A MULTISCALE ANALYSIS OF MAJOR TRANSITION SEASON NORTHEAST SNOWSTORMS

by

Rebecca B. Steeves

A Thesis

Submitted to the University at Albany, State University of New York

in Partial Fulfillment of

the Requirements for the Degree of

Master of Science

College of Arts & Sciences

Department of Atmospheric and Environmental Sciences

2017

ABSTRACT

Major transition season Northeast snowstorms have the potential to cause widespread socioeconomic disruption in the form of transportation delays, infrastructure damage, and widespread power outages. Because heavy, wet snow tends to occur in transition season Northeast snowstorms, lesser accumulations can result in greater disruption than if the same accumulation occurred in winter season Northeast snowstorms. This study is motivated by the opportunity to improve scientific understanding and forecaster situational awareness of this class of snowstorms by means of a multiscale analysis. The multiscale analysis focuses on documenting: 1) the planetary-to-synoptic-scale flow patterns occurring prior to and during major transition season Northeast snowstorms, with emphasis on the role of moisture transport occurring within atmospheric rivers in the formation and evolution of this class of snowstorms, and 2) the synoptic-to-mesoscale flow patterns in the extratropics occurring prior to and during major transition season Northeast snowstorms, with emphasis on the formation and maintenance of regions of lower-tropospheric cold air that coincide with areas of heavy snowfall.

An objectively developed list of major transition season Northeast snowstorms that occurred during fall and spring from 1983 through 2013 was constructed using National Centers for Environmental Information monthly Storm Data publications. This list was used to create a climatology of this class of snowstorms, which were categorized based on both temporal characteristics and spatial patterns of lower-tropospheric cold air that coincided with areas of heavy snowfall. This study found that major transition season Northeast snowstorms featured a variety of lower-tropospheric cold air patterns that provided a means to categorize similar snowstorms. The lower-tropospheric cold air patterns included a Baroclinic Zone: Southwesterly Thermal wind subset, a Baroclinic Zone: Westerly Thermal wind subset, and a Cold Pool

category. Composite analyses were conducted for these lower-tropospheric cold air patterns using the National Centers for Environmental Prediction Climate Forecast System Reanalysis 0.5° horizontal resolution dataset. The composite analyses were utilized to document the planetary-to-synoptic-scale and synoptic-to-mesoscale flow patterns occurring prior to and during major transition season Northeast snowstorms.

The climatology of major transition season Northeast snowstorms reveals that spring snowstorms are the dominant type of major transition season Northeast snowstorms, with the majority occurring in March. The climatology also reveals: 1) cases with heavy snowfall occur more often at higher latitudes than at lower latitudes in the Northeast when cases are grouped by month, and 2) each of the three lower-tropospheric cold air pattern exhibits a distinct spatial distribution of cases with heavy snowfall. Both temporal and spatial categorizations of snowstorms were used in addressing the hypothesis that atmospheric rivers play a key role in the formation and evolution of major transition season Northeast snowstorms. The climatology reveals that atmospheric rivers are generally common during snowstorms when cases are grouped by month and during snowstorms when cases are grouped by lower-tropospheric cold air pattern. The climatology also reveals that atmospheric rivers influence points of heavy snowfall during most of the snowstorms in the Baroclinic Zone: Southwesterly Thermal Wind subset and the Cold Pool category.

The composite analyses of major transition season Northeast snowstorms reveal various atmospheric flow patterns associated with each of the three lower-tropospheric cold air patterns. At upper levels, each of the three lower-tropospheric cold air patterns tends to exhibit different 500-hPa upstream trough amplitudes and different 250-hPa jet streak orientations. At lower levels, the three lower-tropospheric cold air patterns exhibit varying surface cyclone tracks;

surface anticyclone positions and evolutions; and configurations of frontogenesis regions. The direction of vertically integrated vapor transport in the vicinity of the surface cyclones differs among the three lower-tropospheric cold air patterns, which highlights the potential role of atmospheric rivers in the surface cyclones. The results from the composite analyses are summarized in the form of conceptual models that illustrate the planetary-to-synoptic-scale and synoptic-to-mesoscale atmospheric flow patterns for each of the three lower-tropospheric cold air patterns.

ACKNOWLEDGEMENTS

I would like to thank Dr. Andrea Lang and Dr. Daniel Keyser for advising me while I worked on completing my master's degree. Under their advisement, I have grown so much as a scientist by learning from them, cultivating skills, and refining skills. I am confident that the knowledge I have gained from working with them will help me in my future endeavors. I would also like to thank Neil Stuart and Thomas Wasula, my National Weather Service focal points, for their contribution to this research. I truly appreciate having their input, which has aided in making this research applicable in operations. Being able to conduct research with a goal of transitioning results into operations was a rewarding experience. That being said, I am grateful to the Collaborative Science, Technology, and Applied Research Program, which provided the opportunity to conduct this research with funding from the National Oceanic and Atmospheric Administration grant NA13NWS4680004.

I am deeply indebted to the professors and staff of the Department of Atmospheric and Environmental Sciences at the University at Albany. I am grateful for receiving a prestigious education at the University at Albany from my professors, who were enthusiastic in their teachings, and I am grateful for always being able to count on staff when technological or non-technological issues would arise. I would like to thank my professors that taught me when I attended North Carolina State University for my bachelor's degree in meteorology and also my advisors when I participated in Research Experience for Undergraduates at the National Weather Center and also at the Massachusetts Institute of Technology Haystack Observatory. In addition to learning a great deal from both my professors and my advisors, learning and working with them has helped to shape my career goals and interests.

I would like to thank my fellow University at Albany graduate students, who created an extremely welcoming atmosphere from the time I first visited the university to my last day there. I appreciate the invaluable help of Hannah Attard, Alicia Bentley, Kevin Biernat, Alan Brammer, Kyle Meier, and Benjamin Moore, who shared some of their computer code with me at the University at Albany. Also I would like to thank my officemates in ES 234 for creating a team-like environment full of encouragement and enthusiasm. Last but not least, I am so thankful for the endless support of my family, boyfriend, and friends while I have chased my dream to become a meteorologist.

R. B. S.

New York
October 2017

TABLE OF CONTENTS

LIST OF TABLES

LIST OF FIGURES

and at least one of those points is associated with an AR (blue; hereafter AR-influenced cases) for (b) the Baroclinic Zone: Southwesterly Thermal Wind Subset (BZ: SW), (c) the Baroclinic Zone: Westerly Thermal Wind Subset (BZ: W), and (d) the Cold Pool Category (CP). The embedded table (bottom right) displays the association fraction (%) for each CWA for each lower-tropospheric cold air pattern, calculated by dividing the number of AR-influenced cases by total cases with heavy snowfall in a CWA. The CWA abbreviations in the table are as in Fig. 2.2.

Fig. 4.1 Composites of (left panel) 500-hPa geopotential height (contoured in black every 6 dam), 500-hPa cyclonic relative vorticity (shaded according to the left color bar, 10^{-5} s^{-1}), 500-hPa wind (barbs, m s^{-1}), and 600–400-hPa layer-mean upward vertical velocity (contoured in blue every 2×10^{-3} hPa s^{-1}), and (right panel) 600–400-hPa layer-mean **Q**-vector forcing for vertical motion (i.e., the right-hand side of the **Q**-vector form of the QG-omega equation) (shaded according to the right color bar, 10^{-18} Pa^{-1} s^{-3}), geopotential height (contoured in black every 6 dam), potential temperature (contoured in red every 5ºC), **Q** (vectors, $\geq 0.5 \times 10^{-10}$ K m^{-1} s^{-1}) for the Baroclinic Zone: Southwesterly Thermal Wind subset at (a),(b) t_0 – 48 h, (c),(d) t_0 – 24 h, (e),(f) t_0, and (g),(h) t_0 + 24 h. The white diamond with a black outline in each plot denotes the composite center. The dashed and solid lines denote the locations of several troughs and ridges of interest, respectively, as do the labels "T1," "T2," and "R1."

Fig. 4.2 Composites of (left panel) 250-hPa wind speed (shaded according to the left color bar, m s^{-1}), 1000–500-hPa thickness [red (blue) dashed contours for values > (≤) 540 dam, contoured every 6 dam], and MSLP (contoured in black every 4 hPa), and (right panel) 850-hPa geopotential height (contoured in black every 3 dam), temperature [red (blue) dashed contours for values > (≤) 0ºC, contoured every 5ºC], normalized temperature anomalies (shaded according to the right color bar, σ), and wind (vectors, ≥ 5 m s^{-1}) for the Baroclinic Zone: Southwesterly Thermal Wind subset at (a),(b) t_0 – 48 h, (c),(d) t_0 – 24 h, (e),(f) t_0, and (g),(h) t_0 + 24 h. The white diamond with a black outline denotes the composite center. The yellow labels denote the locations of surface high and low pressure systems of interest.

Fig. 4.3 Composites of (left panel) PWAT (shaded according to the left color bar, mm), normalized PWAT anomalies [positive (negative) contoured in red (blue), contoured every 0.5 σ], 850-hPa wind (vectors, ≥ 8 m s^{-1}), and MSLP (contoured in gray every 4 hPa), and (right panel) IVT magnitude (shaded according to the right color bar, kg m^{-1} s^{-1}) with IVT vectors (≥ 25 kg m^{-1} s^{-1}) overlaid, AR axis (red line with black outline), and MSLP (contoured every 4 hPa) for the Baroclinic Zone: Southwesterly Thermal Wind subset at (a),(b) t_0 – 48 h, (c),(d) t_0 – 24 h, (e),(f) t_0, and (g),(h) t_0 + 24 h. The white diamond with a black outline denotes the composite center.

Fig. 4.4 Composites of (left panel) 1000–850-hPa thickness (shaded according to the left color bar, dam) and MSLP (contoured every 4 hPa), and (right panel) 1000–850-hPa layer mean temperature advection [shaded according to the right color bar, K $(3\ h)^{-1}$], cooling due to ascent [contoured in blue every −0.5 K $(3\ h)^{-1}$], temperature (contoured in red every 2ºC), and streamlines (contoured in gray) for the Baroclinic Zone: Southwesterly Thermal Wind subset at (a),(b) t_0. The white diamond with a black outline in each plot denotes the composite center.

Fig. 4.5 Composites of (left panel) 925–850-layer mean frontogenesis [shaded according to the left color bar, K $(100\ \mathrm{km})^{-1}$ $(3\ \mathrm{h})^{-1}$], 925–850-layer mean potential temperature (contoured in dashed red every 2 K), and MSLP (contoured in black every 4 hPa), and (right panel) a cross section, corresponding to the blue line in the left panel, of frontogenesis [shaded according to the right color bar, K $(100\ \mathrm{km})^{-1}$ $(3\ \mathrm{h})^{-1}$], potential temperature (contoured in black every 2 K), vertical velocity (contoured in red every 2 $\mu\mathrm{b\ s}^{-1} \leq -2\ \mu\mathrm{b\ s}^{-1}$), and ageostrophic circulation in the plane of the cross section (vectors) for the Baroclinic Zone: Southwesterly Thermal Wind subset at (a),(b) t_0. The middle tick-mark on the x-axis of the cross section indicates the center of the cross section.

Fig. 4.6 Composites of cross sections along the blue line in Fig. 4.5a of (left panel) relative humidity (shaded according to the left color bar, %), vertical velocity (contoured in black every 2 $\mu\mathrm{b\ s}^{-1}$), and the upper (−18ºC) and lower (−12ºC) bounds of the DGZ (contoured in white), and (right panel) temperature (shaded according to the right color bar, ºC), freezing level (thin black line, 0ºC), and equivalent potential temperature (contoured every 3 K) for the Baroclinic Zone: Southwesterly Thermal Wind subset at (a),(b) t_0.

Fig. 4.7 As in Fig. 4.1 except for the Baroclinic Zone: Westerly Thermal Wind subset. The dashed and solid lines denote the locations of several troughs and ridges of interest, respectively, as do the labels “T3,” “T4,” and “R2.”

Fig. 4.8 As in Fig. 4.2 except for the Baroclinic Zone: Westerly Thermal Wind subset.

Fig. 4.9 As in Fig. 4.3 except for the Baroclinic Zone: Westerly Thermal Wind subset.

Fig. 4.10 As in Fig. 4.4 except for the Baroclinic Zone: Westerly Thermal Wind subset.

Fig. 4.11 As in Fig. 4.5 except for the Baroclinic Zone: Westerly Thermal Wind subset. The cross section shown in the right panel corresponds to the blue line in the left panel.

Fig. 4.12 As in Fig. 4.6 except for the Baroclinic Zone: Westerly Thermal Wind subset. The cross sections correspond to the blue line in Fig. 4.11a.

Fig. 4.13 As in Fig. 4.1 except for the Cold Pool category. The dashed and solid lines denote the locations of several troughs and ridges of interest, respectively, as do the labels “T5,” “T6,” and “R3.”

Fig. 4.14 As in Fig. 4.2 except for the Cold Pool category. The yellow labels “J1” and “J2” correspond to jet streaks of interest, and the remaining yellow labels denote the locations of surface high and low pressure systems of interest. The composite center (i.e., the white diamond with a black outline as denoted in Fig. 4.2) is not shown in the right panel but corresponds to the location of the composite center in the left panel.

Fig. 4.15 As in Fig. 4.3 except for the Cold Pool category.

1. Introduction

1.1 Motivation

Snowstorms have the potential to cause widespread socioeconomic disruption in a variety of forms, such as personal injury, infrastructure damage, and transportation delays. For example, the 12–14 March 1993 Northeast snowstorm caused numerous deaths, an estimated $2 billion in property damage at that time, and the "most widespread disruption of air travel in the history of aviation" (Kocin et al. 1995). The disruptive nature of snowstorms, such as the 12–14 March 1993 example, can be tied to the various weather hazards beyond snowfall accumulation, such as "freezing precipitation, flooding rains, high winds, bitterly cold temperatures, coastal flooding (and erosion), and even strong convection" (Maglaras et al. 1995). The disruptive nature of snowstorms is enhanced when snowstorms occur in highly populated regions such as the northeastern United States (U.S.) (Maglaras et al. 1995), a factor that Kocin and Uccellini (2004a) and Squires et al. (2014) took into account when constructing snowstorm impact scales. With a large portion of the U.S. population residing in the Northeast and at risk to Northeast snowstorms, many studies have been conducted to specifically understand the development and evolution of this class of snowstorms. Northeast snowstorms can be described by three essential ingredients: 1) ascent, which can arise from processes accompanying cyclones, 2) moisture, which can arise from nearby bodies of water, such as the North Atlantic Ocean and the Gulf of Mexico, and 3) lower-tropospheric cold air, which can arise from processes accompanying anticyclones (Kocin and Uccellini 2004b, pp. 4–6). The last ingredient, lower-tropospheric cold air, is more prevalent in winter than in fall and spring (hereafter fall and spring are together referred to as transition seasons). Because of the limited availability of lower-tropospheric cold air during the transition seasons, assessing when the essential ingredients coincide may improve forecaster situational awareness for transition season Northeast snowstorms.

The socioeconomic disruption from transition season Northeast snowstorms can match, or even exceed, that of a winter season Northeast snowstorm because heavy, wet snow tends to occur during the transition seasons. Therefore, lesser accumulations in transition season Northeast snowstorms can result in greater disruption than if the same accumulation occurred in winter season Northeast snowstorms. Furthermore, trees in full leaf during the transition seasons enhance the disruption due to tree limbs breaking from the weight of the heavy, wet snow. For example, heavy, wet snow in the Northeast was reported in the National Centers for Environmental Information (NCEI; formerly National Climatic Data Center) monthly *Storm Data* (*SD*) publications for the 31 March–1 April 1997 and 28–30 October 2011 snowstorms. For the 31 March–1 April 1997 snowstorm, the monthly *SD* publication related that heavy, wet snow and strong winds were responsible for power outages to nearly 750,000 customers in Massachusetts, and the weight of the snow caused roof collapses in eastern Massachusetts (NCEI 1997a, NCEI 1997b). Disruption to the road system from this spring snowstorm was so extensive that humvees from the National Guard were deployed in Pennsylvania to rescue stranded drivers (NCEI 1997b). For the 28–30 October 2011 snowstorm, almost one million customers experienced power outages in eastern Pennsylvania as a result of the heavy, wet snow and trees with full leaf (NCEI 2011). Additionally, this fall snowstorm was indirectly responsible for six deaths in Massachusetts (NCEI 2011). The socioeconomic disruption from these two major transition season Northeast snowstorms was so extensive that states of emergency were declared for both of these snowstorms (NCEI 1997b; NCEI 2011).

Due to the significant socioeconomic disruption caused by major transition season Northeast snowstorms, the goal of this study is to improve scientific understanding and forecaster situational awareness of this class of snowstorms by means of a multiscale analysis through the use of composite analyses. The multiscale analysis emphasizes the role of moisture transport occurring within atmospheric rivers (ARs) in the formation and evolution of this class of snowstorms. Atmospheric rivers during the transition seasons in the Northeast have been documented by Lavers and Villarini (2015), but the role of ARs in regions of heavy snowfall in transition season Northeast snowstorms is still undocumented. The multiscale analysis also emphasizes the formation and maintenance of regions of lower-tropospheric cold air that coincide with areas of heavy snowfall, because the processes that generate lower-tropospheric cold air can represent forecast challenges. Lower-tropospheric cold air can form in the region of heavy snowfall as a result of processes ranging from the synoptic scale to the microscale. For example, Kocin et al. (1995) stated that cold air was advected into the region of heavy snowfall for the 12–14 March 1993 snowstorm, whereas Bosart and Sanders (1991) suggested that cold air was likely generated in-situ by melting snow during the 4 October 1987 snowstorm.

By focusing on the coincidence of essential ingredients and conducting a multiscale analysis of major transition season Northeast snowstorms through the use of composite analyses, this study addresses two scientific opportunities. First, western U.S. ARs have been well documented in the meteorological literature, but to the author's knowledge only two papers (Halverson and Rabenhorst 2010; Lavers and Villarini 2015) discussed ARs in the northeast U.S. In the first paper, Halverson and Rabenhorst (2010) suggested that an AR occurred in an eastern U.S. snowstorm during 5–6 February 2010, and in the second paper, Lavers and Villarini (2015) conducted an analysis with a focus on the AR contribution to continental U.S. precipitation during 1979–2012. Neither paper uses objectively identified ARs to investigate their role in regions of heavy snowfall during Northeast snowstorms. Second, case studies of transition season Northeast snowstorms have been conducted, but to the author's knowledge, no study has conducted composite analyses focusing solely on transition season Northeast snowstorms. Composite analyses have been conducted for snowstorms occurring during January 1946–February 1966 for the Northeast and mid-Atlantic coastal regions (Brandes and Spar 1971), and Thomas and Martin (2007) included snowstorms that tracked through the Northeast when they performed a composite analysis of Alberta clippers occurring during the cool season. Other recent studies conducted composite analyses of snowstorms occurring during the cool season for regions other than the Northeast, such as the Southeast and southern Great Plains (e.g., Mote et al. 1997; Mullens et al. 2016). With a unique focus on the transition seasons, this study aims to improve existing conceptual models and forecaster situational awareness for major transition season Northeast snowstorms through the use of composite analyses.

1.2 Literature Review

This literature review is composed of two sections, the first on Northeast snowstorms (section 1.2.1) and the second on ARs (section 1.2.2). Section 1.2.1 will begin with a discussion on climatological characteristics of snowstorms with a focus on snowstorms in the northeast U.S. Following the climatological discussion, synoptic conditions will be discussed in terms of three principal foci prior to and during Northeast snowstorms: 1) upper-level synoptic conditions, 2) lower-level synoptic conditions, and 3) synoptic conditions from a Lagrangian perspective. Following the synoptic discussion, mesoscale conditions observed during Northeast snowstorms will be considered. The discussion will then proceed to review thermodynamic and microphysical processes, first with a focus on the production and maintenance of lower-tropospheric cold air and second with a focus on snow density. Section 1.2.2 will begin with a general discussion of ARs by presenting the original definition of an AR and discussing the role of ARs in moisture transport from a planetary-to-synoptic-scale perspective. An elaboration on the various definitions and methods used to identify ARs will follow the general discussion. The AR section will conclude with a review of the connection of ARs to flooding and rainfall.

1.2.1 Northeast Snowstorms

Changnon et al. (2006) concluded that a latitudinal gradient of the annual average number of snowstorms existed east of the Rocky Mountains; east of the Rocky Mountains the annual average number of snowstorms generally increased as latitude increased. They defined a snowstorm as the occurrence of at least 15.2 cm (6 in.) of snowfall at a weather station during one or two days. Like Changnon et al. (2006), Kocin and Uccellini (2004b, pp. 10–39) generally observed a latitudinal gradient, but for mean seasonal snowfall for the northeast U.S. Similarly, the snowfall season length was noted to have a latitudinal dependence (Harrington et al. 1987; Changnon et al. 2006) as shown in Fig. 1.1. From Fig. 1.1 it is evident that higher latitudes of the eastern U.S. generally experience the first snowstorm of the season earlier in the fall and the last snowstorm of the season later in the spring than lower latitudes of the eastern U.S. (Changnon et al. 2006). The prevalence of snowstorms and the long-lasting snowfall season of the Northeast can be largely attributed to its proximity to the Gulf Stream, North Atlantic Ocean, Gulf of Mexico, Great Lakes, and Appalachian Mountains (Maglaras et al. 1995). In particular, Reitan

(1974) and Colucci (1976) highlighted the high frequency of cyclones occurring during winter over the western North Atlantic Ocean, and Reitan (1974) attributed the high frequency of cyclones to the cold, continental air flowing over the warm waters of the western North Atlantic Ocean, providing conditions conducive to cyclone development. Furthermore, Sanders and Gyakum (1980) and Roebber (1984) concluded that explosive cyclones frequently occurred in the Gulf Stream region, which is characterized by persistent low-level baroclinicity. Lastly, both the North Atlantic Ocean and the Appalachian Mountains can increase baroclinicity through cold-air damming and coastal frontogenesis, which can aid in providing an environment favorable for cyclogenesis (e.g., Bosart et al. 1972; Richwein 1980; Maglaras et al. 1995; Kocin and Uccellini 2004b, pp. 214–217).

Kocin and Uccellini (2004b, pp. 41–46, p. 79) conducted an extensive study of Northeast snowstorms, where they documented the synoptic conditions prior to and during 30 snowstorms that affected northeastern metropolitan areas. The 30 snowstorms occurred in December through April, and the majority of the snowstorms (24 of 30) occurred during winter (December–February). Their study also documented common synoptic conditions prior to the 30 Northeast snowstorms (Kocin and Uccellini 2004b, pp. 79–101), which are summarized in Fig. 1.2. The first common synoptic condition was an upper-level ridge over the west coast of the U.S. or Canada. Kocin and Uccellini (2004b, pp. 79–101) noted that Lackmann et al. (1996) highlighted the importance of the upper-level ridge as a precursor to explosive cyclogenesis over the western North Atlantic Ocean. The second common synoptic condition was a deep upper-level trough over eastern Canada with a polar jet streak frequently embedded in the flow at the base of the upper-level trough. Often over southeastern Canada and the northeastern U.S., a confluent entrance region of the polar jet streak was observed upstream of the upper-level trough axis

(Kocin and Uccellini 2004b, pp. 101–124; their Figs. 4-12 and 7-7). The upper-level confluence has been linked to the ingredient of lower-tropospheric cold air over the East Coast in several studies (e.g., Bell and Bosart 1989; Kocin and Uccellini 2004b, pp. 101–124). The third common synoptic condition was a subtropical jet streak located over the southeastern U.S. (Kocin and Uccellini 2004b, pp. 79–101). The diffluent exit region of the subtropical jet streak was often the site of snowstorm development.

In addition to documenting common synoptic conditions prior to the 30 Northeast snowstorms, Kocin and Uccellini (2004b, pp. 101–124) also documented common synoptic conditions during the 30 Northeast snowstorms. The first synoptic condition, the upper-level trough, became more common among the cases as the time of heavy snow approached (Kocin and Uccellini 2004b, pp. 79–101). To illustrate, at 36-h prior to the snowstorm, Kocin and Uccellini (2004b, pp. 79–101) noted that half of the cases had well-established upper-level troughs and the other half of the cases had developing upper-level troughs. As the time of heavy snow approached, the majority of the cases (28 of 30) exhibited an amplification of the upper-level trough (Kocin and Uccellini 2004b, pp. 101–124). Additionally, the majority of the cases (28 of 30) exhibited a decrease of the half-wavelength between the upper-level trough associated with the snowstorm and the upper-level ridge downstream while the upper-level trough was observed to amplify. Both the amplification of the upper-level trough and the decrease of the half-wavelength were manifested as enhanced cyclonic vorticity advection and upper-level divergence and were consistent with concepts from Sutcliffe's "self-development" (Sutcliffe and Forsdyke 1950; Kocin and Uccellini 2004b, pp. 101–124, pp. 231–232). The second synoptic condition involved the dynamic coupling of the subtropical and polar jet streaks. Kocin and Uccellini (2004b, pp. 101–124) noted that Uccellini and Kocin (1987) identified this condition in a study of eight snowstorms and found the condition to be conducive to heavy snowfall. Kocin and Uccellini (2004b, pp. 101–124) described how the alignment of the subtropical and polar jet streaks allowed for lateral coupling of the ascent regions of the two jet streak vertical circulations. Figure 1.3 illustrates how the exit region of the subtropical jet streak and the entrance region of the polar jet streak align so that the upward components of both transverse circulations can act in concert to enhance ascent in the region of the snowstorm.

Along with assessing the lower-level synoptic conditions of Northeast snowstorms, Kocin and Uccellini (2004b, pp. 101–124) made connections between the upper-level and the lower-level synoptic conditions. For instance, they noted that the transverse circulations of the subtropical and polar jet streaks influenced the lower-level environment of the snowstorms by aiding in the advection of warm, moist air and cold, dry (i.e., Canadian) air, respectively. The transverse circulation of the subtropical jet streak was unique in that a wind maximum, or lower-level jet (LLJ) streak, was observed within the lower-level branch of the indirect transverse circulation of the subtropical jet streak in all 30 Northeast snowstorms. The LLJ was typically observed east or northeast of the cyclone center aiming toward the heaviest snowfall region. The importance of the LLJ in Northeast snowstorms was highlighted for its ability to transport moisture to the heaviest snowfall region on a scale similar to Midwest spring convective cases (Uccellini et al. 1987; Kocin and Uccellini 2004b, pp. 214–217). Kocin and Uccellini (2004b, pp. 101–124) also noted a connection between surface anticyclones, which provides lower-tropospheric cold air for Northeast snowstorms, and upper-level confluent regions, and stated that Bell and Bosart (1989) noted a similar connection between surface anticyclones and the confluent entrance region of a polar jet streak. Kocin and Uccellini (2004b, pp. 217–219) specifically noted that most cases of Northeast snowstorms (25 of 30) featured surface anticyclones under an upper-level confluent region upstream of an upper-level trough over eastern Canada, which often coincided with the entrance region of a polar jet streak. The surface anticyclones for the 30 snowstorms were observed to have two general types of evolution (Fig. 1.4): 1) a primary anticyclone that moved east from central Canada to southeastern Canada and the northeastern U.S., and 2) a primary anticyclone over central Canada that generally moved southward into the central U.S. while retaining an elongated eastward-directed high-pressure ridge or secondary high-pressure center over southeastern Canada or the northeastern U.S. (Kocin and Uccellini 2004b, pp. 59–77).

In addition to considering Northeast snowstorms from an Eulerian perspective, Northeast snowstorms can be considered from a Lagrangian perspective in terms of airstreams (e.g., Kocin and Uccellini 2004b, pp. 124–131). Carlson (1980) developed a schematic representation of airstreams involved in an extratropical cyclone through a cyclone-relative isentropic analysis based on the assumption of a steady-state system (i.e., the cyclone is not changing speed, shape, or intensity). His schematic representation consisted of the cold conveyor belt, the warm conveyor belt, and the dry airstream. Figure 1.5 displays a modified version of the schematic representation that was produced by Kocin and Uccellini (2004b, pp. 124–131) for a Northeast snowstorm. In their schematic, cyclone-relative trajectories of cold air, termed the cold conveyor belt, form an airstream around the periphery of the anticyclone and move from their northern origin toward the North Atlantic Ocean. Once the airstream reaches the ocean, it turns toward the west, remaining north of the cyclone and low in altitude. Eventually the airstream splits into two branches that curve either cyclonically or anticyclonically. Cyclone-relative trajectories of warm, moist air, termed the warm conveyor belt, ascend over the cold conveyor belt as the trajectories travel northward from their origin in the lower-levels of the warm sector. The warm conveyor belt eventually curves anticyclonically as it ascends and then continues on an eastward path at upper levels. Lastly, cyclone-relative trajectories of dry air, termed the dry airstream, descend from the tropopause region and then split into two airstreams. One airstream continues to descend in the wake of the cold front. The second airstream later ascends and continues on a generally eastward path poleward of the warm conveyor belt. Several studies have further examined the airstream structure of extratropical cyclones (Kocin and Uccellini 2004b, pp. 124–131). For instance, Martin (1999) concluded from three case studies that an airstream beginning in the lower-levels of the warm sector of the cyclone eventually curved cyclonically as it ascended in the occluded sector of the cyclone. Martin (1999) termed this airstream the trowal airstream and stated that precipitation in the northwest sector of an occluded cyclone was frequently produced in the trowal airstream. Findings from Schultz (2001) supported the results from Martin (1999). Schultz (2001) reexamined the 5 December 1977 case study of Carlson (1980) and concluded that the warm conveyor belt split with one branch curving cyclonically. The branch of the warm conveyor belt that curved cyclonically produced precipitation in the northwest sector of the cyclone. In contrast to Schultz (2001), Carlson (1980) suggested that the branch of the cold conveyor belt that curved anticyclonically produced that precipitation.

The northwest sector of the cyclone has been noted as a location of heavy snowfall and a region conducive to mesoscale precipitation bands (e.g., Nicosia and Grumm 1999; Novak et al. 2004). Nicosia and Grumm (1999) stated that heavy snowfall occurred in the northwest sector of the cyclone for all three of their cases, with one case occurring during the fall season. In all three of their cases, they observed mesoscale snowbands with high snowfall rates toward the north of the cyclone. Novak et al. (2004) created a climatology of single-banded precipitation events, being either liquid or frozen precipitation, for five cold seasons (October–April) and noted that most of their events occurred in the northwest sector of the cyclone. Novak et al. (2004) also performed composite analyses and case studies of single-banded precipitation events. Their results and other studies (e.g., Nicosia and Grumm 1999) had consistent findings pertaining to the development of the mesoscale precipitation bands, which suggested that mesoscale precipitation bands developed in environments characterized by frontogenesis and weak moist symmetric stability. In contrast to previous studies, Evans (2006) focused on a snowband associated with a weaker system than many of those previously studied. Evans (2006) analyzed the transition season Northeast snowstorm that occurred on 30 March 2003 and found results consistent with those of Nicosia and Grumm (1999) pertaining to the development of the snowband. The northwest sector of the cyclone has also been noted as a location of heavy snowfall due to surface fronts (Kocin and Uccellini 2004b, pp. 186–193). Kocin and Uccellini (2004b, pp. 186–193) stated, "the [surface] fronts represent sites of localized baroclinic zones that can act to focus strong ascent in relatively narrow bands." They illustrated the results of the focused ascent with two historic transition season Northeast snowstorms, specifically the 11–14 March 1888 and the 22–28 November 1950 snowstorms. Both of the snowstorms had a surface front that stretched northward from the cyclone center and localized regions of snowfall accumulation values exceeding 45 in. to the west of the surface front. Furthermore, ascent in baroclinic zones, such as surface fronts, can be diabatically enhanced by melting snow (Szeto and Stewart 1997).

Thermodynamic and microphysical processes, such as melting snow, are important in snowstorms because these processes can influence the vertical thermal profile, which dictates precipitation type (Lackmann et al. 2002). The importance of these processes in diabatically cooling lower-tropospheric air to temperatures conducive for the occurrence of snowfall has been documented by Gedzelman and Lewis (1990), Bosart and Sanders (1991), and Market et al. (2006). Gedzelman and Lewis (1990) identified several snowstorms with diabatically cooled lower-tropospheric cold air, such as the 4 October 1987 snowstorm, and termed this type of snowstorm as a "warm snowstorm." Bosart and Sanders (1991) conducted an in-depth analysis of the 4 October 1987 snowstorm and suggested that the snowstorm generated a cold pool of air with temperatures near freezing. They suggested the cold pool of air likely formed from diabatic cooling due to melting snow. In addition to the case study of 4 October 1987, diabatic cooling due to melting snow has been well documented in the meteorological literature (e.g., Kain et al. 2000; Lackmann et al. 2002; Market et al. 2006; Ganetis and Colle 2015). For example, Kain et al. (2000) developed criteria to identify a possible precipitation type changeover from diabatic cooling due to melting snow for use in a forecast setting. In contrast to the well-documented diabatic cooling due to melting snow, Market et al. (2006) stated in the context of their study that the "sublimation of snow or 'wet-bulbing' is a widely accepted (yet little studied) process for cooling and moistening a deep layer over a short period." Their study and Homan and Uccellini (1987) denoted the importance of diabatic cooling due to sublimation and evaporation in allowing precipitation to fall as snow.

The vertical thermal profile not only dictates precipitation type, but also influences snow density. Temperature can influence snow density by affecting ice crystal shape, ice crystal growth rate, and riming (e.g., Roebber et al. 2003; Baxter et al. 2005; Cobb and Waldstreicher 2005; Ware et al. 2006). First, different shapes of ice crystals form and grow in different combinations of temperature and supersaturation levels, and the various shapes of ice crystals are associated with different snow densities (Roebber et al. 2003). Second, ice crystal growth occurs at a faster rate when temperatures are between −12°C and −18°C than when the temperature is outside of this range (Cobb and Waldstreicher 2005). The portion of the vertical thermal profile that is characterized by the preferred temperature range for ice crystal growth is referred to as the dendritic growth zone (DGZ) because this temperature range is also conducive to the formation of the dendritic ice crystal shape (DeVoir 2002). Roebber et al. (2003) noted the importance of the ice crystal growth rate in affecting the size of the ice crystal, which then affects snow density. Third, riming is more likely to occur when the cloud temperature is warmer than −10°C due to the presence of super cooled water (Cobb and Waldstreicher 2005). Riming contributes towards producing high-density snow (Cobb and Waldstreicher 2005; Baxter et al. 2005).

Cobb and Waldstreicher (2005) applied an algorithm utilizing the "Cross-Hair Approach," originally proposed by Waldstreicher (2001), which included several of the aforementioned concepts, specifically ice crystal shape and ice crystal growth rate. The "Cross-Hair Approach" included locating layers where the DGZ was collocated with high relative humidity values and the core of upward vertical motion; these layers often yielded high snowfall rates and low-density snow (Cobb and Waldstreicher 2005). Cobb and Waldstreicher (2005) also described an alternative alignment of these features found to be conducive to high-density snow, consisting of a saturated layer where the DGZ was located above the core of upward vertical motion. High-density snow was also generally found to occur when the lower-level temperature was warm (Ware et al. 2006). Since early winter (October and November) and late winter (March and April) climatologically have warmer lower-level temperatures than midwinter (December, January, and February), the findings of Ware et al. (2006) were consistent with Baxter et al. (2005). Baxter et al. (2005) found that generally higher snowfall densities in the contiguous U.S. occurred in early and late winter than in midwinter.

1.2.2 Atmospheric Rivers

Atmospheric rivers can generally be described as filamentary moisture plumes that extend poleward from lower latitudes (Zhu and Newell 1998). Zhu and Newell (1998) highlighted how the filamentary moisture plumes behaved like a river, stating that the moisture flux of an AR was comparable to the water flux of the Amazon River. They concluded that the moisture fluxes of ARs were responsible for the majority of the meridional moisture transport at midlatitudes. The conclusion of Zhu and Newell (1998) stemmed from work with model output data from the European Centre for Medium-Range Weather Forecasts, and Ralph et al. (2004) later published a study supporting the conclusion of Zhu and Newell (1998) through the use of observational data from airplanes and satellites. Ralph et al. (2004) created a conceptual representation of an AR based on AR characteristics observed during their study (Fig. 1.6). Figure 1.6 illustrates an AR as a generally low-lying feature with a core focused around 1 km above mean sea level, and also illustrates the close proximity of an AR to a polar cold front. Other studies also have noted that ARs occurred ahead of cold fronts in extratropical cyclones (e.g., Neiman et al. 2008a; Gimeno et al. 2014). Results from Dacre et al. (2015) explained the close proximity of an AR to a cold front. They concluded that the advance of the cold front toward the warm front resulted in convergence of water vapor and consequently a band of locally higher total column water vapor content corresponding to an AR.

The origin of moisture in ARs has been examined in numerous studies in order to determine whether moisture in the AR originated from local convergence of moisture (e.g., Dacre et al. 2015), from the transport of subtropical or tropical moisture (e.g., Moore et al. 2012), or from a combination of the two (e.g., Bao et al. 2006; Sodemann and Stohl 2013;

Ramos et al. 2016). For example, Dacre et al. (2015) stated that the convergence of water vapor along the cold front implied that moisture was supplied locally to the AR. Their conclusion was in close agreement with the findings from Bao et al. (2006) and Sodemann and Stohl (2013). Bao et al. (2006) conducted a trajectory analysis of bands of vertically integrated water vapor (IWV) for five cases and found that the bands of IWV formed mostly from local moisture convergence. However, their trajectory analysis suggested the possibility that tropical moisture may be transported within the band of IWV to the extratropics. Sodemann and Stohl (2013) investigated moisture source regions for precipitation that occurred during AR conditions in two domains in Norway for December 2006. They defined AR conditions for a domain as the occurrence of IWV > 14 mm over land in the domain. They found that an oceanic latitudinal band adjacent to Norway (Fig. 1.7), specifically the band defined by either 50°–60°N or 60°–70°N, contributed the most moisture to the precipitation for each domain. However, the subtropical and tropical oceanic source region between 10°N and 30°N was observed to contribute moisture to the precipitation during AR conditions, but this oceanic source region contributed less than 3% in each domain.

There are various AR identification methods documented in the meteorological literature. For example, one AR identification method was developed by Ralph et al. (2004), who proposed the use of IWV for identifying ARs. Their proposal was founded on the correlation they observed between IWV and horizontal water vapor flux and on the availability of accurate satellite IWV measurements. Thus they identified an AR, during 137 continuous days, as a filamentary moisture plume that had IWV > 2 cm with the following dimensions: 1) a length ≥ 2000 km and 2) a width ≤ 1000 km. Neiman et al. (2008a) validated the methodology of Ralph et al. (2004) after investigating ARs from eight years of satellite observations. Other AR identification methods, summarized in Table 1.1, use vertically integrated water vapor transport (IVT). For instance, in order to identify ARs in the western U.S., Rutz et al. (2014) used a minimum IVT threshold of 250 kg m^{-1} s^{-1} and employed a modified version of the methodology proposed by Ralph et al. (2004) and Neiman et al. (2008a). In order to identify ARs in the southeast U.S., Mahoney et al. (2016) used 500 kg m^{-1} s^{-1} as the minimum IVT threshold and applied an objective algorithm developed by Wick (2014). In order to identify ARs over the central and eastern U.S., Lavers and Villarini (2015) set the minimum IVT threshold to 367.8 kg m^{-1} s^{-1}, which was based on a statistical analysis, and implemented a modified version of the objective identification algorithm by Lavers and Villarini (2013).

Regardless of the various ways to identify ARs, there is strong agreement in the meteorological literature on the connection between ARs and significant precipitation. For example, Ralph et al. (2006) found that AR conditions defined in the context of their study led to heavy orographic rainfall every time the Russian River in California reached the flood stage between 1 October 1997 and 28 February 2006. They defined AR conditions according to the criteria set forth by Ralph et al. (2004) along with coastal observations of low-level wind and IWV to determine onshore moisture transport. In another example, Neiman et al. (2008b) connected the presence of a strong AR to heavy rainfall on 6–8 November 2006, which "exceeded 100-yr precipitation thresholds for 24-h periods" for selected locations in the Pacific Northwest. In the south-central U.S., Moore et al. (2012) noted a connection between an AR and destructive flooding in Kentucky and Tennessee in May 2010. In the southeast U.S., Mahoney et al. (2016) concluded that the presence of an AR corresponded on average to 41% of heavy rain days between January 2002 and December 2011. In the northeast U.S., Lavers and Villarini (2015) found that ARs generally contributed to precipitation the most in winter (30–50% AR fraction, defined as the ratio of AR attributed precipitation to total precipitation during 1979–2012) and suggested snowfall events caused the large AR fraction. Although the AR fraction was generally highest in winter months, the AR fraction was comparable to winter months for selected areas in the Northeast during November, March, and April (Lavers and Villarini 2015).

1.3 Research Goals and Thesis Structure

The goal of this study is to improve scientific understanding and forecaster situational awareness of major transition season Northeast snowstorms by conducting a multiscale analysis of this class of snowstorms. The multiscale analysis will focus on documenting: 1) the planetary-to-synoptic-scale flow patterns occurring prior to and during major transition season Northeast snowstorms, with emphasis on the role of moisture transport occurring within ARs in the formation and evolution of this class of snowstorms, and 2) the synoptic-to-mesoscale flow patterns in the extratropics occurring prior to and during major transition season Northeast snowstorms, with emphasis on the formation and maintenance of regions of lower-tropospheric cold air that coincide with areas of heavy snowfall.

Chapter 2 will detail the datasets and the methodology used for the identification, categorization, and analysis of major transition season Northeast snowstorms. Chapters 3 and 4 will focus on the results from the analyses of the snowstorms, which are categorized based on characteristic patterns of lower-tropospheric cold air that coincide with areas of heavy snowfall. The results will begin with the climatology in Chapter 3 and will be followed by composite analyses of the aforementioned categories in Chapter 4. Chapter 5 will discuss the results from the climatology and composite analyses and will highlight the major conclusions. Also in

Chapter 5, the transfer of research to operations will be discussed along with suggestions for future work.

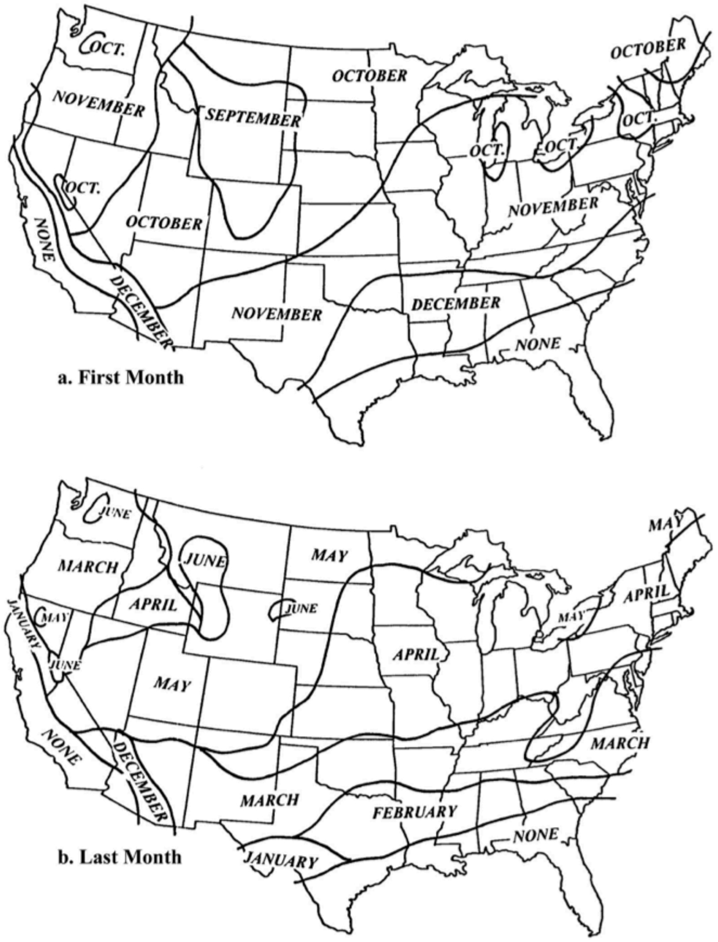

Fig. 1.1. Geographical distribution of the month of (a) the first snowstorms of the season (b) the last snowstorms of the season. Snowstorms for 1901–2001 were considered [Fig. 10 and adapted caption from Changnon et al. (2006)].

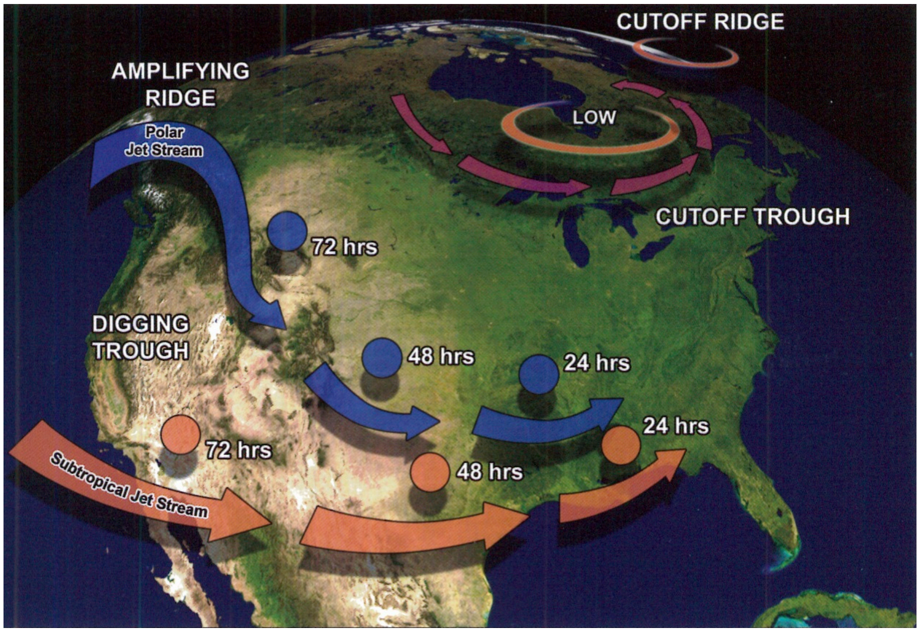

Fig. 1.2. Schematic of upper-level synoptic conditions observed 72-h, 48-h, and 24-h prior to Northeast snowstorms [Fig. 4-4 and caption adapted from Kocin and Uccellini (2004b)].

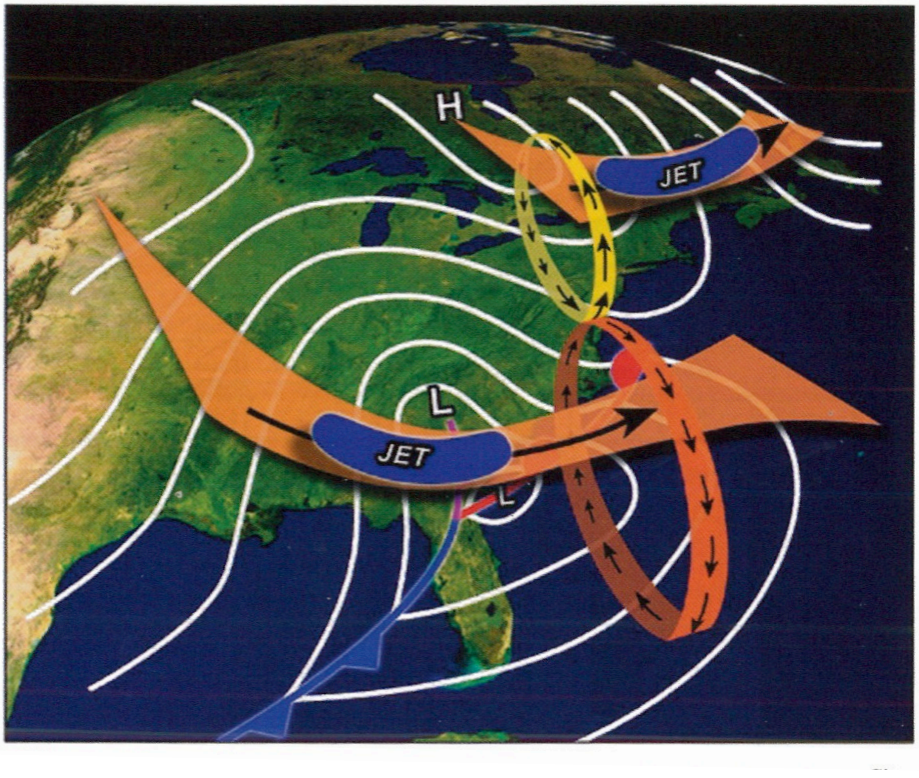

Fig. 1.3. Schematic of the configuration of upper-level jet streaks found by Uccellini and Kocin (1987) to be conducive to heavy snowfall. Yellow and orange circles depict the transverse circulations of the jet streaks, and white lines depict sea level isobars [Fig. 4-17 and caption adapted from Kocin and Uccellini (2004b)].

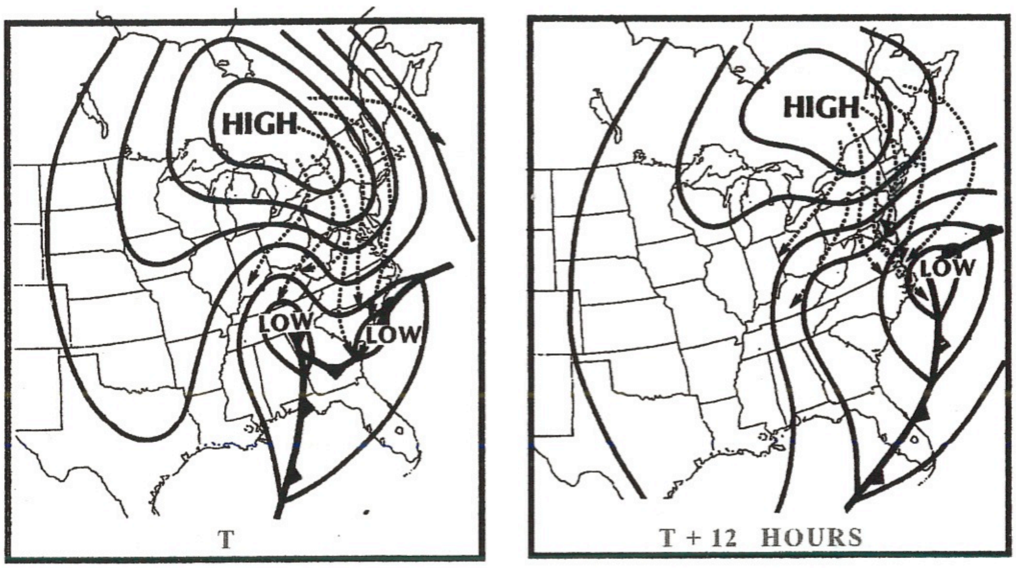

PRIMARY ANTICYCLONE OVER ONTARIO-QUEBEC

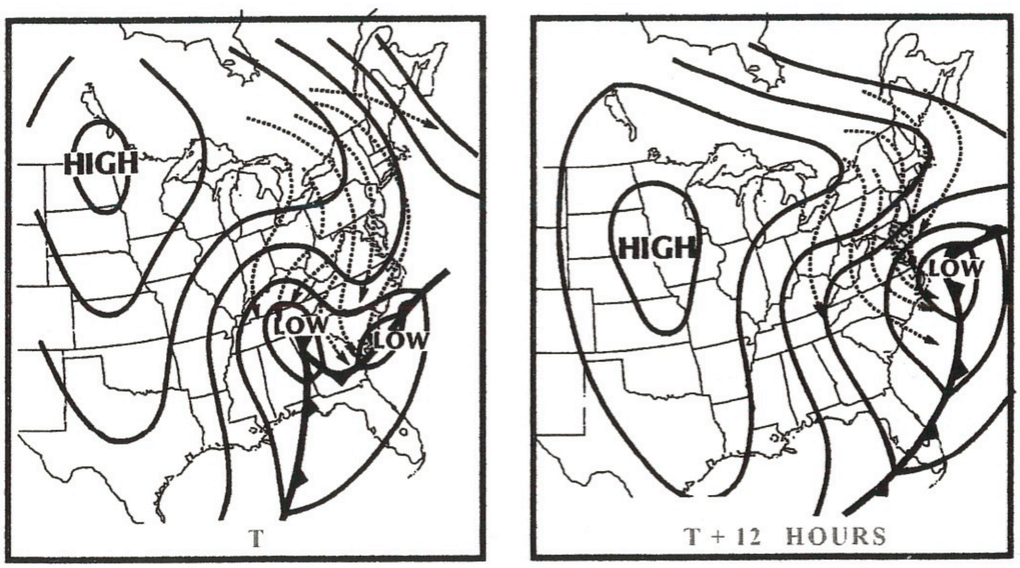

SECONDARY ANTICYLONE OR SURFACE RIDGE AXIS

Fig. 1.4. Depiction of the two general types of evolution of anticyclones observed during Northeast snowstorms. Solid lines denote sea level isobars, and dotted lines denote streamlines [Fig. 3-12 and caption adapted from Kocin and Uccellini (2004b)].

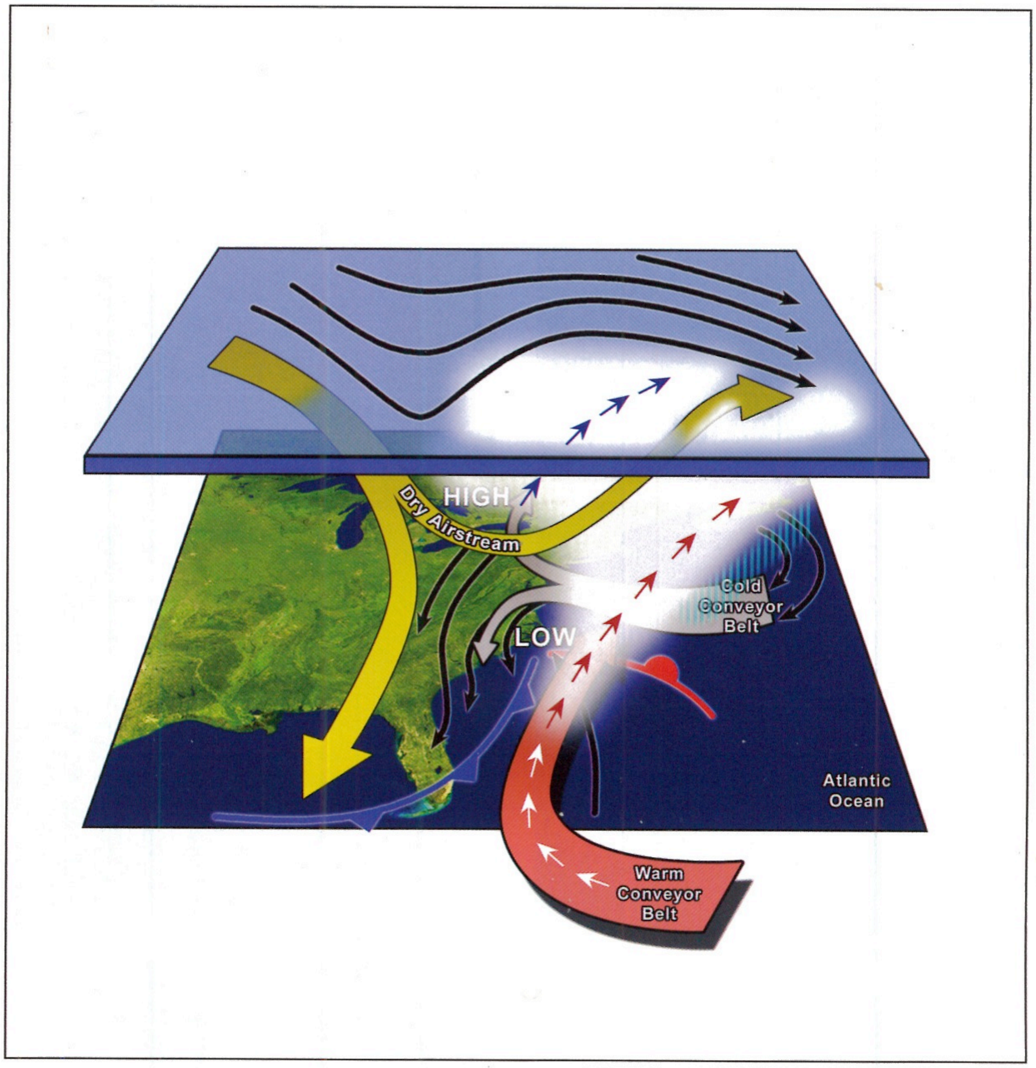

Fig. 1.5. Schematic representation of airstreams for a Northeast snowstorm that was adapted from Carlson (1980). Black lines denote streamlines for lower- and upper-levels [Fig. 4-23 and caption adapted from Kocin and Uccellini (2004b)].

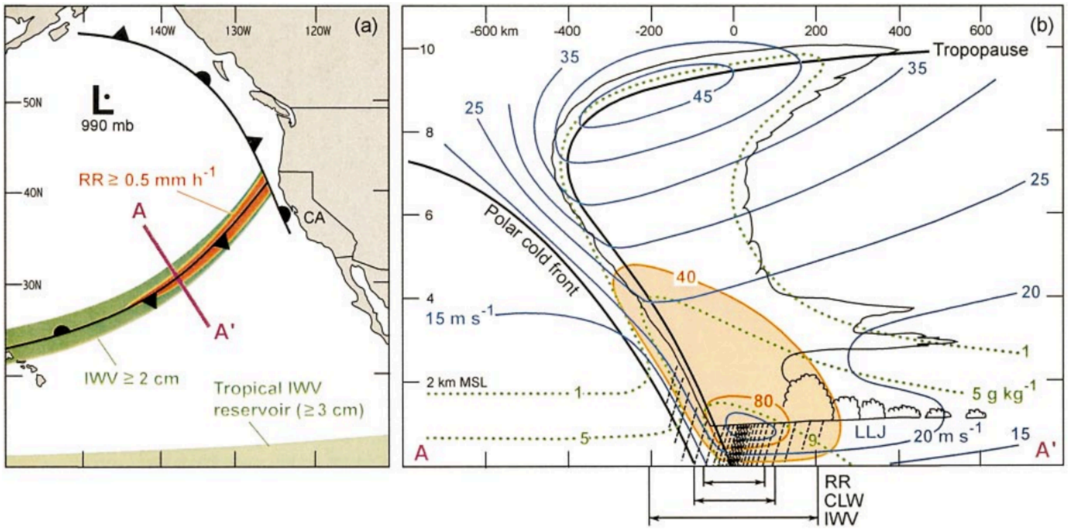

Fig. 1.6. Conceptual representation of an atmospheric river over the northeastern Pacific Ocean. (a) Plan-view schematic of concentrated IWV (IWV ≥ 2 cm; dark green) and associated rain-rate enhancement (RR ≥ 0.5 mm h^{-1}; red) along a polar cold front. The tropical IWV reservoir (>3 cm; light green) is also shown. The bold line AA' is a cross-section projection for (b). (b) Cross-section schematic through an atmospheric river [along AA' in (a)] highlighting the vertical structure of the alongfront isotachs (blue contours; m s^{-1}), water vapor specific humidity (dotted green contours; g kg^{-1}), and horizontal alongfront moisture flux (red contours and shading; $\times 10^5$ kg s^{-1}). Schematic clouds and precipitation are also shown, as are the locations of the mean width scales of the 75% cumulative fraction of perturbation IWV (widest), CLW, and RR (narrowest) across the 1500-km cross-section baseline (bottom).
[Fig. 23 and reproduced caption from Ralph et al. (2004)].

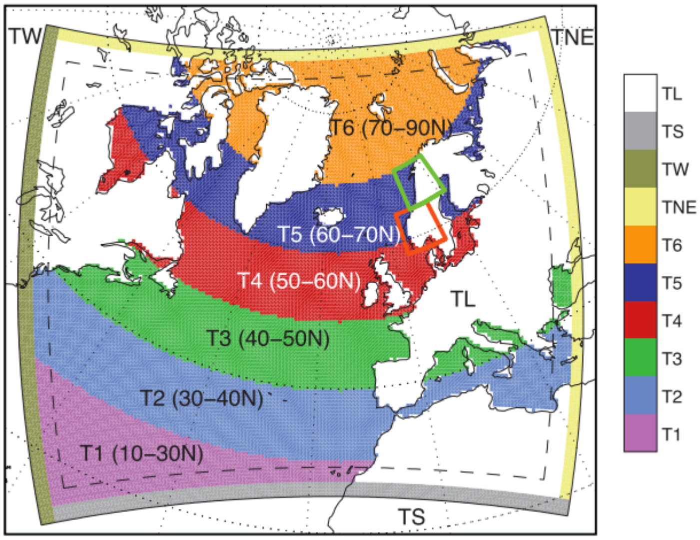

Fig. 1.7. Calculation domain of the CHRM [climate High-Resolution Model] model (solid black line) and interior model domain (dashed black line). Colors show moisture source tracers released by surface evaporation from every 10° latitude band of ocean area (T1–T6), land (TL, here plotted in white), and from advection through the southern (TS), western (TW), and northeastern (TNE) boundaries reaching from the bottom to top of the model domain. Initial atmospheric tracer (TA) is not displayed. Boxed areas over Scandinavia denote the target domains of northern Norway (green) and southern Norway (red) [Fig. 1 and reproduced caption from Sodemann and Stohl (2013)].

Region	**Minimum IVT Threshold**	**Citation**
Western U.S.	250 kg m^{-1} s^{-1}	Rutz et al. (2014)
Southeast U.S.	500 kg m^{-1} s^{-1}	Mahoney et al. (2016)
Eastern U.S.	367.8 kg m^{-1} s^{-1}	Lavers and Villarini (2015)

Table 1.1 Consolidated list of regions and corresponding minimum IVT thresholds from the studies cited in section 1.2.2.

2. Data and Methodology

2.1 Case Identification

The process of major transition season Northeast snowstorm case identification consisted of compiling all non-lake effect events featuring frozen precipitation catalogued in the National Centers for Environmental Information (NCEI; formerly National Climatic Data Center) monthly *Storm Data* (*SD*) publication. Events were compiled during spring (March–May) and fall (September–November) 1979–2013 for the Northeast region as defined by the NCEI. The monthly *SD* publication was utilized as the basis for compiling events and identifying cases because it includes socioeconomic impacts (e.g., power outages, infrastructure damage, and transportation reports) in addition to storm characteristics, such as precipitation amount and type, areas affected, and surface storm evolution. In conjunction with the monthly *SD* publication, mean sea level pressure (MSLP) maps, created with National Centers for Environmental Prediction Climate Forecast System Reanalysis (CFSR; Saha et al. 2010) data, were used to distinguish events from one another when monthly *SD* publication reports were close in time and the details provided in the monthly *SD* publication were insufficient for distinguishing one event from another.

Compiling all of the transition season Northeast events featuring frozen precipitation aided in determining the objective thresholds needed to categorize events as major transition season Northeast snowstorms. Objective thresholds unique to major transition season Northeast snowstorms were determined because heavy, wet snow tends to occur during the transition seasons. As a result of the heavy, wet snow, lesser accumulations occurring during the transition seasons can result in greater disruption than if the same accumulation occurred during the winter season. The compiled events were used to determine the objective thresholds by performing a subjective ranking with respect to the spatial extent of both socioeconomic impact and snowfall accumulation. After ranking the events, common snowstorm characteristics were identified, leading to a preliminary definition. The definition was finalized after discussion with the National Weather Service (NWS) Albany focal points, Neil Stuart and Thomas Wasula, and consideration of a parallel definition used in the ice storm classification of Castellano (2012), who utilized the monthly *SD* publication for identifying and classifying ice storms. The finalized definition is as follows: to be objectively defined as a major transition season Northeast snowstorm, an event in the monthly *SD* publication must have at least three separate county warning areas (CWAs) report: "Heavy Snow" (HS), "Winter Storm" (WS), "Blizzard" (B), or a combination of any of the three. Additionally, WS and B reports were required to have snowfall accumulations that met or exceeded the 12-h snow warning criterion threshold for the reporting CWA. The 12-h snow warning criterion thresholds were obtained from the March 2015 NWS Mount Holly map shown in Fig. 2.1.

Application of the finalized objective definition, which was performed to construct a case list, began with identifying each event that included at least one report of HS, WS, or B from the compiled monthly *SD* publication frozen precipitation events. Subsequently, for each event, the monthly *SD* publication was reutilized, along with the CWA layout and county lines provided by the NWS Geographical Information System (GIS) - Advanced Weather Interactive Processing System (AWIPS) Shapefile Database (http://www.nws.noaa.gov/geodata/), to record details regarding the affected states, CWAs, and counties; the number of HS, WS, or B reports; and the snowfall accumulations for WS or B reports. The recorded details were then used to determine if the objective definition applied to each event. While reutilizing the monthly *SD* publication, the

Northeast domain, corresponding to NCEI's Northeast region, was expanded to incorporate data that accounted for the portions of the CWAs (i.e., Pittsburgh and Sterling) that extend into Ohio, Virginia, West Virginia, and Washington, DC. Figure 2.2 illustrates the expanded Northeast domain to which the definition was applied.

Although the years 1979–2013 were initially the intended time period for the case list of major transition season Northeast snowstorms, the years 1979–1982 were excluded from the final case list, restricting the final case list to the years 1983–2013. The years 1979–1982 were excluded because numerous monthly *SD* publication reports were incomplete in the respect that notable temporal gaps existed within the snowfall data record. Similarly, Branick (1997) reported notable temporal gaps during the early and middle 1980s in the monthly *SD* publication when he used it to compile all winter weather events for the continental U.S. during 1982–1994. Using the years 1983–2013, the application of the objective definition during the transition seasons yielded 72 spring cases and 24 fall cases for a total of 96 cases. A historic case with significant socioeconomic impact, the 4 October 1987 snowstorm, was added to the case list because the objective definition would have likely detected the snowstorm if not for reporting inconsistences in the early years of the analyzed time period. An analysis of total snowfall accumulation for the October 1987 snowstorm by Bosart and Sanders (1991) (Fig. 2.3) supported the addition of this snowstorm to the case list because the analysis displayed total snowfall accumulation values that met or exceeded the 12-h snow warning criterion threshold for three CWAs. The addition of the October 1987 snowstorm to the case list yielded a total of 97 cases resulting from 72 cases in the spring (Table 2.1) and 25 cases in the fall (Table 2.2).

2.2 Case Categorization

After constructing the case list of major transition season Northeast snowstorms, a preliminary analysis for each of the 97 cases was performed in an effort to identify similar synoptic-to-mesoscale flow patterns to serve as the basis for compositing the cases. The preliminary analysis utilized CFSR-derived maps and snowfall accumulation maps. The CFSR-derived maps used in this analysis were created with the NCAR Command Language (NCL; The NCAR, 2016) using the CFSR data with a temporal resolution of 6 h and a horizontal resolution of 0.5°. The snowfall accumulation maps were created with Quantum GIS (QGIS; QGIS Development Team, 2015) using NCEI Global Historical Climatology Network Daily (GHCN-D; Menne et al. 2012) data, Global Multi-resolution Terrain Elevation Data 2010 (Danielson and Gesch 2011), and boundaries of regions from NWS GIS - AWIPS. The preliminary analysis revealed that the characteristic patterns of lower-tropospheric cold air that coincided with areas of heavy snowfall could serve as distinguishing characteristics for composite categories.

The composite categories included a baroclinic zone category (49 cases), a cold pool category (36 cases) and an unclassified category (12 cases). The baroclinic zone category contained cases characterized by a gradient in the 1000–850-hPa thickness field that coincided with an area of heavy snowfall. The cold pool category contained cases characterized by a local minimum (i.e., a cold pool) in the 1000–850-hPa thickness field that coincided with an area of heavy snowfall. Additionally, the cold pool had to be present for at least 6 h while maintaining thicknesses below 1310 m. Thicknesses below 1310 m were required in order to identify cold pools that either supported frozen precipitation or were close to supporting frozen precipitation. The unclassified category contained cases that either: 1) did not exhibit the characteristics of the cold pool category or the baroclinic zone category based on the 1000–850-hPa thickness field, or

2) exhibited dynamics differing from those of extratropical cyclones. For example, during one unclassified case, the 25–26 October 2005 snowstorm, the National Hurricane Center noted that a tropical cyclone transitioned to an extratropical cyclone (Pasch et al. 2006).

The baroclinic zone and cold pool categories were further divided into subsets within their respective category in order to document: 1) the planetary-to-mesoscale flow patterns of two unique clusters of snowstorms in the baroclinic zone category through the use of maps, and 2) cold pool formation and maintenance in various thermodynamic environments through the use of soundings. The baroclinic zone category was divided into two subsets based on the average 1000–850-hPa thermal wind direction calculated over a 6° longitude by 5° latitude box to the northwest of the surface cyclone center during the case days of the snowstorm. Case days of the snowstorm were defined as the 24-h period beginning at 0600 UTC for each day of the snowstorm as identified by the monthly *SD* publication. Section 2.5 further elaborates on the process used to calculate the average thermal wind direction for each case in the baroclinic zone category. The two subsets were comprised of southwesterly thermal wind cases (29 cases), which included cases with an average thermal wind direction ≥ 202.5° and < 247.5°, and westerly thermal wind cases (20 cases), which included cases with an average thermal wind direction ≥ 247.5° and < 292.5°.

The cold pool category was divided into four subsets based on the precipitation type and temperature observed at the surface station closest to the point of maximum snowfall accumulation within the cold pool for each case. The point of maximum snowfall accumulation was identified in QGIS using GHCN-D, NWS GIS - AWIPS, and CFSR data. Precipitation type and temperature were obtained through METAR observations archived by Iowa State University (https://mesonet.agron.iastate.edu/archive/) and were considered during the 12-h time period that ended at the time when the cold pool first appeared over the identified point of snowfall accumulation. The four subsets were comprised of changeover cases (7 cases), wet snow cases (19 cases), normal snow cases (5 cases), and unclassified cases (5 cases). The definitions of the four cold pool subsets are as follows:

- *Changeover case:* During the analyzed 12-h time period, a changeover in precipitation type to snow was required.
- *Wet snow case:* During the analyzed 12-h time period, the initial precipitation type was snow, and while it was snowing the surface temperature remained above −2.5°C.
- *Normal snow case:* During the analyzed 12-h time period, the initial precipitation type was snow, and while it was snowing the surface temperature remained below −2.5°C.
- *Unclassified case:* During the analyzed 12-h time period, the conditions of the other subsets were not met.

The temperature value of −2.5°C was selected for use in the cold pool subset definitions after dividing the cold pool category into subsets with similar precipitation characteristics (e.g., precipitation only in the form of snow) and temperature characteristics (e.g., temperatures above or near freezing), and thus was a value unique to the METAR observations for the 36 cold pool cases. Two cases in the wet snow subset and two cases in the normal snow subset featured temperatures that approached −2.5°C. Despite temperatures approaching −2.5°C, the use of the monthly *SD* Publication and QGIS confirmed the division of the cases into their respective subset. For the two cases in the wet snow subset, the monthly *SD* Publication reported heavy, wet snow, and QGIS revealed that the locations of the heavy, wet snow were less than 50 km away from the identified points of snowfall accumulation. For the two cases in the normal snow subset, the monthly *SD* Publication reported heavy, wet snow, but QGIS revealed that the locations of the heavy, wet snow were more than 500 km away from the identified points of snowfall accumulation.

2.3 Atmospheric Rivers

The methodology of Lavers and Villarini (2015) was modified and incorporated into this study in order to: 1) identify AR axes objectively, and 2) associate points of snowfall accumulation with ARs. A modified version of their methodology was incorporated into this study because their methodology was designed for the central and eastern U.S., which overlapped with the domain used in this study (i.e., the northeast U.S.; Fig. 2.2). The modified methodology of Lavers and Villarini (2015) used in this study that objectively identified AR axes (hereafter referred to as an algorithm) was applied to CFSR-derived vertically integrated water vapor transport (IVT) fields computed for the 1000–300-hPa layer for all 97 cases on the case list. After applying the algorithm, the results were quality checked manually to ensure that only AR axes associated with the surface cyclone of interest were considered for analysis. These objectively identified AR axes were then used to associate points of snowfall accumulation with ARs from an Eulerian perspective. The methodology to make this association was based on methodology from Lavers and Villarini (2015), as mentioned previously, along with the methodology from Mahoney et al. (2016). From an Eulerian perspective, a point of snowfall accumulation was associated with an AR if that point of snowfall accumulation was 250 km or closer to at least one point on an AR axis at any time during the 24-h period beginning at 0600 UTC on the day(s) of precipitation.

The algorithm that objectively identified AR axes followed several steps. The first step of the algorithm identified the point of maximum IVT along 40°N between 50°–100°W and then determined if the IVT value at that point exceeded the minimum IVT threshold of 367.8 kg m^{-1} s^{-1}. The value of the minimum IVT threshold was calculated by Lavers and Villarini (2015) through statistical analysis. If the minimum IVT threshold was exceeded, the algorithm proceeded to the second step. The second step of the algorithm repeated the first step of the algorithm with the exception of searching along different latitudes. The second step searched north from 40°N to 50°N and south from 40°N to 15°N in 0.5° intervals. If the algorithm found 19 or more sequential points of maximum IVT to the north and/or south of 40°N that exceeded the minimum IVT threshold, and the longitude difference between sequential points did not exceed 4° longitude, then an AR was identified, and its axis was defined by the 19 or more sequential points of maximum IVT. A minimum of 19 sequential points of maximum IVT to the north and/or south of 40°N were required in order to be consistent with Lavers and Villarini (2015), who modified their methodology from Lavers and Villarini (2013). Lavers and Villarini (2013) stated that their number of grids spaced by 0.7°, when considered along a line of longitude south of 40.35°N, covered an approximate length of 1000 km. In this study, 19 sequential points separated by 0.5° directly south of 40°N equated to an approximate length of 1000 km.

2.4 Climatology

The climatology of major transition season Northeast snowstorms has two primary foci: 1) climatological characteristics of major transition season Northeast snowstorms, and 2) climatological characteristics of ARs objectively identified during the periods of the cases on the case list. For both foci, the 97 cases on the case list were grouped by season, month, and lower-tropospheric cold air category. Using these groups, the temporal and spatial characteristics of this class of snowstorms were assessed through monthly distribution plots, time series plots, and spatial distribution plots. To address the first focus, spatial distribution plots were created with QGIS using NWS GIS - AWIPS and GHCN-D data. These plots displayed the number of cases in one of the aforementioned groups that occurred in each county where GHCN-D snowfall accumulation values for the case met or exceeded the 12-h heavy snow warning criterion threshold for the respective CWA of each county. Additionally, QGIS, NWS GIS - AWIPS, and CFSR data were used to create plots that displayed the number of cold pools in each county at the initial and midpoint time of the cold pool for the cases in the cold pool category. To address the second focus, spatial distribution plots were created with NCL using CFSR data. These plots illustrated the AR axis density as a function of the aforementioned groups. Additionally, QGIS, NWS GIS - AWIPS, GHCN-D, and CFSR data were used to create plots that displayed the number of cases in a CWA where at least one point of snowfall accumulation that met or exceeded the 12-h heavy snow warning criterion threshold was associated with an AR.

2.5 Composite Analyses

2.5.1 Composite Map Analysis

Composite maps were created with CFSR data to document the planetary-to-mesoscale flow patterns occurring prior to and during the baroclinic zone and cold pool categories of major transition season Northeast snowstorms. For both categories, the characteristic pattern of lower-tropospheric cold air provided the basis for case-centered composites in both location and time. The center location and the center time (t_0) were selected to represent a time of heavy precipitation occurring within the baroclinic zone to the northwest of the surface cyclone or occurring within the cold pool. The use of a center time that represented a time of heavy precipitation for the composite categories allowed for comparison between the composite categories. The center location for both subsets of the baroclinic zone category was the minimum MSLP of the surface cyclone, so that the northwest sectors of the surface cyclones (used to define the 1000–850-hPa thickness gradient and thermal wind) aligned with each other. The time of the strongest 1000–850-hPa thickness gradient located to the northwest of the surface cyclone center served as the center time, t_0, for the baroclinic zone category composites because precipitation was assumed to be heavy at this time. For the cold pool category, the center location was the minimum 1000–850-hPa thickness of the cold pool at the midpoint time of the cold pool. The midpoint time of the cold pool served as the center time, t_0, for the composite category because precipitation was assumed to be heavy at this time. In each composite category or subset, the composite center consisted of the averaged location of all the center locations of the cases in the category or subset. Finally, for each composite category or subset, derived fields, such as Q-vectors, were calculated for each case and then composited.

For each case in the cold pool category, t_0 was identified via manual analysis, while for each case in the baroclinic zone category, t_0 was identified using the following algorithm. The algorithm calculated the 1000–850-hPa thickness gradient and the thermal wind over a 6°

longitude by 5° latitude box with a center located 1° west and 2° north of the surface cyclone center at every time during each case. If the surface cyclone consisted of a primary low-pressure center and a secondary low-pressure center, then the low-pressure center was selected that allowed for the thickness gradient and thermal wind to be calculated nearest to the heavy snowfall region as indicated by the monthly *SD* publication. After the algorithm performed the aforementioned calculations, the algorithm identified the time of the strongest 1000–850-hPa thickness gradient that occurred when the box to the northwest of the surface cyclone center had any degree of overlap with the Northeast region bounded by 82.5°–67.0°W and 37.5°–47.5°N. Overlap was required to constrain the identified time of the strongest 1000–850-hPa thickness gradient over or near the Northeast domain shown in Fig. 2.2. Additionally, the average thermal wind over the box was averaged over all of the times when any degree of overlap occurred between the box and the Northeast region in the previously specified bounds. The resulting averaged value led to the division of the baroclinic zone category cases into the southwesterly thermal wind and westerly thermal wind subsets described in section 2.2.

2.5.2 Composite Sounding Analysis

For each of the three cold pool subsets described in section 2.2, composite soundings were created with CFSR data in order to document cold pool formation and maintenance in various thermodynamic environments. The composite soundings for each cold pool subset were created by averaging the vertical profiles over the point of maximum snowfall accumulation within the cold pool for each case. The time when the cold pool first appeared over the aforementioned point of maximum snowfall accumulation served as t_0 for the composite soundings. As in section 2.5.1, derived fields were first calculated for each case and then composited.

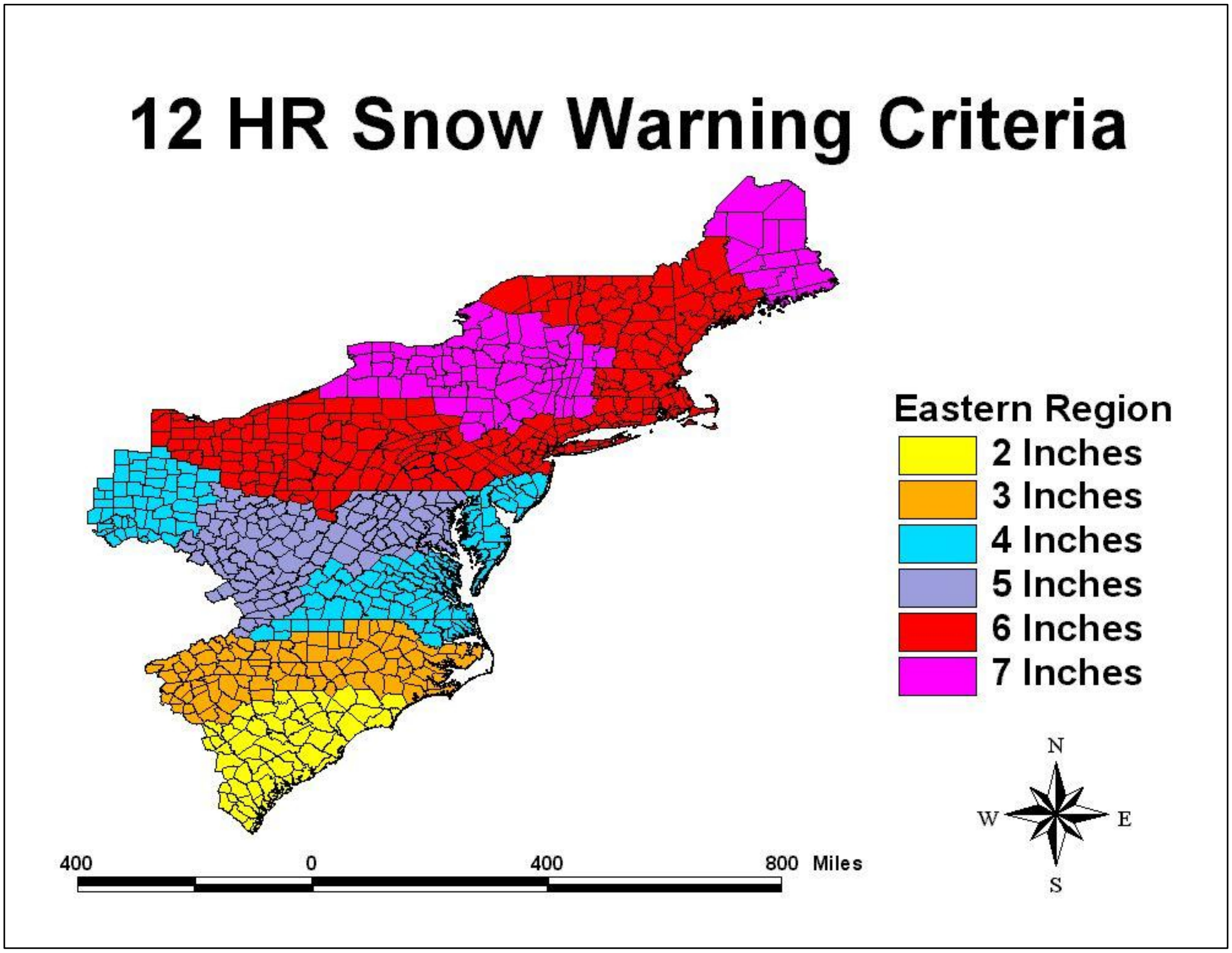

Fig. 2.1 The March 2015 NWS Mount Holly map displaying the 12-h snow warning criterion for each county. The 12-h snow warning criterion for each county reflects the 12-h snow warning criterion of its respective CWA. The March 2015 NWS Mount Holly map was reproduced from http://www.erh.noaa.gov/phi/WinterMaps/12hrsnwwrng.jpg.

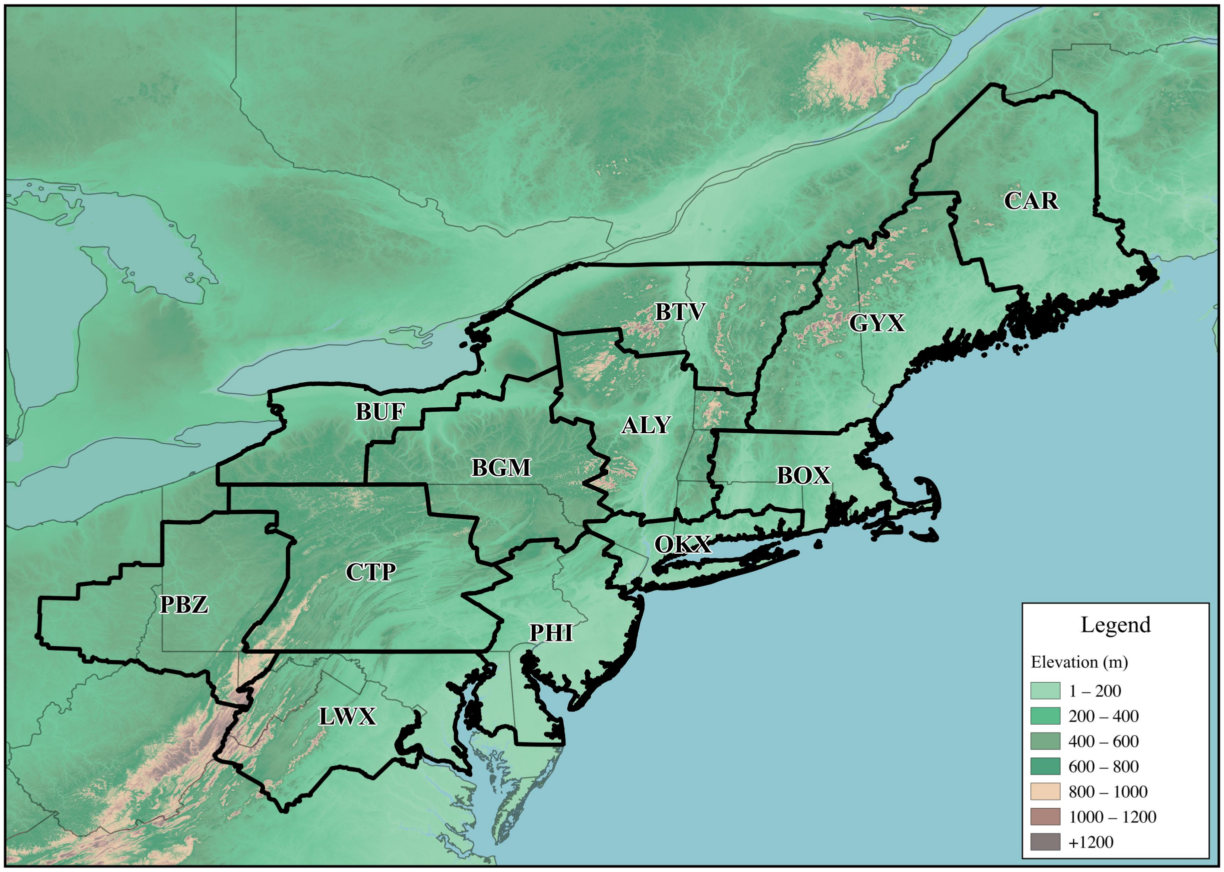

Fig. 2.2 The CWAs (dark black lines) comprising the Northeast domain to which the objective definition of a major transition season Northeast snowstorm was applied. Terrain (shaded, m) is also shown along with U.S. state and Canadian provincial boundaries (thin black lines).

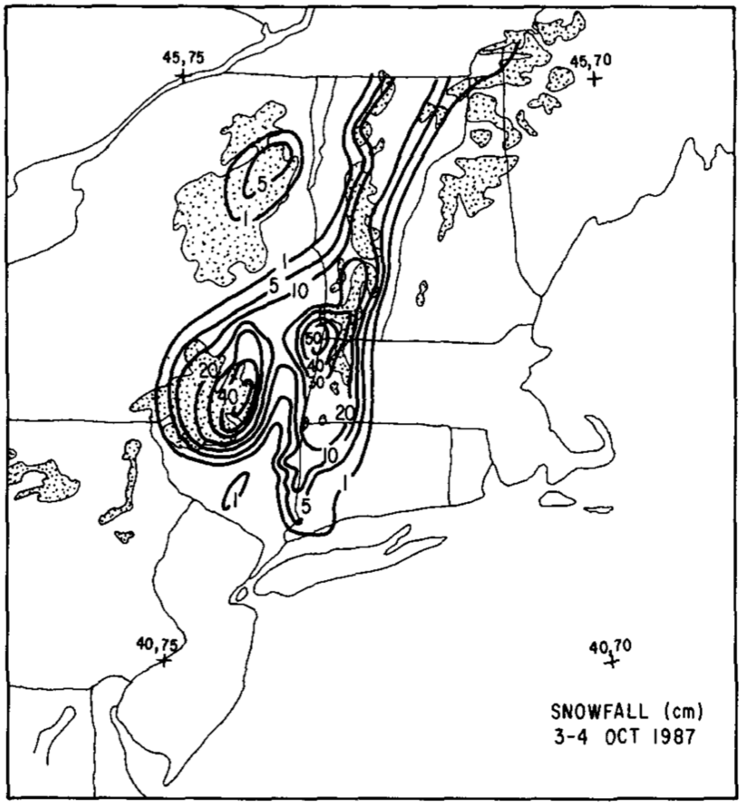

Fig. 2.3 Analysis of total snowfall accumulation for the 3–4 October 1987 snowstorm. Regions of elevation exceeding 600 m are indicated by stippling [Fig. 2 and caption adapted from Bosart and Sanders (1991)].

Case No.	Snowstorm Date(s)	Case No.	Snowstorm Date(s)
1	19–20 Apr 1983	37	16–17 Mar 2000
2	8–9 Mar 1984	38	8–10 Apr 2000
3	28–30 Mar 1984	39	4–7 Mar 2001
4	6–7 Mar 1986	40	9–10 Mar 2001
5	3–5 Apr 1987	41	21–23 Mar 2001
6	13–15 Mar 1991	42	29–31 Mar 2001
7	10–12 Mar 1992	43	20–21 Mar 2002
8	18–19 Mar 1992	44	24–27 Mar 2002
9	22–23 Mar 1992	45	6 Mar 2003
10	4–6 Mar 1993	46	30–31 Mar 2003
11	12–14 Mar 1993	47	3–5 Apr 2003
12	23–25 Mar 1993	48	16–17 Mar 2004
13	1–2 Apr 1993	49	18–19 Mar 2004
14	22–23 Apr 1993	50	4–6 Apr 2004
15	2–4 Mar 1994	51	8–9 Mar 2005
16	9–10 Mar 1994	52	11–13 Mar 2005
17	15–17 Mar 1994	53	23–24 Mar 2005
18	18 Mar 1994	54	2–3 Apr 2005
19	21–23 Mar 1994	55	2 Mar 2006
20	8–9 Mar 1995	56	4–5 Apr 2006
21	2–3 Mar 1996	57	1–3 Mar 2007
22	7–8 Mar 1996	58	6–7 Mar 2007
23	7–8 Apr 1996	59	16–18 Mar 2007
24	9–11 Apr 1996	60	4–5 Apr 2007
25	5–6 Mar 1997	61	11–13 Apr 2007
26	14–15 Mar 1997	62	15–17 Apr 2007
27	31 Mar–1 Apr 1997	63	7–9 Mar 2008
28	17–19 Apr 1997	64	18–21 Mar 2008
29	14–15 Mar 1998	65	1–2 Mar 2009
30	21–22 Mar 1998	66	6–7 Mar 2011
31	3–4 Mar 1999	67	22–24 Mar 2011
32	6–8 Mar 1999	68	1–2 Apr 2011
33	9–10 Mar 1999	69	22–23 Apr 2012
34	14–16 Mar 1999	70	5–9 Mar 2013
35	21–23 Mar 1999	71	17–20 Mar 2013
36	11–12 Mar 2000	72	24–25 Mar 2013

Table 2.1 List of objectively identified major transition season Northeast snowstorms occurring during spring (March–May) 1983–2013.

Case No.	Snowstorm Date(s)
1	18–19 Nov 1986
2	4 Oct 1987
3	10–12 Nov 1987
4	22–23 Nov 1989
5	31 Oct–2 Nov 1993
6	14–15 Nov 1995
7	29 Nov 1995
8	26–27 Nov 1996
9	13–15 Nov 1997
10	22 Nov 1997
11	14–18 Nov 1999
12	28–30 Oct 2000
13	5–7 Nov 2002
14	16–18 Nov 2002
15	26–27 Nov 2002
16	25–26 Oct 2005
17	22–23 Nov 2005
18	24 Nov 2005
19	16–17 Nov 2007
20	28–29 Oct 2008
21	24–26 Nov 2008
22	28–30 Oct 2011
23	22–23 Nov 2011
24	7–8 Nov 2012
25	26–27 Nov 2013

Table 2.2 List of objectively identified major transition season Northeast snowstorms occurring during fall (September–November) 1983–2013.

3. Climatology Analysis

The climatology of major transition season Northeast snowstorms is presented first with cases grouped by temporal characteristics (i.e., season or month) in section 3.1 and second with cases grouped by lower-tropospheric cold air pattern (i.e., the Baroclinic Zone: Southwesterly Thermal Wind subset, the Baroclinic Zone: Westerly Thermal Wind subset, and the Cold Pool category) in section 3.2.

3.1 Temporal Characteristics

Figure 3.1 displays the number of spring and fall major transition season Northeast snowstorms as a function of year for 1983–2013. During 1983–2013, interannual variability was evident for both spring and fall seasons. In general, few snowstorms occurred during the 1980s, the early 1990s, and the late 2000s (including 2010). Conversely, many snowstorms occurred during the mid/late 1990s, the early/mid 2000s, and the early 2010s (excluding 2010). These observations are consistent with analysis of Kocin and Uccellini (2004b, pp. 10–39); they noted reduced snowfall in the late 1980s and the early 1990s and enhanced snowfall during the mid 1990s when they analyzed a 5-year running mean of the seasonal snowfall for 18 locations in the eastern Northeast during 1900–2003. During 1983–2013, the maximum number of snowstorms observed during spring occurred in 2007 (six snowstorms), and the maximum number of snowstorms observed during fall occurred in 2002 and 2005 (three snowstorms) (Fig. 3.1). The minimum number of snowstorms observed during spring and fall was zero, which happened for both spring and fall during 1985, 1988, 1990, and 2010 (Fig. 3.1). In addition to revealing interannual variability, Fig. 3.1 reveals a predominance of spring snowstorms when compared to fall snowstorms. During 1983–2013 (31 spring and fall seasons), 72 spring snowstorms and 25 fall snowstorms occurred. On average two snowstorms were observed during spring, and one snowstorm was observed during fall. The monthly distribution of the snowstorms (Fig. 3.2) shows that most of the spring snowstorms occurred during March (55 snowstorms) followed by April (17 snowstorms). The monthly distribution also shows that most of the fall snowstorms occurred during November (19 snowstorms) followed by October (6 snowstorms) (Fig. 3.2). No major transition season Northeast snowstorms occurred in either May or September.

For each month that featured a major transition season Northeast snowstorm, Fig. 3.3 illustrates the spatial distribution of cases with heavy snowfall. Specifically, Fig. 3.3 displays the number of cases in each county where GHCN-D snowfall accumulation values for a case met or exceeded the 12-h heavy snow warning criterion threshold for the respective CWA of each county. The spatial distributions of cases with heavy snowfall for the months of March, April, October, and November reveal two common signals (Figs. 3.3a–d). The first common signal is the high occurrence of cases with heavy snowfall in regions of elevated terrain (see Fig. 2.2 for a terrain map). The second common signal is the low occurrence of cases with heavy snowfall in the southeastern portion of the Northeast domain, which includes Virginia, Maryland, Delaware, and New Jersey. For the months of March, April, and November, a latitudinal gradient of cases with heavy snowfall is largely evident; the number of cases with heavy snowfall generally increases as latitude increases (Figs. 3.3a,b,d). However, regions of elevated terrain interrupt the latitudinal gradient because of the high occurrence of cases with heavy snowfall in those regions. These results are similar to those of Kocin and Uccellini (2004b, pp. 10–39) who analyzed mean seasonal snowfall for the Northeast during 1961–1990 and generally observed a latitudinal gradient that was interrupted by regions of elevated terrain.

Table 3.1 presents the AR fraction for each month, and Fig. 3.4 displays the AR axis density as a function of month. The AR fraction for each month was calculated by dividing the number of case periods with an identified AR during all case days in a month by the total number of case periods during all case days in that month. As in section 2.2, case days of a snowstorm correspond to the 24-h period beginning at 0600 UTC for each day of the snowstorm as identified by the monthly *SD* publication. A case period refers to a 6 h time interval of the CFSR data, which was used in identifying ARs. The AR fractions indicate the frequency of observed ARs during the snowstorms in each month; thus a high AR fraction (Table 3.1) can signify that ARs are frequently observed during snowstorms in a month even if the values of AR axis density for that month appear low, as in October (Fig. 3.4c). Table 3.1 reveals that all of the months have AR fractions over 50%, which indicates that ARs are frequently observed during the snowstorms in each month and suggests that ARs are characteristic features associated with major transition season Northeast snowstorms.

The greatest AR fraction occurs in October (71.0%) followed by April (68.5%) (Table 3.1). The greatest AR fraction in October indicates that ARs are most frequent during October snowstorms when compared to March, April, and November snowstorms. Figure 3.4c shows that the AR axes during October snowstorms are concentrated over the western North Atlantic Ocean. Figure 3.4c also shows that the AR axis density within the Northeast domain is low during October snowstorms; only 1–5 unique AR axes in a 250 km radius occur over eastern Maine (Fig. 3.4c). The low AR axis density over the Northeast domain suggests that the ARs observed during October snowstorms may not be influential in terms of moisture transport into the Northeast domain. The lowest AR fraction occurs in March (56.8%) (Table 3.1) and indicates that ARs are least frequent during March snowstorms when compared to April, October, and November snowstorms. Although ARs are least frequent during March snowstorms, March features the highest AR axis density over the Northeast domain (approximately 60–70 unique AR axes in a 250 km radius occur over the Northeast coast; Fig. 3.4a) suggesting that the observed ARs are influential in terms of moisture transport into the Northeast domain.

3.2 Lower-Tropospheric Cold Air Pattern

Figure 3.5 presents the monthly distribution of major transition season Northeast snowstorms according to lower-tropospheric cold air pattern. A prominent signal in Fig. 3.5 is the predominance of Cold Pool category snowstorms in April (11 snowstorms), whereas only several snowstorms in April are in the Baroclinic Zone category (3 snowstorms). March also features a notable number of snowstorms in the Cold Pool category (19 snowstorms). However, the majority, approximately two-thirds, of the snowstorms in March are in the Baroclinic Zone category (33 snowstorms). Similarly, the majority, approximately two-thirds, of the snowstorms in November are in the Baroclinic Zone category (12 snowstorms).

Figure 3.6 shows the number of cold pools in each county in the Northeast domain at the initial time of the cold pool and at the midpoint time of the cold pool for the cases in the Cold Pool category. At the initial time of the cold pool, there is a widespread occurrence of cold pools, where the majority of the counties in the Northeast domain experience at least one cold pool (Fig. 3.6a). Many of the cold pools are located along and to the leeward side of the Appalachian Mountains and also along the coasts of Lake Erie and Lake Ontario. Local maxima of cold pool number often occur in regions of elevated terrain and include the White Mountains in Maine and New Hampshire; the Catskill Mountains in New York; the Allegany Plateau in western New York; and the Allegheny Mountains in Maryland, Pennsylvania, and the Virginias.

The occurrence of cold pools continues to be widespread at the midpoint time of the cold pool (Fig. 3.6b); similar to the initial time, the majority of the counties in the Northeast domain experience at least one cold pool. The number of counties that experience five or more cold pools increases from 30 counties at the initial time to 96 counties at the midpoint time. This increase in cold pool occurrence is likely attributable to an increase in the areal extent of the cold pools from their initial time to their midpoint time. At the midpoint time, local maxima of cold pool number are generally located in regions of elevated terrain and are primarily concentrated in eastern New York and New England (Fig. 3.6b).

The spatial distribution of cases with heavy snowfall for each of the lower-tropospheric cold air patterns is illustrated in Fig. 3.7, which displays the number of cases in each county where GHCN-D snowfall accumulation values for a case met or exceeded the 12-h heavy snow warning criterion threshold for the respective CWA of each county. The lower-tropospheric cold air patterns share a commonality of high case occurrence in regions of elevated terrain (Figs. 3.7a–c). Apart from this commonality, the lower-tropospheric cold air patterns reveal different spatial distributions of cases with heavy snowfall. In the Baroclinic Zone: Southwesterly Thermal Wind subset (Fig. 3.7a), more cases with heavy snowfall occur inland than in coastal regions, especially in the southern portion of the Northeast domain. In the Baroclinic Zone: Westerly Thermal Wind subset (Fig. 3.7b), a high occurrence of cases with heavy snowfall is evident in two regions. One region extends along the Pennsylvania/New York border to coastal Massachusetts, and the second region extends from northern New York to coastal Maine. In the

Cold Pool category (Fig. 3.7c), a high occurrence of cases with heavy snowfall is concentrated in eastern New York and New England.

Comparing the spatial distribution of cases with heavy snowfall for each lower-tropospheric cold air pattern (Figs. 3.7a–c) reveals that the widest coverage of high case frequencies occurs in the Cold Pool category (Fig. 3.7c). The Cold Pool category features the most counties (146 counties) experiencing more than five cases with heavy snowfall, followed by the Baroclinic Zone: Southwesterly Thermal Wind subset (99 counties) and the Baroclinic Zone: Westerly Thermal Wind subset (25 counties). High case frequencies are also the most widespread along the I-95 corridor in the Cold Pool category (Fig. 3.7c) relative to the other lower-tropospheric cold air patterns (Figs. 3.7a,b). Because the I-95 corridor is a highly populated region with areally dense infrastructure, the potential for significant socioeconomic impact during Cold Pool category cases is especially large. The prevalence of high case frequencies in the Cold Pool category is likely attributable to the widespread nature of heavy snowfall occurring during Cold Pool category cases; more counties experience heavy snowfall, on average, during a Cold Pool case (approximately 58 counties) than during either a Baroclinic Zone: Southwesterly Thermal Wind case (approximately 47 counties) or a Baroclinic Zone: Westerly Thermal Wind case (approximately 30 counties). The prevalence of high case frequencies may also be attributable to the higher number of cases in the Cold Pool category (36 cases) when compared to either the Baroclinic Zone: Southwesterly Thermal Wind subset (29 cases) or the Baroclinic Zone: Westerly Thermal Wind subset (20 cases).

Table 3.2 contains the AR fraction for each lower-tropospheric cold air pattern, which was calculated during all case days of the snowstorms (calculated identically to the AR fraction in section 3.1 except replacing month with lower-tropospheric cold air pattern) and at the composite center time (t_0) of the cases (calculated identically to the AR fraction during all case days of the snowstorms except considering only the ARs identified at t_0; see section 2.5.1 for t_0 description). The highest AR fraction during all case days occurs in the Baroclinic Zone: Southwesterly Thermal Wind subset (71.3%) followed by the Cold Pool category (59.0%) (Table 3.2). The highest AR fraction in the Baroclinic Zone: Southwesterly Thermal Wind subset indicates that ARs are most frequent in this lower-tropospheric cold air pattern when compared to the other lower-tropospheric cold air patterns. The lowest AR fraction during all case days occurs in the Baroclinic Zone: Westerly Thermal Wind subset (47.5%) (Table 3.2) indicating that ARs are least frequent in this lower-tropospheric cold air pattern relative to the other lower-tropospheric cold air patterns. Similar to during all case days, at t_0 the Baroclinic Zone: Southwesterly Thermal Wind subset features the highest AR fraction (82.8%) of the lower-tropospheric cold air patterns (Table 3.2), indicating that ARs are most frequent at t_0 during the Baroclinic Zone: Southwesterly Thermal Winds subset when compared to the remaining lower-tropospheric cold air patterns. Dissimilar to during all case days, at t_0 the Cold Pool category features the lowest AR fraction (52.8%), indicating that ARs are least frequent in the Cold Pool category than in either subset of the Baroclinic Zone category at t_0 (Table 3.2).

During all case days, the Baroclinic Zone: Southwesterly Thermal Wind subset and the Cold Pool category are comparable in terms of their number of landfalling ARs in the Northeast domain (defined by an AR axis intersecting the Northeast domain in Fig. 2.2). Though comparable, the Cold Pool category exhibits slightly more landfalling ARs (66 ARs) than the Baroclinic Zone: Southwesterly Thermal Wind subset (58 ARs) over the Northeast domain during all case days. Consistently, the AR axis density plots show comparable values of maximum AR axis density over the Northeast domain for the Baroclinic Zone: Southwesterly

Thermal Wind subset (Fig. 3.8a) and the Cold Pool category (Fig. 3.8e), with slightly higher values evident in the Cold Pool category. During all case days, the Baroclinic Zone: Westerly Thermal Wind subset features notably fewer landfalling ARs (14 ARs) than the previous two lower-tropospheric cold air patterns. Consistently, the AR axis density plots show the lowest values of maximum AR axis density over the Northeast domain for the Baroclinic Zone: Westerly Thermal Wind subset (Fig. 3.8c) compared to the other two lower-tropospheric cold air patterns (Figs. 3.8a,e).

Table 3.3 displays the landfalling AR fraction at t_0 (calculated by dividing the number of case periods with a landfalling AR at t_0 by the total number of case periods at t_0) for each lower-tropospheric cold air pattern. Similar to during all case days, at t_0 the Baroclinic Zone: Westerly Thermal Wind subset features fewer landfalling ARs (two ARs) than either the Baroclinic Zone: Southwesterly Thermal Wind subset (five ARs) or the Cold Pool category (11 ARs) (Table 3.3). Consistently, the Baroclinic Zone: Westerly Thermal Wind subset has the lowest landfalling AR fraction of the lower-tropospheric cold air patterns. The highest landfalling AR fraction of the lower-tropospheric cold air patterns occurs in the Cold Pool (Table 3.3); the landfalling AR fraction comparison suggests that the identified ARs have the potential to be more influential in transporting moisture into the Northeast domain at t_0 of the cases in the Cold Pool category than in either subset of the Baroclinic Zone category. Consistent with the highest landfalling AR fraction occurring in the Cold Pool category, Fig. 3.8f shows that the Cold Pool category features the highest values of AR axis density over the Northeast domain compared to both subsets of the Baroclinic Zone category (Figs. 3.8b,d).

The region of high AR axis density in Fig. 3.8 has a prominent configuration in each lower-tropospheric cold air pattern, evident both during all case days and at t_0 of the cases. For both subsets in the Baroclinic Zone category, the core of high AR axis density extends from the southwest to the northeast in a linear configuration (Figs. 3.8a–d). For the Cold Pool category, the core of high AR axis density has a cyclonically curved configuration (Figs. 3.8e,f). The Cold Pool category is unique in that the core of high AR axis density curves toward the Northeast domain north of 40°N (Figs. 3.8e,f), suggesting moisture transport from ARs into the Northeast domain. The linear configuration for both subsets of the Baroclinic Zone category and the cyclonically curved configuration for the Cold Pool category were subjectively determined (not shown) to be the most common AR configurations observed during all case days in their respective subset or category and at t_0; however, there is a notable degree of variability in AR configuration present within each lower-tropospheric cold air pattern.

The ARs in each lower tropospheric cold air pattern were associated with points of heavy snowfall in order to determine the role of these ARs during major transition season Northeast snowstorms (see section 2.3 for the methodology used to make the associations). The points of heavy snowfall are defined as the points of observed snowfall accumulation (from GHCN-D data) for a case that met or exceeded the 12-h heavy snow warning criterion threshold for their respective CWA. These points of observed snowfall accumulation are referred to as points of heavy snowfall because their snowfall accumulation values are consistent with the values used in the definition of a major transition season Northeast snowstorm (refer to section 2.1 for the definition). As the snowfall accumulation for a case can span multiple days, only one day of snowfall at the point of snowfall accumulation had to meet the criterion of the association for the association to be made. The number of cases experiencing an association between at least one point of heavy snowfall and an AR was counted and presented in Fig. 3.9a. An association between at least one point of heavy snowfall and an AR will be referred to as "AR-influenced," and an "association fraction" refers to the ratio of AR-influenced cases to total cases.

Figure 3.9a shows that the highest association fraction (25 out of 36 cases; 69.4%) occurs in the Cold Pool category. The association fraction of the Baroclinic Zone: Southwesterly Thermal Wind subset (20 out of 29 cases; 69.0%) is comparable to that of the Cold Pool category. The high association fractions of the two lower-tropospheric cold air patterns suggest that ARs are important ingredients in areas of heavy snowfall as the majority of the cases (approximately two-thirds) in the two lower-tropospheric cold air patterns are AR-influenced. The lowest association fraction (5 out of 20 cases; 25.0%) occurs in the Baroclinic Zone: Westerly Thermal Wind subset, and the low association fraction suggests that ARs are a less frequent ingredient during this type of major transition season Northeast snowstorm.

In order to display the spatial distribution of AR-influenced cases, the number of cases in each CWA where at least at least one point of heavy snowfall was associated with an AR was counted for each lower-tropospheric cold air pattern (Figs. 3.9b–d). Here, an association fraction refers to the ratio of AR-influenced cases in a CWA to total cases with heavy snowfall in a CWA. For each lower-tropospheric cold air pattern, the highest association fractions generally occur in the New England CWAs, whereas the lower association fractions generally occur in the mid-Atlantic CWAs (Figs. 3.9b–d and embedded table). The CWAs in New England (i.e., BOX, BTV, CAR, and GYX) and also the CWA in eastern New York (ALY) have the highest association fractions in the Cold Pool category (Fig. 3.9d and embedded table) relative to the other lower-tropospheric cold air patterns (Figs. 3.9b,c and embedded table). The CWAs in the remainder of the Northeast domain (i.e., BGM, BUF, CTP, LWX, OKX, PBZ, and PHI) have the highest association fractions in the Baroclinic Zone: Southwesterly Thermal Wind subset (Fig.

3.9b and embedded table) relative to the other two lower-tropospheric cold air patterns (Figs. 3.9c,d and embedded table).

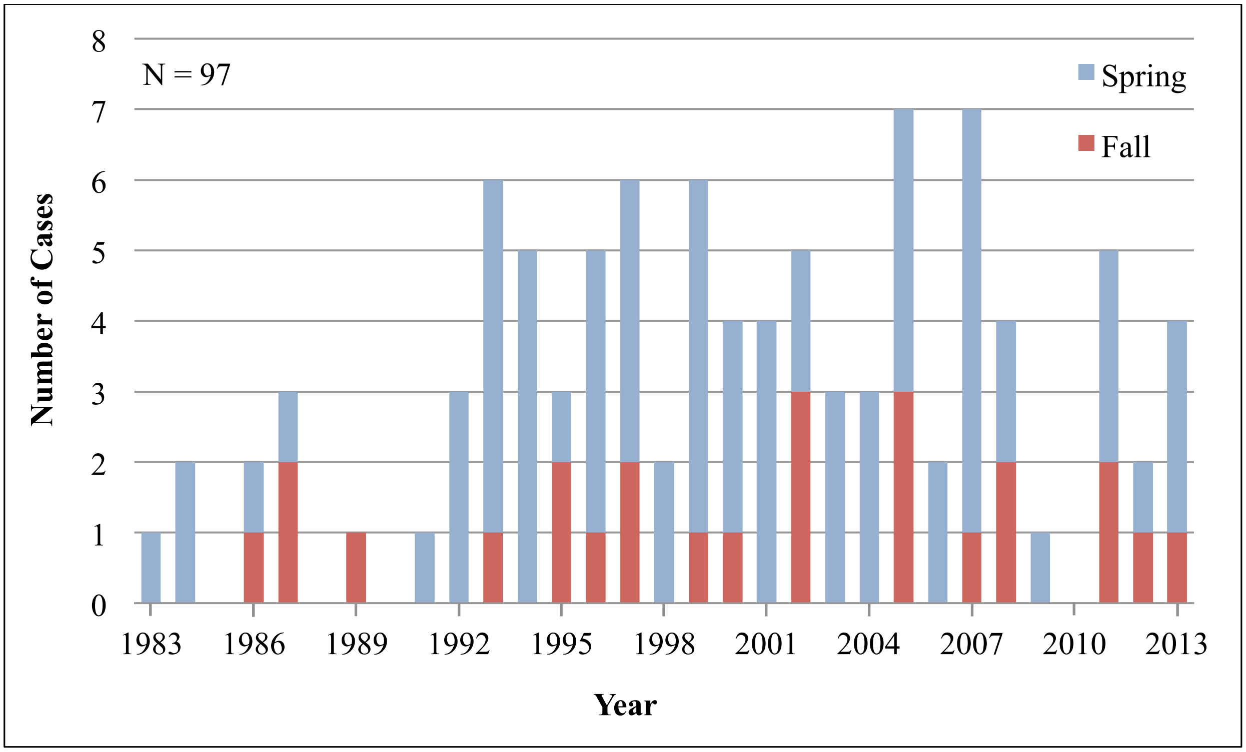

Fig. 3.1 Number of spring (blue) and fall (red) major transition season Northeast snowstorms as a function of year for 1983–2013.

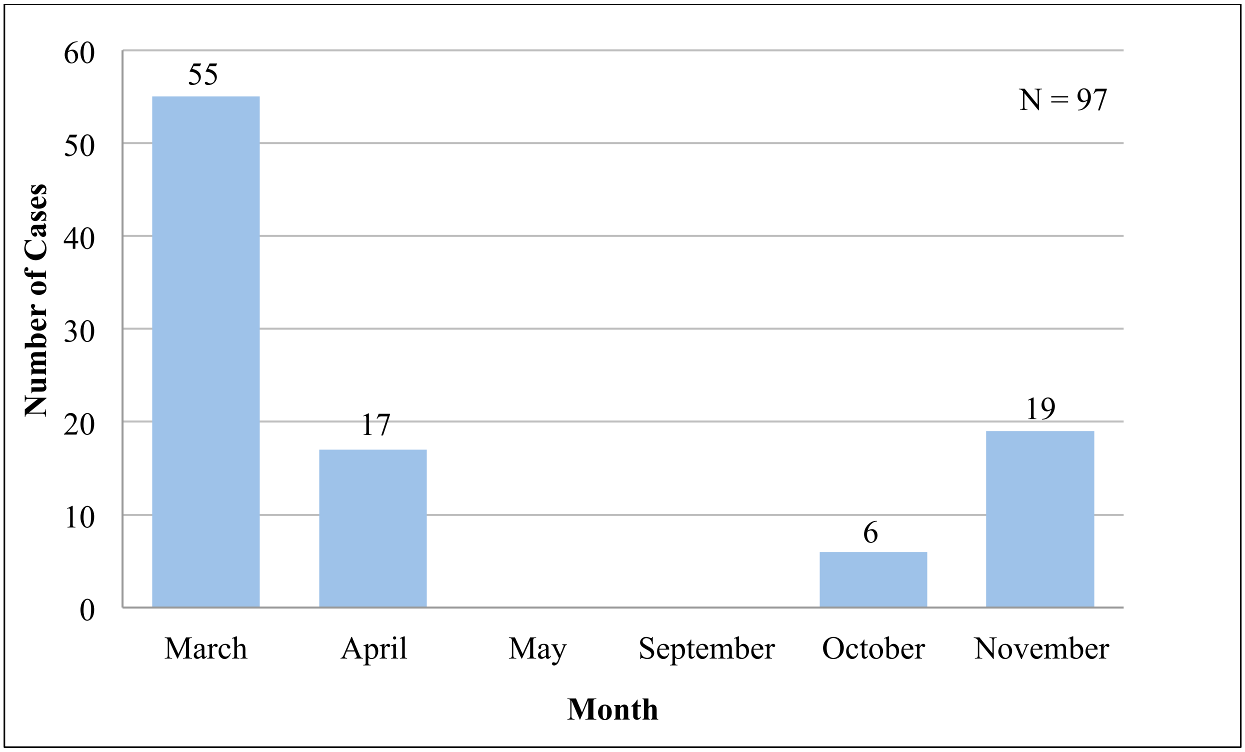

Fig. 3.2 Monthly distribution of major transition season Northeast snowstorms.

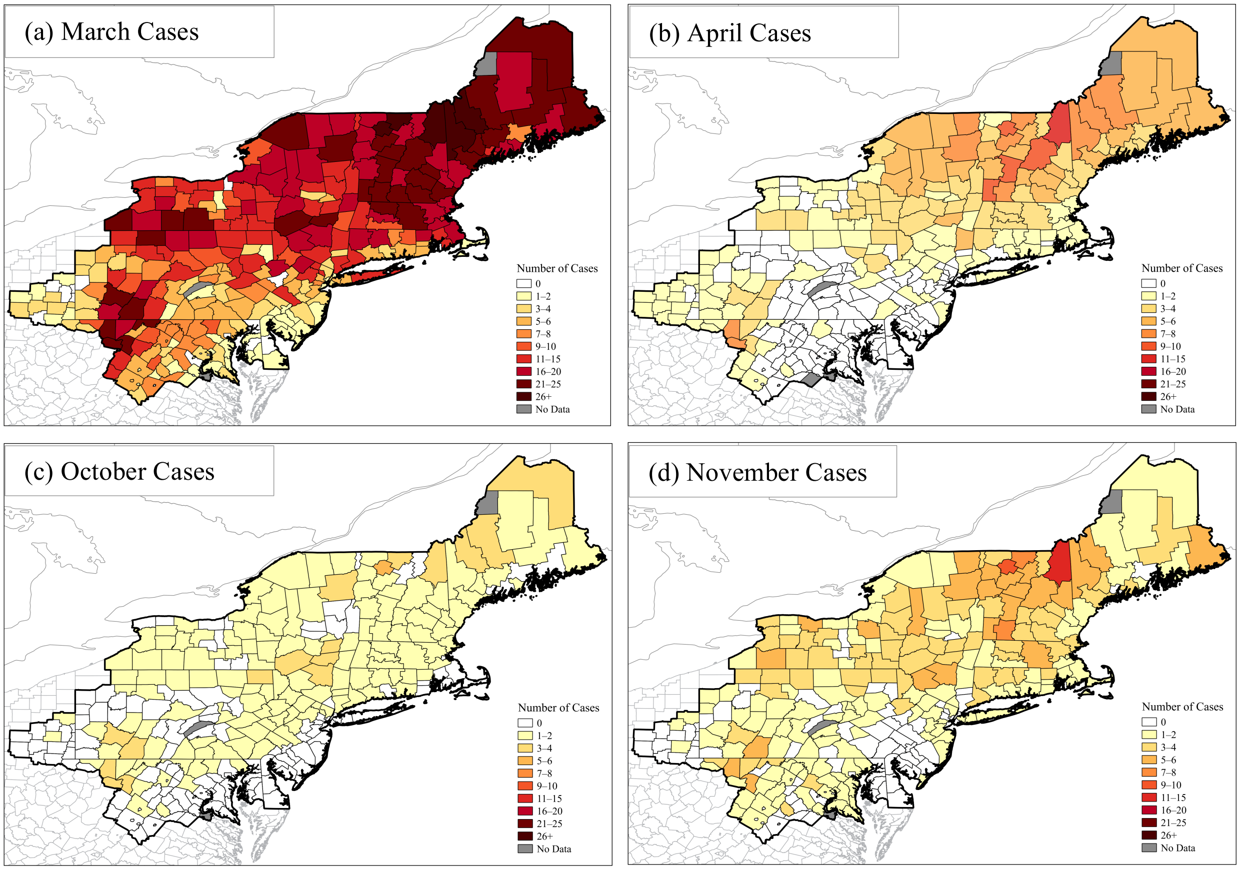

Fig. 3.3 Number of cases in each county (shaded) where GHCN-D snowfall accumulation values for a case met or exceeded the 12-h heavy snow warning criterion threshold for the respective CWA of each county for (a) March cases, (b) April cases, (c) October cases, and (d) November cases.

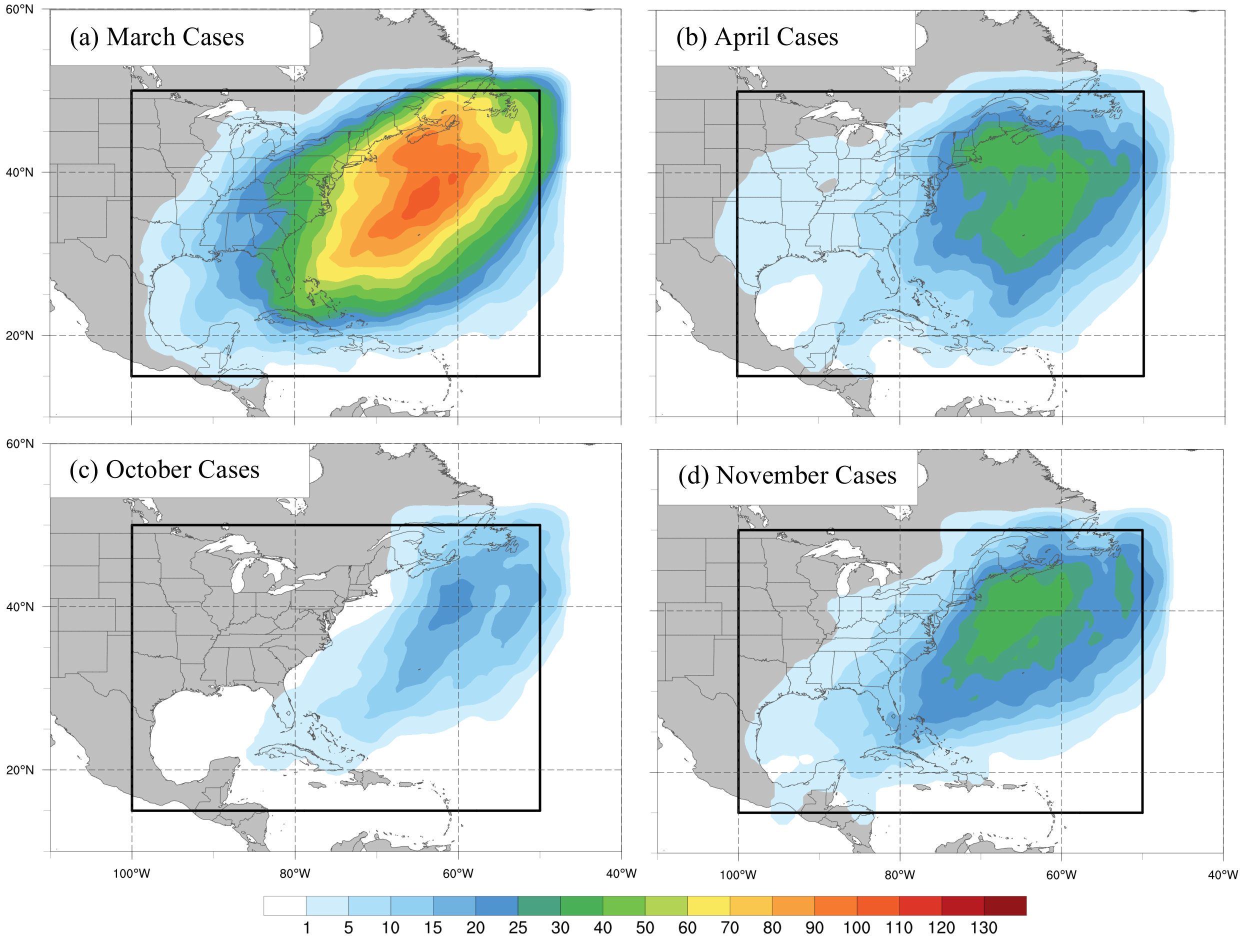

Fig. 3.4 AR axis density (shaded; number of unique ARs in a 250 km radius) within the domain bounded by the black box for (a) March cases, (b) April cases, (c) October cases, and (d) November cases.

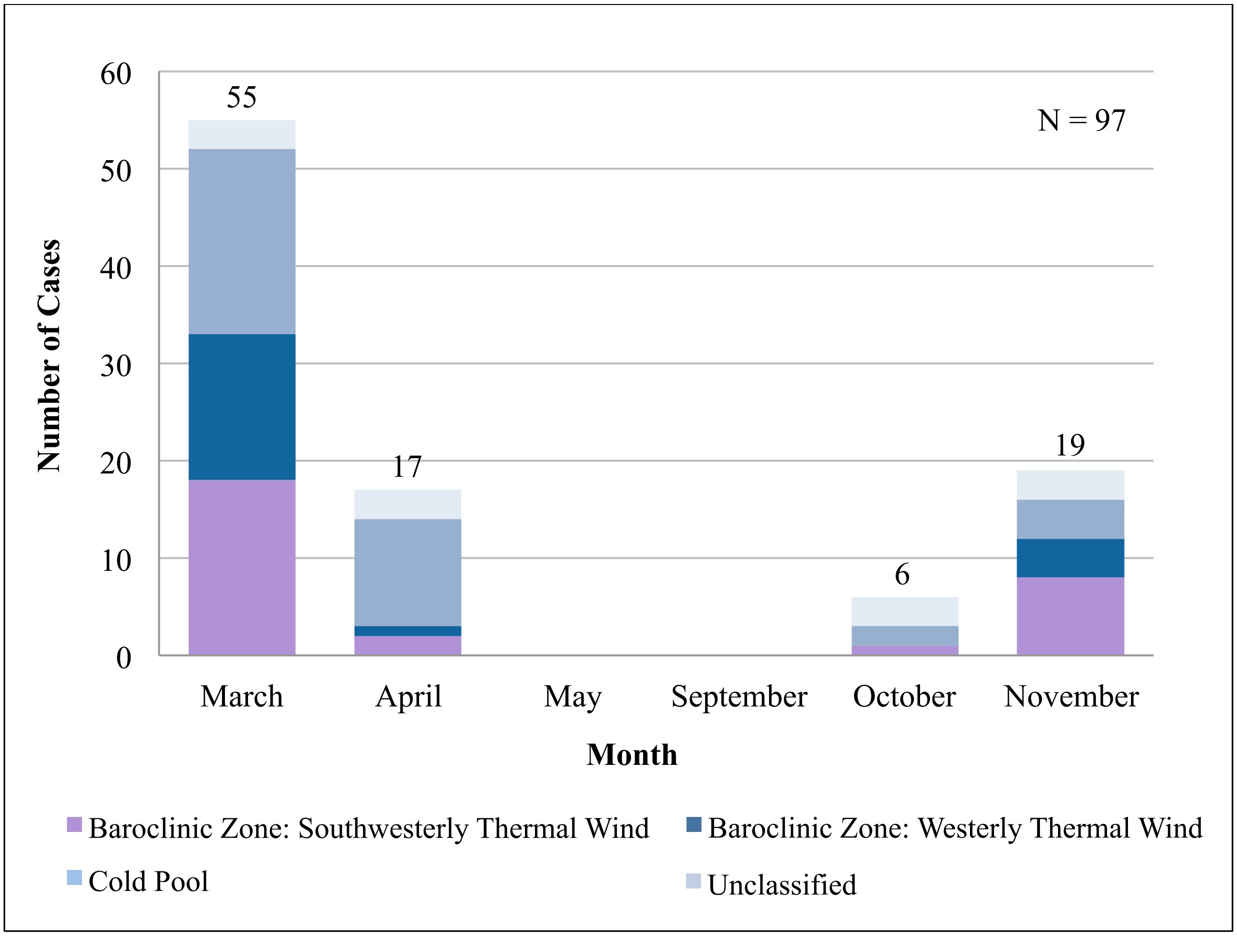

Fig. 3.5 Monthly distribution of major transition season Northeast snowstorms according to lower-tropospheric cold air pattern.

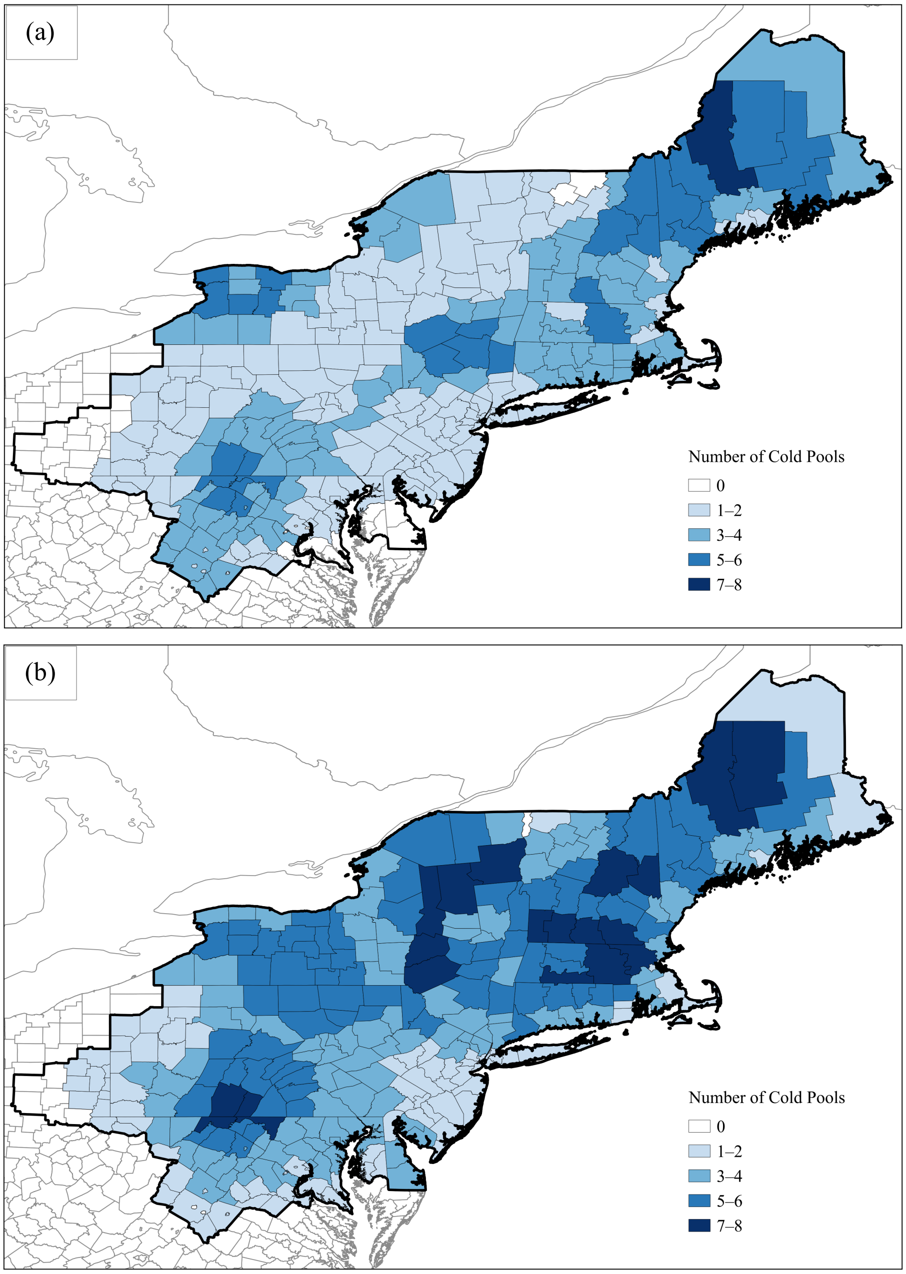

Fig. 3.6 The number of cold pools in each county at (a) the initial time and (b) the midpoint time of the cold pool for the cases in the Cold Pool category.

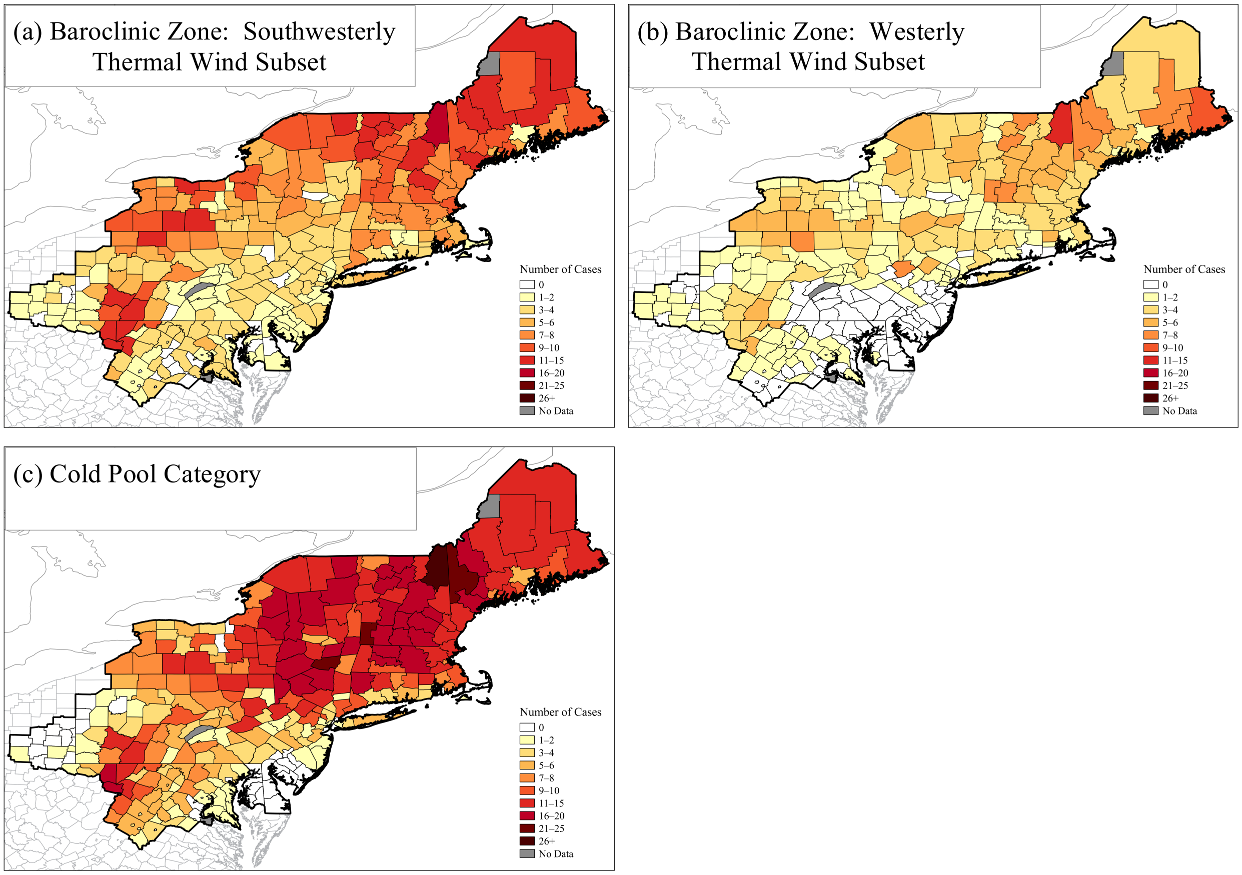

Fig. 3.7 Number of cases in each county (shaded) where GHCN-D snowfall accumulation values for a case met or exceeded the 12-h heavy snow warning criterion threshold for the respective CWA of each county for the (a) Baroclinic Zone: Southwesterly Thermal Wind subset, (b) Baroclinic Zone: Westerly Thermal Wind subset, and (c) Cold Pool category.

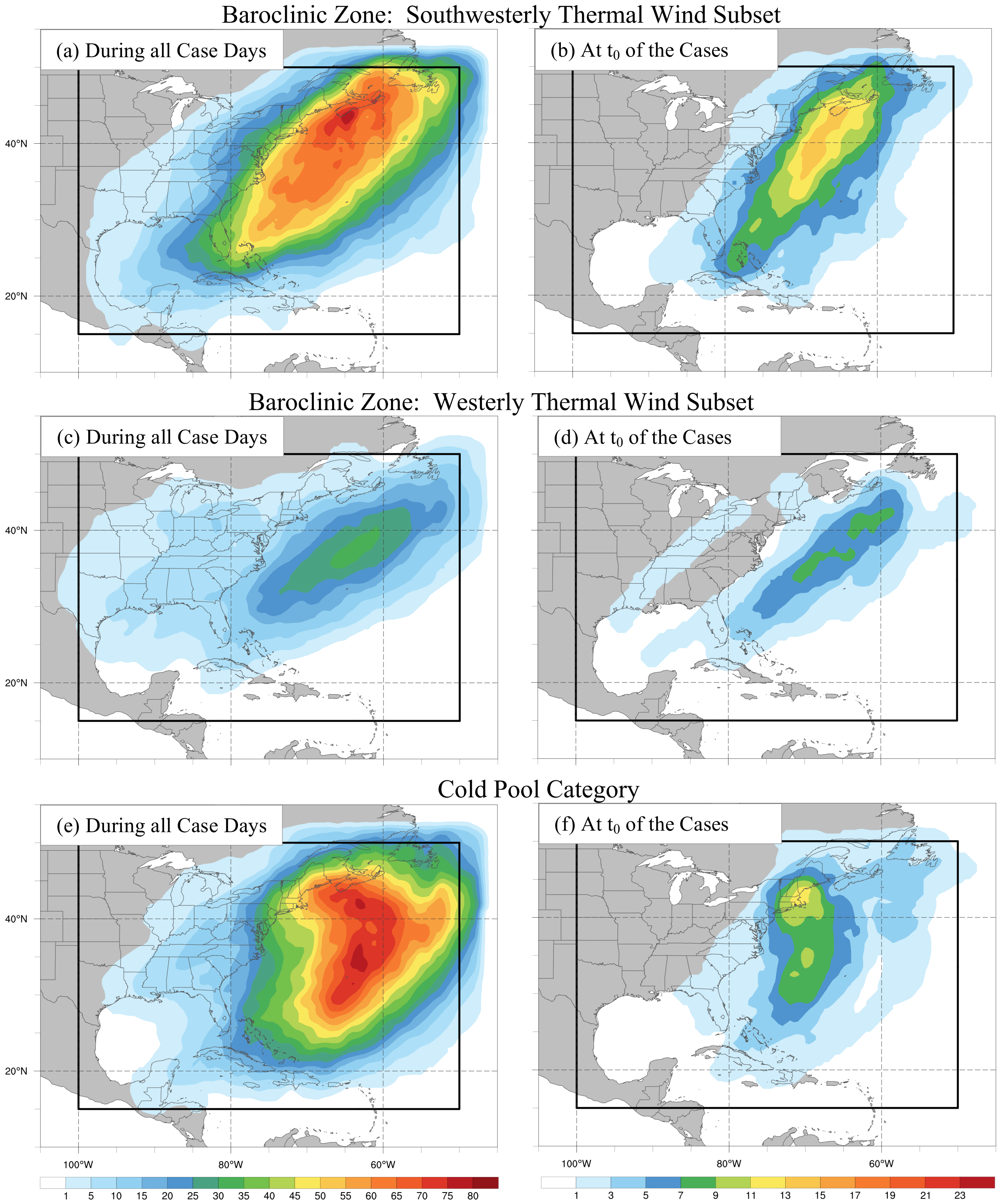

Fig. 3.8 AR axis density (shaded; number of unique ARs in a 250 km radius) within the domain bounded by the black box (left) during all case days and (right) at the composite center time (t_0) of the cases for (a),(b) the Baroclinic Zone: Southwesterly Thermal Wind subset, (c),(d) the Baroclinic Zone: Westerly Thermal Wind subset, and (e),(f) the Cold Pool category.

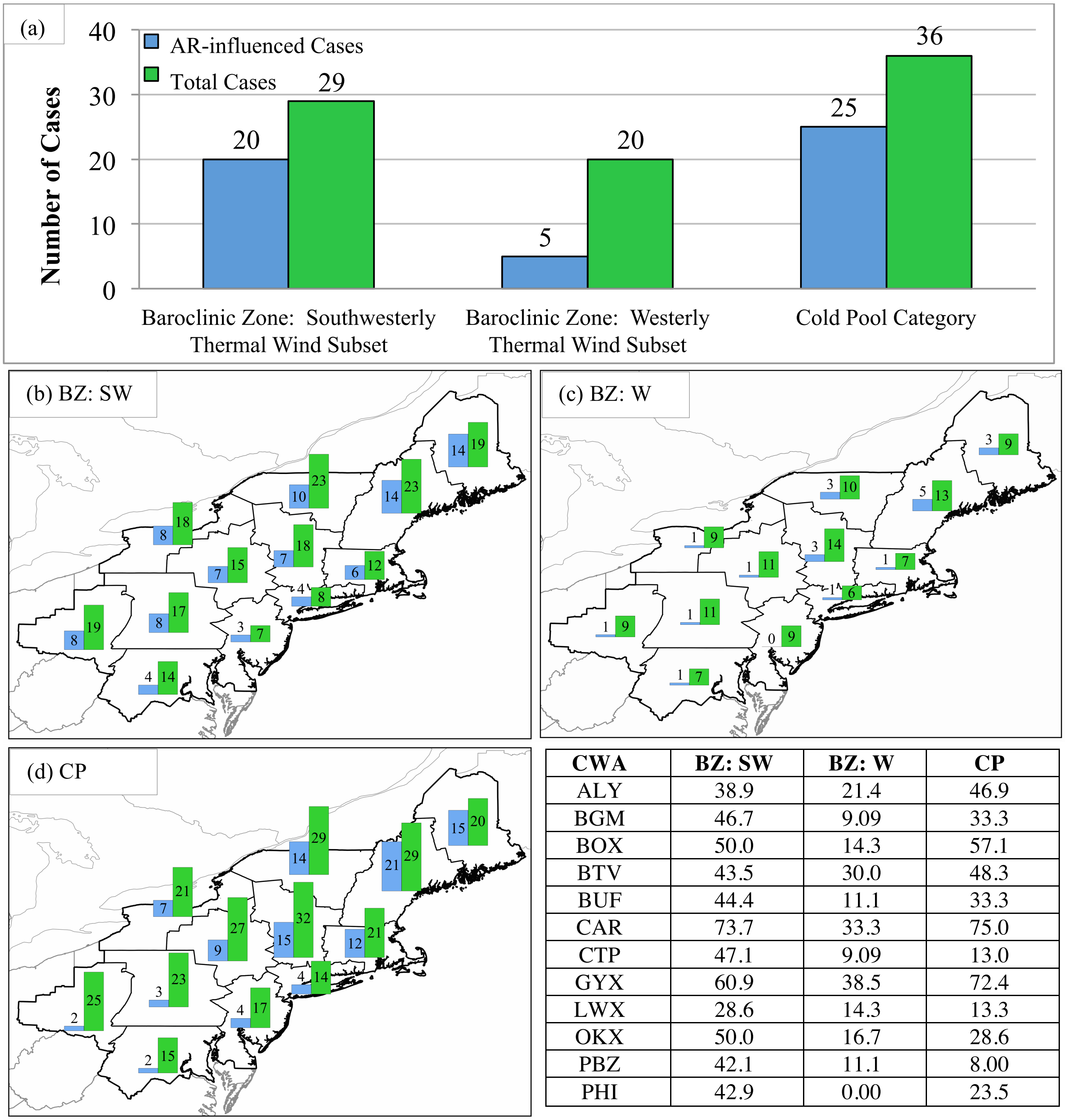

CWA	BZ: SW	BZ: W	CP
ALY	38.9	21.4	46.9
BGM	46.7	9.09	33.3
BOX	50.0	14.3	57.1
BTV	43.5	30.0	48.3
BUF	44.4	11.1	33.3
CAR	73.7	33.3	75.0
CTP	47.1	9.09	13.0
GYX	60.9	38.5	72.4
LWX	28.6	14.3	13.3
OKX	50.0	16.7	28.6
PBZ	42.1	11.1	8.00
PHI	42.9	0.00	23.5

Fig. 3.9 (a) The number of cases experiencing an association between at least one point of heavy snowfall and an AR (blue) compared with the total number of cases (green). The number of cases in a CWA where at least one point of snowfall accumulation for a case met or exceeded the 12-h heavy snow warning criterion for its respective CWA (green; hereafter total cases with heavy snowfall) and the total number of cases where the aforementioned statement holds true and at least one of those points is associated with an AR (blue; hereafter AR-influenced cases) for (b) the Baroclinic Zone: Southwesterly Thermal Wind Subset (BZ: SW), (c) the Baroclinic Zone: Westerly Thermal Wind Subset (BZ: W), and (d) the Cold Pool Category (CP). The embedded table (bottom right) displays the association fraction (%) for each CWA for each lower-tropospheric cold air pattern, calculated by dividing the number of AR-influenced cases by total cases with heavy snowfall in a CWA. The CWA abbreviations in the table are as in Fig. 2.2.

Month	**Case Periods with an AR**	**Total Case Periods**	**AR Fraction (%)**
March	341	600	56.8
April	126	184	68.5
October	44	62	71.0
November	112	190	58.9

Table 3.1 AR Fraction (%) and the components used to calculate the AR fraction for each month.

Lower-Tropospheric Cold Air Pattern	**Time**	**Case Periods with an AR**	**Total Case Periods**	**AR Fraction (%)**
Baroclinic Zone: Southwesterly Thermal Wind Subset	During all Case Days	211	296	71.3
	At t_0	24	29	82.8
Baroclinic Zone: Westerly Thermal Wind Subset	During all Case Days	87	183	47.5
	At t_0	13	20	65.0
Cold Pool Category	During all Case Days	248	420	59.0
	At t_0	19	36	52.8

Table 3.2 AR Fraction (%) and the components used to calculate the AR fraction for each lower-tropospheric cold air pattern during all case days and at t_0.

Lower-Tropospheric Cold Air Pattern	**Case Periods with an AR**	**Total Case Periods**	**Landfalling AR Fraction (%)**
Baroclinic Zone: Southwesterly Thermal Wind Subset	5	29	17.2
Baroclinic Zone: Westerly Thermal Wind Subset	2	20	10.0
Cold Pool Category	11	36	30.6

Table 3.3 Landfalling AR Fraction (%) at t_0 and the components used to calculate the landfalling AR fraction for each lower-tropospheric cold air pattern.

4. Composite Analyses

The composite analysis of each lower-tropospheric cold air pattern begins with an analysis of the planetary-to-synoptic scale flow patterns from t_0 – 48 h to t_0 + 24 h in 24 h intervals. The analysis of the planetary-to-synoptic scale flow patterns will be followed by an analysis of the synoptic-to-mesoscale flow patterns at t_0 for both subsets of the Baroclinic Zone category and at t_0 – 6 h and t_0 for the Cold Pool category. The Cold Pool category includes an additional time, t_0 – 6 h, to discuss the temporal evolution of a lower-tropospheric cold pool in the composites. For the Cold Pool category only, an additional analysis is included that utilizes composite soundings to assess cold pool formation and maintenance in various thermodynamic environments.

As the composites used in the various analyses are shifted in space (see section 2.5), geographical terms throughout this chapter are used solely for referencing the atmospheric flow patterns in the figures. For the analysis of the synoptic-to-mesoscale flow patterns, the figures depicting cross sections for each subset of the Baroclinic Zone category were created by: 1) identifying the location of the 925–850-hPa frontogenesis maximum associated with the composite surface cyclone at t_0, and 2) creating a cross section normal to the 925–850-hPa layer-mean temperature gradient at t_0 that transects the location of the frontogenesis maximum. The figures depicting cross sections for the Cold Pool category were constructed by creating a cross section normal to the 925–850-hPa layer-mean temperature gradient at t_0 that transects the composite center location. All of the cross sections for each lower-tropospheric cold air pattern have a length of approximately 2000 km.

4.1 Baroclinic Zone: Southwesterly Thermal Wind Subset

4.1.1 Planetary-to-Synoptic Scale Flow Patterns

Figures 4.1 and 4.2 depict the planetary-to-synoptic scale flow patterns in the middle and upper troposphere from t_0 – 48 h to t_0 + 24 h. At t_0 – 48 h, the middle troposphere is characterized by several prominent features manifested in the 500-hPa geopotential height field (Fig. 4.1a). The prominent features include: 1) a well-established ridge over western North America (R1), 2) a deep trough over eastern Canada (T1), and 3) a positively tilted trough over the central U.S. (T2). Downstream of R1 and upstream of T1 at t_0 – 48 h (Fig. 4.1a), a surface anticyclone (H1) is evident (Fig. 4.2a). H1 is also evident beneath an upper-level confluent region over western Canada (Fig. 4.1a). Downstream of T2 at t_0 – 48 h (Fig. 4.1a), an inverted trough (L1) is evident as the incipient form of a composite surface cyclone (C1) that becomes prominent at t_0 – 24 h and affects the Northeast at t_0 (Figs. 4.2a,c,e).

As time progresses from t_0 – 48 h to t_0, T1 remains relatively stationary and phases with T2 by t_0 (Figs. 4.1a,c,e). Also as time progresses from t_0 – 48 h to t_0, T2 moves east while phasing with T1, gaining a neutral tilt and amplifying (Figs. 4.1a,c,e). While T2 amplifies, R1 deamplifies (Figs. 4.1a,c,e), suggestive of downstream development. Downstream of T2 as it moves east from t_0 – 24 h to t_0 + 24 h (Figs. 4.1c,e,g), C1 is apparent (Figs. 4.2c,e,g). Also downstream of T2, forcing for ascent is manifested by the convergence of Q-vectors over L1 at t_0 – 48 h (Figs. 4.1b and 4.2a) and over C1 from t_0 – 24 h to t_0 + 24 h (Figs. 4.1d,f,h and 4.2c,e,g).

At t_0 – 48 h toward the base of T1 (Fig. 4.1a), the upper troposphere features a 40–45 m s^{-1} jet streak embedded in the flow at 250 hPa over the eastern Canada/U.S. border (Fig. 4.2a). The jet streak at 250 hPa persists over the eastern Canada/U.S. border through t_0 (Figs. 4.2a,c,e).

During t_0 – 24 h through t_0, the equatorward entrance region of the 250-hPa jet streak provides favorable conditions for ascent over C1 (Figs. 4.2c,e). Although not apparent at t_0 – 24 h or t_0, evidence of dynamical coupling between the aforementioned 250-hPa jet streak and a second 250-hPa jet streak over the northern Gulf of Mexico and the Gulf Coast occurs at t_0 – 18 h and t_0 – 12 h over C1 (not shown). This dynamical coupling likely enhances ascent over C1.

Figure 4.2 also depicts the planetary-to-synoptic scale flow patterns in the lower troposphere from t_0 – 48 h to t_0 + 24 h. At t_0 – 48 h, the lower troposphere is characterized by several prominent systems manifested in the MSLP field that include: 1) H1, 2) a surface cyclone over the western North Atlantic Ocean (L2), and 3) L1 (Fig. 4.2a). From t_0 – 48 h to t_0 – 24 h, the circulation established by H1 and L2 advects cold air toward the northeast U.S. (inferred from the 1000–500-hPa thickness and MSLP fields in Figs. 4.2a,c). In the region of cold air advection and at 850 hPa, temperatures are anomalously low (Figs. 4.2b,d). Also at 850 hPa, temperatures below freezing are established in the area where heavy snowfall occurs at t_0 (i.e., northwest of the composite center) (Figs. 4.2b,d).

From t_0 – 48 h to t_0 – 24 h, L1, the incipient form of C1, expands north, and by t_0 – 24 h, C1 is evident over the Southeast within the expanded L1 (Figs. 4.2a,c). Also from t_0 – 48 h to t_0 – 24 h, H1 moves southeast. While moving southeast, H1 has a ridge of high pressure that extends east such that the ridge is located north of L1 at t_0 – 48 h and C1 at t_0 – 24 h. (Figs. 4.2a,c). From t_0 – 24 h to t_0, C1 intensifies and moves northeast (Figs. 4.2c,e). During the same time period, H1 continues to move southeast while retaining a ridge of high pressure to the north of C1 (Figs. 4.2c,e). Kocin and Uccellini (2004b, pp. 59–77) noted that the configuration of H1 and its position to the northwest of C1 results in cold air being advected south primarily over land, which allows for the air to remain cold by avoiding sensible heat fluxes from the ocean. A closed circulation at 850 hPa that develops by t_0 also aids in advecting cold air south through t_0 + 24 h (Figs. 4.2f,h). To the west of this closed circulation, temperature anomalies are 1.5–2.0 σ below normal.

Figure 4.3 displays the planetary-to-synoptic scale flow patterns focusing on moisture from t_0 – 48 h to t_0 + 24 h. At t_0 – 48 h, a broad area of precipitable water (PWAT) featuring values of 15–30 mm stretches from the southeast U.S. into the western North Atlantic Ocean and coincides with a corridor of IVT featuring values of 100–300 kg m^{-1} s^{-1} (Fig. 4.3a,b). This corridor of IVT (Fig. 4.3b) is evident along a cold front associated with a surface pressure trough extending southwest from L2 (Fig. 4.2a). During t_0 – 24 h through t_0 + 24 h, low-level flow, established by the juxtaposition of the composite surface cyclone and a surface anticyclone centered over the Atlantic Ocean, reinforces the prior-established PWAT and IVT by advecting moisture polewards (Figs. 4.3c–h). A northeastward advancing PWAT plume reflects this poleward moisture advection (Figs. 4.3c,e,g). Strong winds (25–30 m s^{-1}) at 850 hPa in the southeastern sector of the composite surface cyclone at t_0, indicative of a LLJ, aid in advecting the PWAT plume toward the northeast (Fig. 4.3e). At t_0, PWAT anomalies associated with the PWAT plume reach between 2.0 σ and 2.5 σ above normal (Fig. 4.3e).

At t_0, the PWAT plume (Fig. 4.3e) coincides with a region of large IVT that has a maximum value exceeding 700 kg m^{-1} s^{-1} (Fig. 4.3f). In this region of large IVT, an AR axis is objectively identified from the composite IVT field. The AR axis objectively identified from the composite IVT field stretches from the southwest to the northeast. IVT vectors surrounding the AR axis indicate moisture transport to the northeast along the AR axis, especially north of 40°N (Fig. 4.3f). The northeast moisture transport along the AR axis at t_0 (Fig. 4.3f) is directed into an area of ascent in the northeastern sector of the composite surface cyclone (Fig. 4.1e). An AR axis continues to be objectively identified from the composite IVT field through t_0 + 24 h (Figs. 4.3f,h) as the composite surface cyclone moves northeast while weakening (Figs. 4.3f,h).

4.1.2 Synoptic-to-Mesoscale Flow Patterns

Figure 4.4 displays the synoptic-to-mesoscale flow patterns with a focus on the lower troposphere, represented by the 1000–850-hPa layer, at t_0. At t_0, the 1000–850-hPa thickness field features a large thickness gradient from north of the composite surface cyclone center, where thickness values are 130.5–131.0 dam, to southeastern Canada, where thickness values are 120.5–121.0 dam (Fig. 4.4a). Also at t_0, 1000–850-hPa thickness values that are supportive of snowfall (i.e., thickness values ≤ 129.0 dam) are located in the northwest sector of the composite surface cyclone. Consistently, in the northwest sector of the composite surface cyclone, the 1000–850-hPa layer-mean temperature field reveals cold lower-tropospheric air with mean temperatures below freezing (Fig. 4.4b). The cold lower-tropospheric air is maintained in the northwest sector of the composite surface cyclone by horizontal cold air advection and cooling due to ascent (Fig. 4.4b).

The synoptic-to-mesoscale flow patterns with a focus on frontogenesis and its attendant ageostrophic circulation are displayed at t_0 in Fig. 4.5. At t_0, a band of frontogenesis stretches from the southwest to the northeast and resides to the northwest of the composite surface cyclone center (Fig. 4.5a). A cross section through the band of frontogenesis reveals deep frontogenesis, with the largest magnitudes of frontogenesis concentrated below 850 hPa (Fig. 4.5b). The cross section through the band of frontogenesis also reveals a deep thermally direct ageostrophic circulation. The thermally direct ageostrophic circulation aids in providing the necessary ingredients for snowfall. Specifically, the lower-level branch of the ageostropic circulation advects cold air to the southeast, which acts to maintain lower-tropospheric cold air to the northwest of the cross section center (Figs. 4.5b and 4.6b). The ascending branch of the ageostrophic circulation provides lift in an area of high relative humidity values, which creates conditions conducive for precipitation generation (Fig. 4.6a). Conditions are also conducive for heavy snow as suggested by the presence of the cross-hair signature (Cobb and Waldstreicher 2005) to the northwest of the cross-section center. The cross-hair signature is evident where the core of strongest upward vertical velocity to the northwest of the cross-section center overlaps with high relative humidity values and coincides with the DGZ (Fig. 4.6a). Where the cross-hair signature is evident, temperature are below freezing throughout the depth of the cross section (Figs. 4.6a,b), supporting snowfall. At t_0, the occurrence of heavy wet snow is plausible near the cross section center as a notable portion of the core of the ascending branch is located below the DGZ (Fig. 4.6a). This alignment allows for the production of supercooled water droplets that can enhance riming and lead to high-density snow (Cobb and Waldstreicher 2005).

4.2 Baroclinic Zone: Westerly Thermal Wind Subset

4.2.1 Planetary-to-Synoptic Scale Flow Patterns

Figures 4.7 and 4.8 display the planetary-to-synoptic scale flow patterns in the middle and upper troposphere from t_0 – 48 h to t_0 + 24 h for the Baroclinic Zone: Westerly Thermal Wind subset. The middle troposphere at t_0 – 48 h is characterized by several features evident in the 500-hPa geopotential height field that include: 1) a deep trough over eastern Canada (T3), 2) a low-amplitude, positively tilted trough over the central U.S. (T4), and 3) a low-amplitude ridge over western North America (R2) (Fig. 4.7a). Upstream of T3 at t_0 – 48 h (Fig. 4.7a), a surface anticyclone (H2) is evident over central Canada (Fig. 4.8a) and beneath weak confluent flow at 500 hPa (Fig. 4.7a). As time progresses from t_0 – 48 h to t_0 + 24 h, T3 remains relatively stationary over eastern Canada while deamplifying (Figs. 4.7a,c,e,g). At t_0 – 48 h and downstream of T4 (Fig. 4.7a), a composite surface cyclone (C2) is established over the central U.S. (Fig. 4.8a). From t_0 – 48 h to t_0, T4 moves east while amplifying and gaining a neutral tilt (Figs. 4.7a,c,e). Downstream of the eastward moving T4, Q-vector forcing for ascent is evident (Figs. 4.7b,d,f,h) over C2 (Figs. 4.8a,c,e,g). At t_0, magnitudes of Q-vector forcing for ascent are especially large within and to the northwest of the center of C2 (Figs. 4.7f and 4.8e). At t_0 – 48 h, the upper troposphere features a 40–45 m s^{-1} jet streak embedded in the flow at 250 hPa (Fig. 4.8a). During t_0 – 48 h through t_0, the 250-hPa jet streak shifts east (Figs. 4.8a,c,e), and to its southwest at t_0, a second jet streak has formed at 250 hPa (Fig. 4.8e). At t_0, the two jet streaks are in a configuration favorable for dynamical coupling over C2 (Fig. 4.8e), enhancing ascent over C2.

Figure 4.8 also displays the planetary-to-synoptic scale flow patterns in the lower troposphere from t_0 – 48 h to t_0 + 24 h. At t_0 – 48 h, several notable systems evident in the MSLP field characterize the lower troposphere. These systems include: 1) H2, 2) C2, and 3) a surface cyclone over the western North Atlantic Ocean (L3) (Fig. 4.8a). At t_0 – 48 h, H2 is located to the northeast of C2 (Fig. 4.8a). H2 remains to the northeast of C2 as the two systems progress eastward during t_0 – 48 h through t_0 – 24 h (Figs. 4.8a,c). Also during t_0 – 48 h through t_0 – 24 h, the flow established by H2 and L3 advects cold air toward the south (inferred from the 1000–500-hPa thickness and MSLP fields in Figs. 4.8a,c), reinforcing cold air in the Northeast. At 850 hPa, in the area of cold air advection, temperatures are anomalously low (Figs. 4.8b,d). The anomalously low temperatures infiltrate the mid-Atlantic states at t_0 as a closed circulation at 850 hPa that develops by t_0 advects cold air toward the south (Fig. 4.8f). These anomalously low temperatures persist in the mid-Atlantic states through t_0 + 24 h (Figs. 4.8f,h).

Figure 4.9 shows the planetary-to-synoptic scale flow patterns with a focus on moisture from t_0 – 48 h to t_0 + 24 h. At t_0 – 48 h, PWAT values of approximately 15–30 mm are collocated with a corridor of IVT values of approximately 100–300 kg m^{-1} s^{-1} (Figs. 4.9a,b). This corridor of IVT (Fig. 4.9b) is evident along a cold front associated with L3, located within a surface pressure trough extending southwest from L3 (Fig. 4.8a). During t_0 – 24 h through t_0, low-level flow, which is associated with the composite surface cyclone and enhanced by a surface anticyclone over the western North Atlantic Ocean, reinforces the established PWAT and IVT values by advecting moisture poleward (Figs. 4.9c–f). This advection of moisture is reflected in a PWAT plume that advances poleward from t_0 – 24 h through t_0 + 24 h (Figs. 4.9c,e,g). Southwesterly flow at 850 hPa associated with the composite surface cyclone aids in advecting the PWAT plume poleward from t_0 – 48 h to t_0 + 24 h (Figs. 4.9a,c,e,g). The southwesterly flow at 850 hPa associated with the composite surface cyclone increases from t_0 – 48 h to t_0, such that wind speeds reach 25–30 m s^{-1} in the southeastern sector of the composite cyclone, indicating the presence of a LLJ (Figs. 4.9a,c,e). As the PWAT plume is advected poleward, PWAT anomalies coincident with the PWAT plume increase from between 0.5 σ and 1.0 σ above normal at t_0 – 24 h (Fig. 4.9c) to between 1.5 σ and 2.0 σ above normal at t_0 (Fig. 4.9e).

At t_0, the PWAT plume is collocated with IVT values that exceed 700 kg m^{-1} s^{-1} and an objectively identified AR axis (Figs. 4.9e,f), which was identified from the composite IVT field. The AR axis objectively identified from the composite IVT field stretches from the southwest to the northeast (Fig. 4.9f). IVT vectors surrounding the AR axis at t_0 indicate moisture transport with a prominent eastward component, especially south of 40°N (Fig. 4.9f). North of 40°N, IVT vectors indicate northeastward moisture transport along the AR axis (Fig. 4.9f) directed into a region of ascent in the northeastern sector of C2 (Figs. 4.7e and 4.8e). An AR axis continues to be objectively identified from the composite IVT field until t_0 + 18 h (not shown) as the composite surface cyclone moves northeast while weakening (Figs. 4.9f,h).

4.2.2 Synoptic-to-Mesoscale Flow Patterns

Figure 4.10 displays the synoptic-to-mesoscale flow patterns with a focus on the lower troposphere, represented by the 1000–850-hPa layer, at t_0. At t_0, the 1000–850-hPa thickness field features a large thickness gradient from north of the composite surface cyclone center, where thickness values are 130.5–131.0 dam, to southeastern Canada, where thickness values are 121.0–121.5 dam (Fig. 4.10a). Thickness values below 129.0 dam, which are supportive of snowfall, are evident in the northwest sector of the composite surface cyclone (Fig. 4.10a), and correspondingly in the same sector, the 1000–850-hPa layer-mean temperature field exhibits lower-tropospheric air with temperatures below freezing (Fig. 4.10b). The cold lower-tropospheric air in the northwest sector of the composite surface cyclone is maintained by horizontal cold air advection and cooling due to ascent (Fig. 4.10b).

Figures 4.11–4.12 illustrate the synoptic-to-mesoscale flow patterns focusing on frontogenesis and its attendant ageostrophic circulation at t_0. At t_0, a band of frontogenesis with a zonal orientation is located to the north of the composite surface cyclone center (Fig. 4.11a). A cross section through the band of frontogenesis reveals a region of frontogenesis that extends from 1000 hPa to 450 hPa with the largest magnitudes of frontogenesis focused below 850 hPa

(Fig. 4.11b). The cross section also reveals a deep thermally direct ageostrophic circulation (Fig. 4.11b). The ageostrophic circulation aids in providing the necessary ingredients for snowfall. Specifically, the lower-level branch of the ageostrophic circulation advects cold air to the south (Figs. 4.11b and 4.12b), reinforcing lower-tropospheric cold air. The ascending branch of the ageostrophic circulation provides ascent in a region of high relative humidity values (Fig. 4.12a), creating conditions favorable for precipitation production. Conditions are also favorable for heavy snow, as indicated by the presence of the cross-hair signature (Cobb and Waldstreicher 2005) to the north of the cross-section center. The cross-hair signature is evident where the core of maximum ascent coincides with high relative humidity values and intersects the DGZ (Fig. 4.12a). Also to the north of the cross-section center, temperatures are below freezing (Fig. 4.12b), supporting a precipitation type of snow.

4.3 Cold Pool Category

4.3.1. Planetary-to-Synoptic Scale Flow Patterns

Figures 4.13 and 4.14 display the planetary-to-synoptic scale flow patterns in the middle and upper troposphere for the Cold Pool category. At t_0 – 48 h, the middle troposphere is characterized by several prominent features manifested in the 500-hPa geopotential height field (Fig. 4.13a). The prominent features include: 1) a trough over eastern Canada (T5), 2) a trough over the central U.S. with a positive tilt (T6), and 3) a ridge over western North America (R3) (Fig. 4.13a). At t_0 – 48 h, a surface anticyclone (H3) (Fig. 4.14a) exists downstream of R3 and upstream of T5 (Fig. 4.13a).

As time progresses from t_0 – 48 h to t_0, T5 deamplifies and moves east; meanwhile, T6 amplifies and moves east (Figs. 4.13a,c,e). Downstream of T6 at t_0 – 24 h (Fig. 4.13c), a broad area of low surface pressure (L5) is evident (Fig. 4.14c) and is the incipient form of a composite surface cyclone (C3), which becomes prominent at t_0 (Fig. 4.14e). From t_0 to t_0 + 24 h, T6 continues to amplify (Figs. 4.13e,g). Downstream of T6, ridging is evident at 500 hPa (Figs. 4.13e,g), likely due to latent heat release from C3, which is located downstream of T6 (Figs. 4.14e,g). Downstream of T6 during t_0 – 24 h through t_0 + 24 h, Q-vector forcing for ascent overlaps with L5 at t_0 – 24 h (Figs. 4.13d and 4.14c) and with C3 at t_0 and t_0 + 24 h (Figs. 4.13f,h and 4.14e,g). At t_0, large values of Q-vector forcing for ascent are concentrated over the composite center location (Fig. 4.13f), corresponding to the location of a lower-tropospheric cold pool (Fig. 4.16c).

At t_0 – 48 h, the upper troposphere features a 40–45 m s^{-1} jet streak at 250 hPa (J1) over the eastern U.S. (Fig. 4.14a). By t_0 – 24 h, a second 40–45 m s^{-1} jet streak (J2) develops at 250 hPa (Fig. 4.14c). The two jet streaks are oriented to promote jet coupling over L5 (Fig. 4.14c), likely enhancing ascent over L5, the incipient form of C3. During t_0 through t_0 + 24 h, J2 becomes the prominent jet streak and provides favorable conditions for ascent over C3, as C3 is located in the poleward exit region of J2 (Figs. 4.14e,g).

Figure 4.14 also displays the planetary-to-synoptic scale flow patterns in the lower troposphere. The lower troposphere is characterized by several prominent systems in the MSLP field at t_0 – 48 h (Fig. 4.14a). The prominent systems include: 1) H3 and 2) a surface cyclone over the western North Atlantic Ocean (L4) (Fig. 4.14a). At t_0 – 48 h, the circulation established by H3 and L4 advects cold air to the south (inferred from the 1000–500-hPa thickness and MSLP fields) toward the northeast U.S. (Fig. 4.14a). Also at t_0 – 48 h, a large area of anomalous cold air is absent at 850 hPa in the region of cold air advection (Fig. 4.14b). At t_0 – 24 h, L5, the incipient form of C3, is evident over the southeast U.S., and by t_0, C3 develops within L5 (Figs. 4.14c,e). H3, which has moved east since t_0 – 48 h, is located to the north of L5 at t_0 – 24 h and to the north of C3 at t_0 (Figs. 4.14a,c,e). From t_0 to t_0 + 24 h, both C3 and H3 shift poleward while C3 strengthens and H3 weakens (Figs. 4.14e,g).

From t_0 – 24 h to t_0, temperatures at 850 hPa in the area of heavy snowfall (i.e., the composite center location) decrease and become 0.5–1.0 σ below normal (Figs. 4.14d,f). The anomalously low temperatures in the area of heavy snowfall coincide with a southward protrusion of cold air with temperatures between −5ºC and −10ºC (Fig. 4.14f). This southward protrusion of cold air is located to the north of the center of a closed circulation that develops at 850 hPa by t_0 (Fig. 4.14f). The southward protrusion of cold air develops despite the presence of warm air advection at 850 hPa along the eastern boundary of the southward protrusion (Fig. 4.14f). At t_0 + 24 h, the southward protrusion of cold air is no longer prominent in the area of heavy snowfall (Fig. 4.14h) and is suggested to have been eroded by warm air advection at 850 hPa that occurred from t_0 (Fig 4.14f) to t_0 + 12h (not shown).

Figure 4.15 displays the planetary-to-synoptic flow patterns with a focus on moisture. From t_0 – 48 h to t_0 – 24 h, PWAT values of approximately 15–30 mm are collocated with a corridor of IVT values of approximately 100–300 kg m^{-1} s^{-1} (Figs. 4.15a–d). The IVT corridor stretches from the southeast U.S. into the North Atlantic Ocean (Figs. 4.15b,d) along a cold front located within a surface pressure trough extending southwest from L4 (Figs. 4.14a,c). Southwesterly flow at 850 hPa associated with the composite surface cyclone aids in reinforcing the prior established IVT and PWAT values by advecting a broad plume of PWAT toward the northeast during t_0 through t_0 + 24 h (Figs. 4.15e,g). While advancing toward the northeast, the broad plume of PWAT maintains PWAT anomalies between 0.5 σ and 1.0 σ above normal (Figs. 4.15e,g). Also during t_0 through t_0 + 24 h, IVT vectors transition in space from indicating northeastward moisture transport towards the south/southeast of the composite surface cyclone center to indicating northwestward moisture transport towards the north/north-northeast of the composite surface cyclone center (Figs. 4.15f,h). At t_0 + 24 h, the broad plume of PWAT coincides with an objectively identified AR axis, identified from the composite IVT field (Fig. 4.15h). The moisture transport along the AR axis (Fig. 4.15h) is directed into an area of ascent (Fig. 4.13g) in the eastern portion of the composite surface cyclone (Fig. 4.14g).

4.3.2. Synoptic-to-Mesoscale Flow Patterns

Figure 4.16 displays the synoptic-to-mesoscale flow patterns with a focus on the lower troposphere, represented by the 1000–850-hPa layer at t_0 – 6 h and $t_{0.}$ At t_0 – 6 h, baroclinicity characterized by a moderate thickness gradient is present from north of the composite surface cyclone center to southeastern Canada (Fig. 4.16a). Also at t_0 – 6 h, a southward protrusion of low 1000–850-hPa thicknesses is located to the north of the composite surface cyclone center (Fig. 4.16a). In the area of the southward protrusion of low 1000–850-hPa thicknesses, a cold pool forms at t_0 as an enclosed 1000–850-hPa thickness minimum (Figs. 4.16a,c).

At both t_0 – 6 h and t_0, weak horizontal cold air advection is evident immediately to the west of the composite center location (Figs. 4.16b,d). The weak horizontal cold air advection is attributable to the cold air in either the southward protrusion of cold air or the cold pool being advected toward the west by easterly winds. As cold air is not horizontally advected into the southward protrusion of cold air or the cold pool, it is suggested that horizontal cold air advection is not the key process in the formation of the cold pool. Cooling due to ascent occurs immediately to the east of the composite center location within a portion of the southward protrusion of cold air at t_0 – 6 h or within the cold pool at t_0 (Figs. 4.16b,d). As cooling occurs within a portion of the southward protrusion of cold air or within the cold pool, it is suggested that cooling due to ascent is a partial contributor to the formation of the cold pool due to its limited areal influence.

Figures 4.17–4.18 display the synoptic-to-mesoscale flow patterns with a focus on frontogenesis and cold pool formation. At t_0 – 6 h, a region of frontogenesis is in close proximity to the southward protrusion of cold air, evident in the 925–850-hPa layer-mean potential temperature field (Fig. 4.17a). This region of frontogenesis is located to the north of the composite surface cyclone. Within this region of frontogenesis and close to the center of the composite surface cyclone, a band of locally higher values of frontogenesis stretches from the west to the east. From t_0 – 6 h to t_0, both the region of frontogenesis and the band of frontogenesis move slightly north with the composite surface cyclone, and the band of frontogenesis attains a southwest-to-northeast orientation (Figs. 4.17a,c). At t_0, the band of frontogenesis is located to the southeast of the cold pool, the latter evident in the 925–850-hPa layer-mean potential temperature field, and the region of frontogenesis overlaps with the southeastern boundary of the cold pool (Fig. 4.17c).

At t_0 – 6 h, a cross section through the Cold Pool category composite center location and the region of frontogenesis reveals evidence of the cold pool that develops at t_0 in the form of a dome of cold air represented by a bowing 275 K isentrope below 850 hPa at the cross-section center (Fig. 4.17b). At t_0, a cross section displays the cold pool as a local minimum of potential temperature below 850 hPa at the cross-section center (Fig. 4.17d). At t_0 – 6 h and t_0, the cross sections reveal shallow frontogenesis to the southeast of the cross-section center that slopes over the dome of cold air or the cold pool. The cross sections also reveal a weak horizontal potential temperature gradient below 850 hPa and a weak lower-level branch of the ageostrophic circulation northwest of the cross-section center (Figs. 4.17b,d), indicating weak cold air advection by the ageostrophic wind.

At t_0 – 6 h over the dome of cold air at the cross-section center (Fig. 4.17b), an ascent maximum coincides with high values of relative humidity and intersects the DGZ (Fig. 4.18a), characteristic of the cross-hair signature, which indicates conditions conducive to heavy snow (Cobb and Waldstreicher 2005). The cross-hair signature persists over the cross-section center at t_0 (Fig. 4.18c). Beneath the cross-hair signature, lower-level cooling occurs below 800 hPa (Figs. 4.18b,d), and temperatures at 1000 hPa decrease from above freezing at t_0 – 6 h (Fig. 4.18b) to below freezing at t_0 (Fig. 4.18d). The lower-level cooling is likely attributable to diabatic cooling from sublimating snow as the environment below 800 hPa moistened, which is indicated by relative humidity values increasing from 80–90% at t_0 – 6 h to 90–100% at t_0 (Figs. 4.18a,c).

4.3.3 Soundings

4.3.3.1 Changeover Subset

At t_0 – 12 h, the sounding for the changeover subset (Fig. 4.19a) generally characterizes an environment with precipitation in the form of light rain; at t_0 – 12 h or within ±3 h of this time, light rain was occurring in more than half of the cases (4 of 7 cases). The sounding at t_0 – 12 h reveals unsaturated air below 600 hPa and a temperature profile below freezing with the exception of the 1000–925-hPa layer (hereafter referred to as the surface warm layer) (Fig.

4.19a). The depth of the surface warm layer (approximately 630 m) allows for the falling snow to melt such that rain is observed at the surface. Schmocker (2008) reviewed the findings of Penn (1957) and McNulty (1988) that noted a surface warm layer must have a depth of approximately 366 m or greater for falling snow to transition to rain.

The sounding at t_0 – 6 h (Fig. 4.19b) generally represents a transitional environment in terms of precipitation; more than half of the cases (4 of 7 cases) were transitioning to snow when considering a time period ±3 h of t_0 – 6 h. From t_0 – 12 h to t_0 – 6 h, the environment cooled below 600 hPa, resulting in a decrease in the depth of the surface warm layer, such that the depth of the layer is approximately 204 m at t_0 – 6 h (Figs. 4.19a,b). The cooling below 600 hPa has several likely contributors: 1) weak cold air advection implied via backing winds from approximately 700 hPa to 600 hPa, 2) a deep layer of ascent (approximately 800–250-hPa) partially overlaps with the environment below 600 hPa, and 3) diabatic processes such as melting or sublimation (Fig. 4.19b). Consistent with cooling via diabatic processes, the cross-hair signature is evident at t_0 – 6 h, suggesting heavy snowfall (Cobb and Waldstreicher 2005), which is likely sublimating or partially melting due to presence of the surface warm layer.

By t_0, the time of cold pool occurrence, snow was observed for all of the cases. Also by t_0, the environment has cooled below 800 hPa, such that the temperature profile is below freezing, with the exception of the temperature at 1000 hPa (0.3°C) (Fig. 4.19c). The low-level cooling is likely attributable to diabatic processes. The low-level cooling occurs despite the presence of veering winds from 1000 hPa to 500 hPa, which imply warm air advection. At t_0, the maximum upward vertical velocity at t_0 is aligned slightly below the DGZ (Fig. 4.19c). This alignment is associated with the production of supercooled water droplets, which increases the likelihood of riming, resulting in high-density snow (Cobb and Waldstreicher 2005).

4.3.3.2 Wet Snow Subset

The sounding at t_0 – 12 h for the wet snow subset (Fig. 4.20a) generally represents an environment prior to the observation of precipitation at the surface; in more than half of the cases (11 of 19 cases), precipitation was not observed ±3 h of t_0 – 12 h. At t_0 – 12 h, the temperature profile is below freezing with the exception of the temperature of 0.1ºC at 1000 hPa. Also at t_0 – 12 h, the middle and low levels are marked by the presence of dry air. From t_0 – 12 h to t_0 – 6 h, the environment moistened considerably (Figs. 4.20a,b). At t_0 – 6 h or ±3 h of this time, snow was observed during many of the cases (13 of 19 cases). Diabatic processes, such as sublimation, occurring while the snow fell, likely led to the moistening of the environment. At t_0 – 6 h, the temperature profile (Fig. 4.20b) is below freezing except for the 1000–975-hPa layer, i.e., the surface warm layer. The surface warm layer (approximately 203 m deep) likely leads to partial melting of the snow, resulting in high-density snow. Also at t_0 – 6 h, a veering wind profile in the 1000–600-hPa layer implies warm air advection, which is likely offset by cooling due to diabatic processes and cooling due to ascent.

The sounding at t_0, the time of cold pool occurrence, shows that the low levels (below 850 hPa) have moistened and cooled since t_0 – 6 h (Figs. 4.20b,c). Diabatic processes, such as sublimation, arising from the falling snow are likely responsible for the moistening of the environment by t_0 (Fig. 4.20c) as snow was observed for all of the cases at or ± 3 h of t_0. Diabatic processes are also likely responsible for the low-level cooling. The low-level cooling occurs despite warm air advection indicated by the veering wind profile from 1000 hPa to approximately 600 hPa. The sounding at t_0 (Fig. 4.20c) suggests heavy snow due to the presence of the cross-hair signature (Cobb and Waldstreicher 2005), which is characterized in the sounding by the collocation of the maximum upward vertical velocity, the DGZ, and saturated conditions. The maximum upward vertical velocity exists within a deep layer of upward vertical velocity (800–250-hPa). A portion of the deep layer of upward vertical velocity resides below the DGZ in near-saturated conditions and temperatures above −10ºC, indicating the potential for the production of supercooled water droplets, allowing for riming and thus high-density snow (Cobb and Waldstreicher 2005).

4.3.3.3 Normal Snow Subset

At t_0 – 12 h, most of the cases (4 of 5 cases) feature snow at or ±3 h of t_0 – 12 h; however, one case did not feature any precipitation. This case features dry air that is evident in the composite sounding (Fig. 4.21a). The dry air in this case has been eroded at t_0 – 6 h, and at t_0 – 6 h or ±3 h of this time, snow was observed at the surface for all of the cases allowing for a more homogeneous sample in this subset. At t_0 – 6 h, consistent with observations of snow in all the cases, the temperature profile is entirely below freezing (Fig. 4.21b). The sounding displays the cross-hair signature (Cobb and Waldstreicher 2005) as a strong upward vertical velocity maximum coincides with the DGZ and saturated conditions. The strong upward vertical velocity maximum is evident in a layer of ascent with values between −12 μb s^{-1} and −4 μb s^{-1} from approximately 700 hPa to 400 hPa, which may induce mid-to-low-level cooling. From t_0 – 6 h to t_0, the time of cold pool occurrence, slight cooling occurred throughout the middle and lower troposphere, likely attributable to the strong ascent present at t_0 (Figs. 4.21b,c). At t_0, the ascent maximum is collocated with the DGZ and saturated conditions; thus the cross-hair signature

(Cobb and Waldstreicher 2005) is displayed by the sounding (Fig. 4.21c). Consistently, at or ±3 h of t_0, snow continued to be observed for all of the cases (Fig. 4.21c).

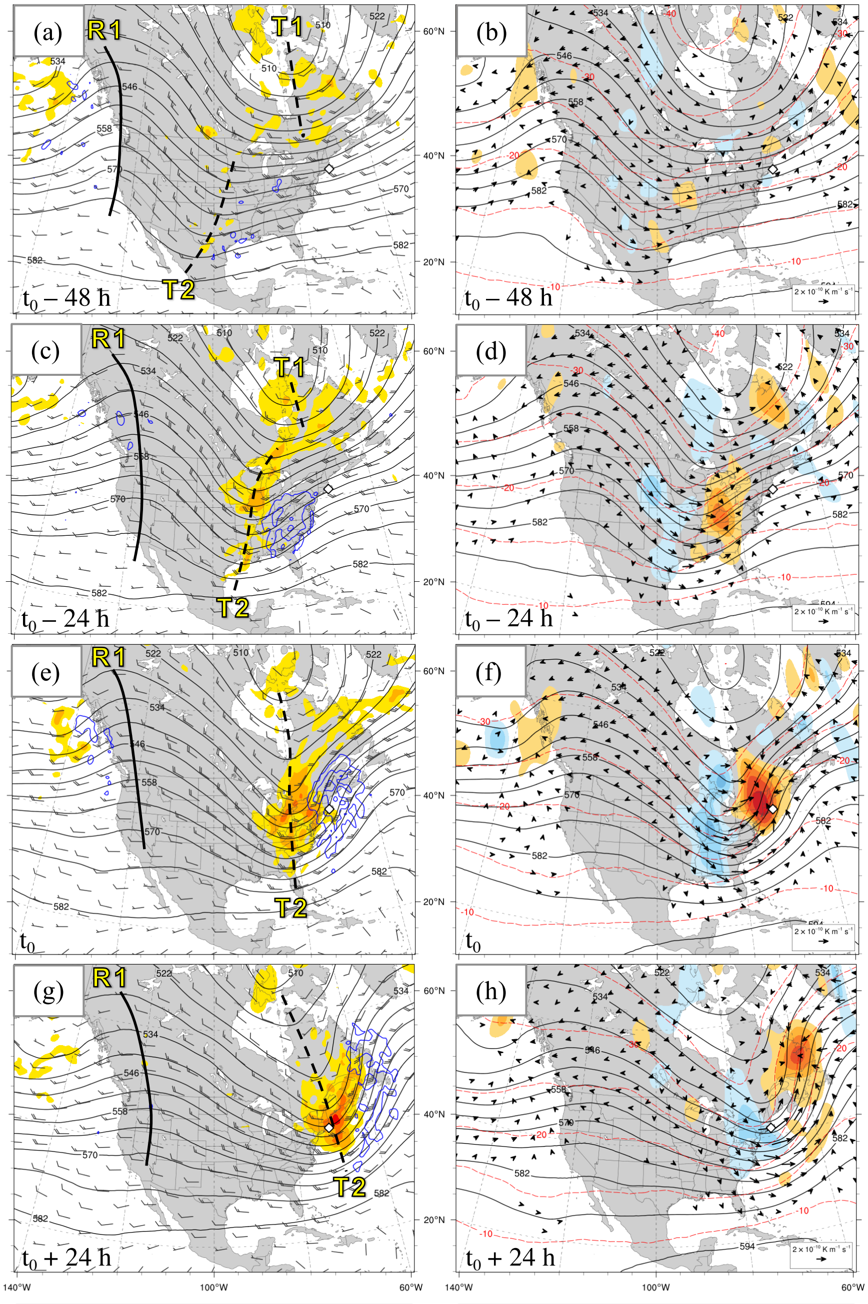

Fig. 4.1 Composites of (left panel) 500-hPa geopotential height (contoured in black every 6 dam), 500-hPa cyclonic relative vorticity (shaded according to the left color bar, 10^{-5} s^{-1}), 500-hPa wind (barbs, m s^{-1}), and 600–400-hPa layer-mean upward vertical velocity (contoured in blue every 2 × 10^{-3} hPa s^{-1}), and (right panel) 600–400-hPa layer-mean **Q**-vector forcing for vertical motion (i.e., the right-hand side of the **Q**-vector form of the QG-omega equation) (shaded according to the right color bar, 10^{-18} Pa^{-1} s^{-3}), geopotential height (contoured in black every 6 dam), potential temperature (contoured in red every 5ºC), **Q** (vectors, ≥ 0.5 × 10^{-10} K m^{-1} s^{-1}) for the Baroclinic Zone: Southwesterly Thermal Wind subset at (a),(b) $t_0 - 48$ h, (c),(d) $t_0 - 24$ h, (e),(f) t_0, and (g),(h) $t_0 + 24$ h. The white diamond with a black outline in each plot denotes the composite center. The dashed and solid lines denote the locations of several troughs and ridges of interest, respectively, as do the labels "T1," "T2," and "R1."

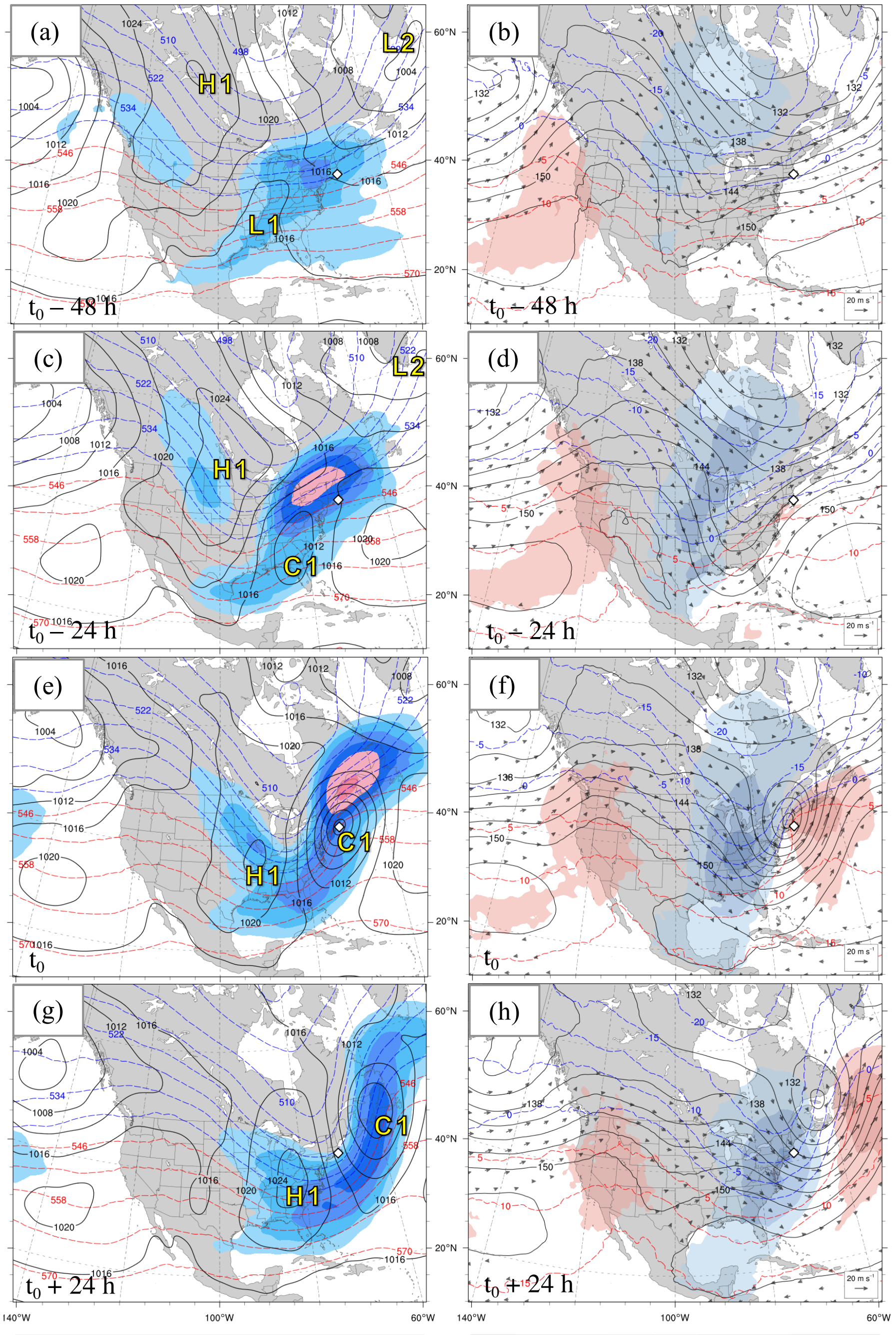

Fig. 4.2 Composites of (left panel) 250-hPa wind speed (shaded according to the left color bar, m s^{-1}), 1000–500-hPa thickness [red (blue) dashed contours for values > (≤) 540 dam, contoured every 6 dam], and MSLP (contoured in black every 4 hPa), and (right panel) 850-hPa geopotential height (contoured in black every 3 dam), temperature [red (blue) dashed contours for values > (≤) 0ºC, contoured every 5ºC], normalized temperature anomalies (shaded according to the right color bar, σ), and wind (vectors, ≥ 5 m s^{-1}) for the Baroclinic Zone: Southwesterly Thermal Wind subset at (a),(b) t_0 – 48 h, (c),(d) t_0 – 24 h, (e),(f) t_0, and (g),(h) t_0 + 24 h. The white diamond with a black outline denotes the composite center. The yellow labels denote the locations of surface high and low pressure systems of interest.

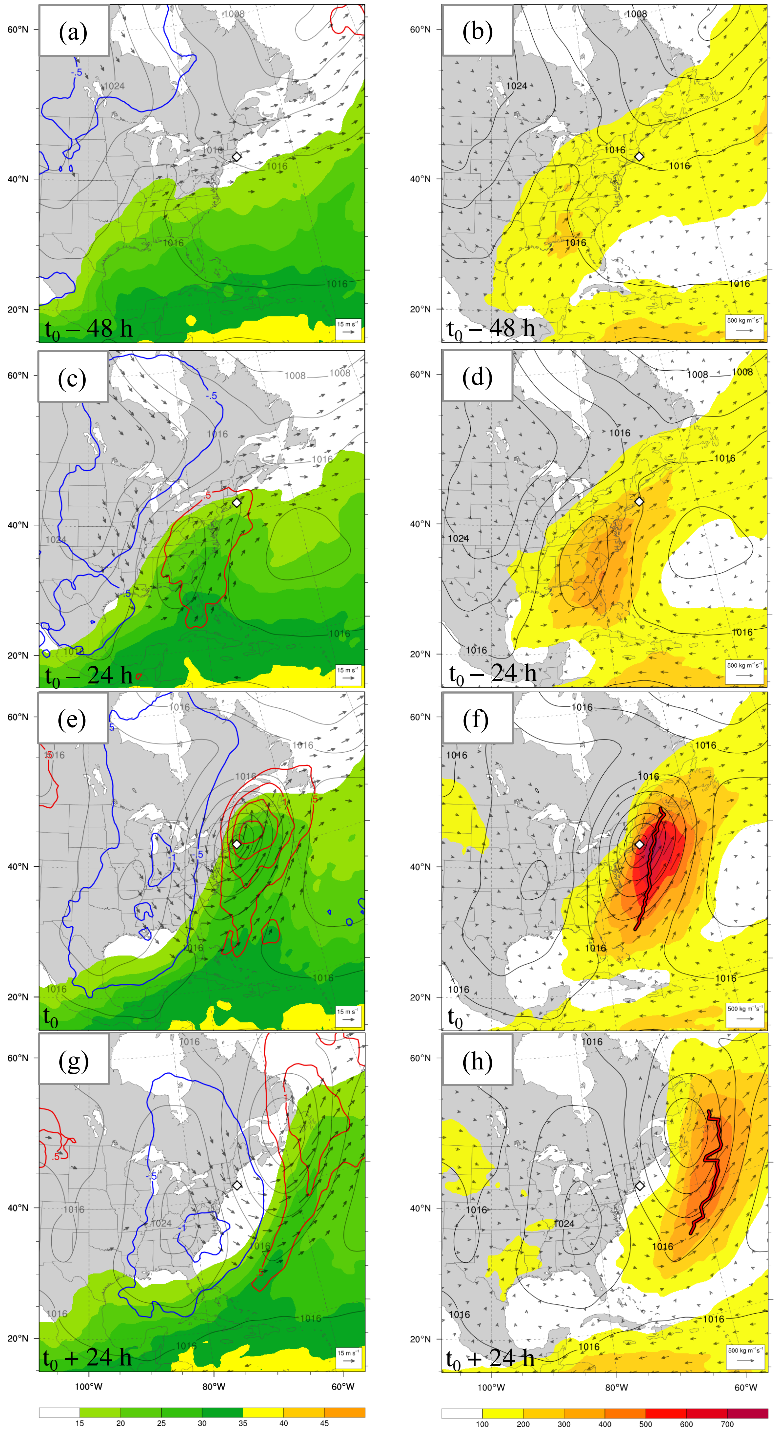

Fig. 4.3 Composites of (left panel) PWAT (shaded according to the left color bar, mm), normalized PWAT anomalies [positive (negative) contoured in red (blue), contoured every 0.5 σ], 850-hPa wind (vectors, ≥ 8 m s^{-1}), and MSLP (contoured in gray every 4 hPa), and (right panel) IVT magnitude (shaded according to the right color bar, kg m^{-1} s^{-1}) with IVT vectors (≥ 25 kg m^{-1} s^{-1}) overlaid, AR axis (red line with black outline), and MSLP (contoured every 4 hPa) for the Baroclinic Zone: Southwesterly Thermal Wind subset at (a),(b) $t_0 - 48$ h, (c),(d) $t_0 - 24$ h, (e),(f) t_0, and (g),(h) $t_0 + 24$ h. The white diamond with a black outline denotes the composite center.

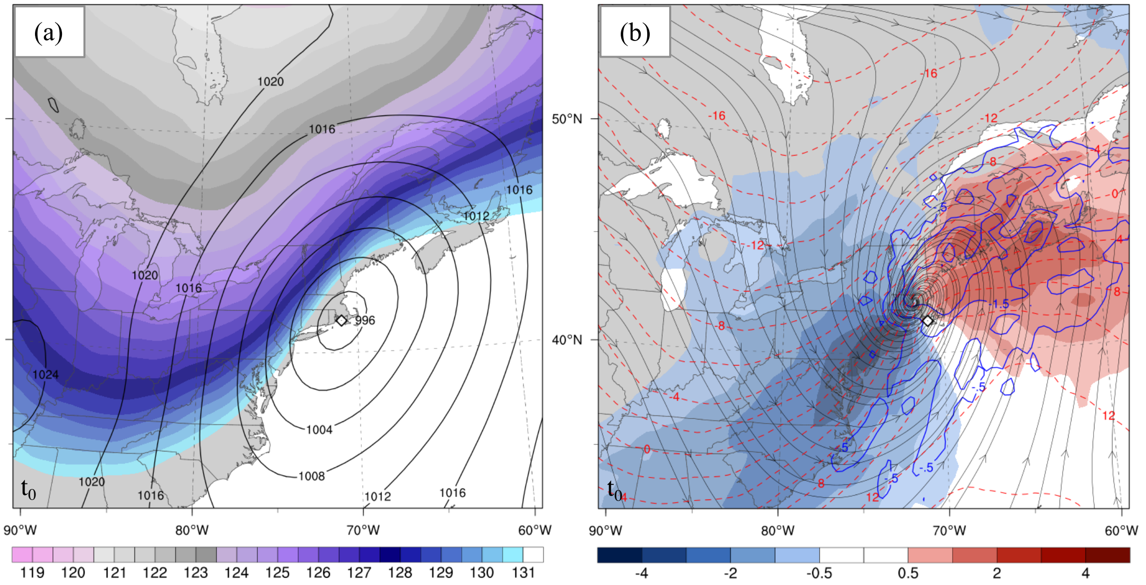

Fig. 4.4 Composites of (left panel) 1000–850-hPa thickness (shaded according to the left color bar, dam) and MSLP (contoured every 4 hPa), and (right panel) 1000–850-hPa layer mean temperature advection [shaded according to the right color bar, K (3 h)$^{-1}$], cooling due to ascent [contoured in blue every −0.5 K (3 h)$^{-1}$], temperature (contoured in red every 2ºC), and streamlines (contoured in gray) for the Baroclinic Zone: Southwesterly Thermal Wind subset at (a),(b) t_0. The white diamond with a black outline in each plot denotes the composite center.

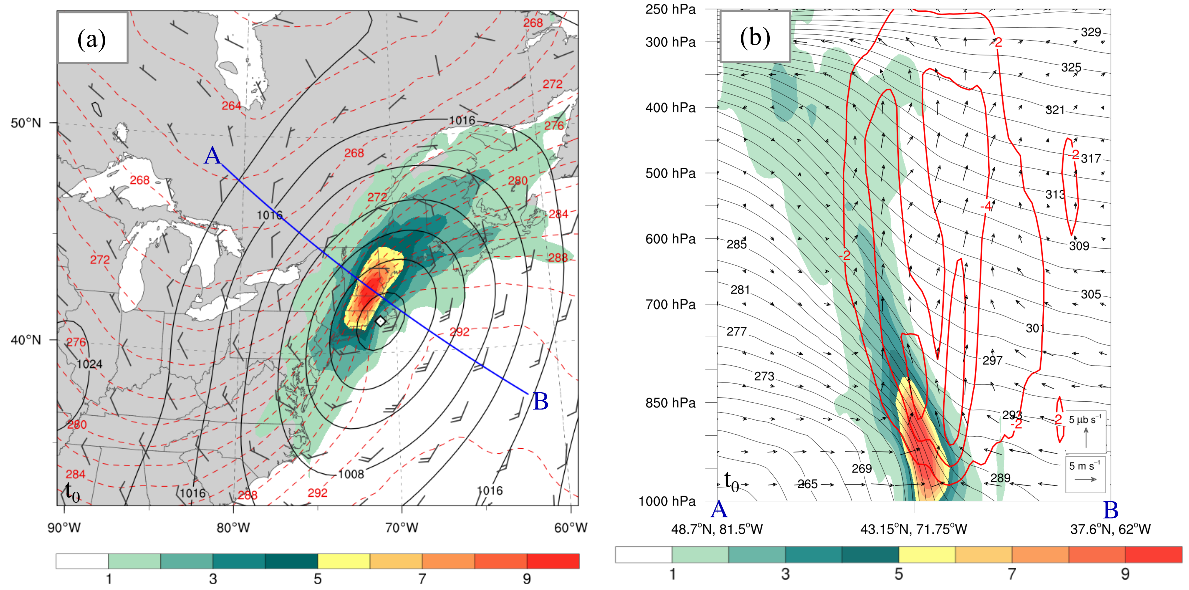

Fig. 4.5 Composites of (left panel) 925–850-layer mean frontogenesis [shaded according to the left color bar, K (100 km)$^{-1}$ (3 h)$^{-1}$], 925–850-layer mean potential temperature (contoured in dashed red every 2 K), and MSLP (contoured in black every 4 hPa), and (right panel) a cross section, corresponding to the blue line in the left panel, of frontogenesis [shaded according to the right color bar, K (100 km)$^{-1}$ (3 h)$^{-1}$], potential temperature (contoured in black every 2 K), vertical velocity (contoured in red every 2 μb s^{-1} ≤ -2 μb s^{-1}), and ageostrophic circulation in the plane of the cross section (vectors) for the Baroclinic Zone: Southwesterly Thermal Wind subset at (a),(b) t_0. The middle tick-mark on the x-axis of the cross section indicates the center of the cross section.

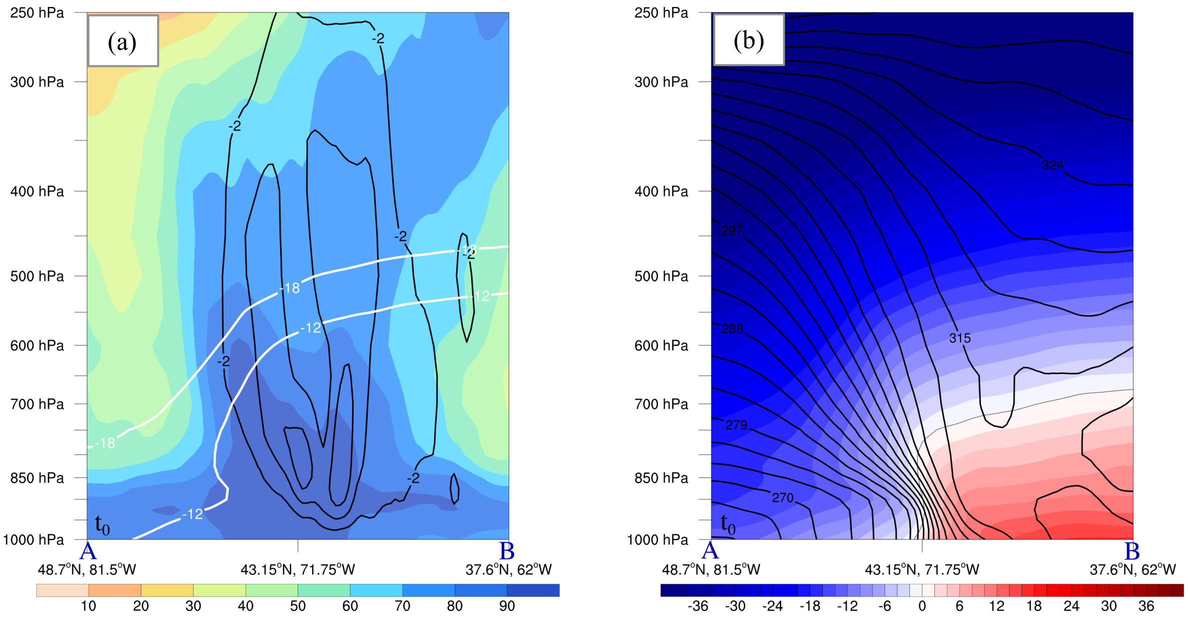

Fig. 4.6 Composites of cross sections along the blue line in Fig. 4.5a of (left panel) relative humidity (shaded according to the left color bar, %), vertical velocity (contoured in black every 2 μb s^{-1}), and the upper (−18ºC) and lower (−12ºC) bounds of the DGZ (contoured in white), and (right panel) temperature (shaded according to the right color bar, ºC), freezing level (thin black line, 0ºC), and equivalent potential temperature (contoured every 3 K) for the Baroclinic Zone: Southwesterly Thermal Wind subset at (a),(b) t_0.

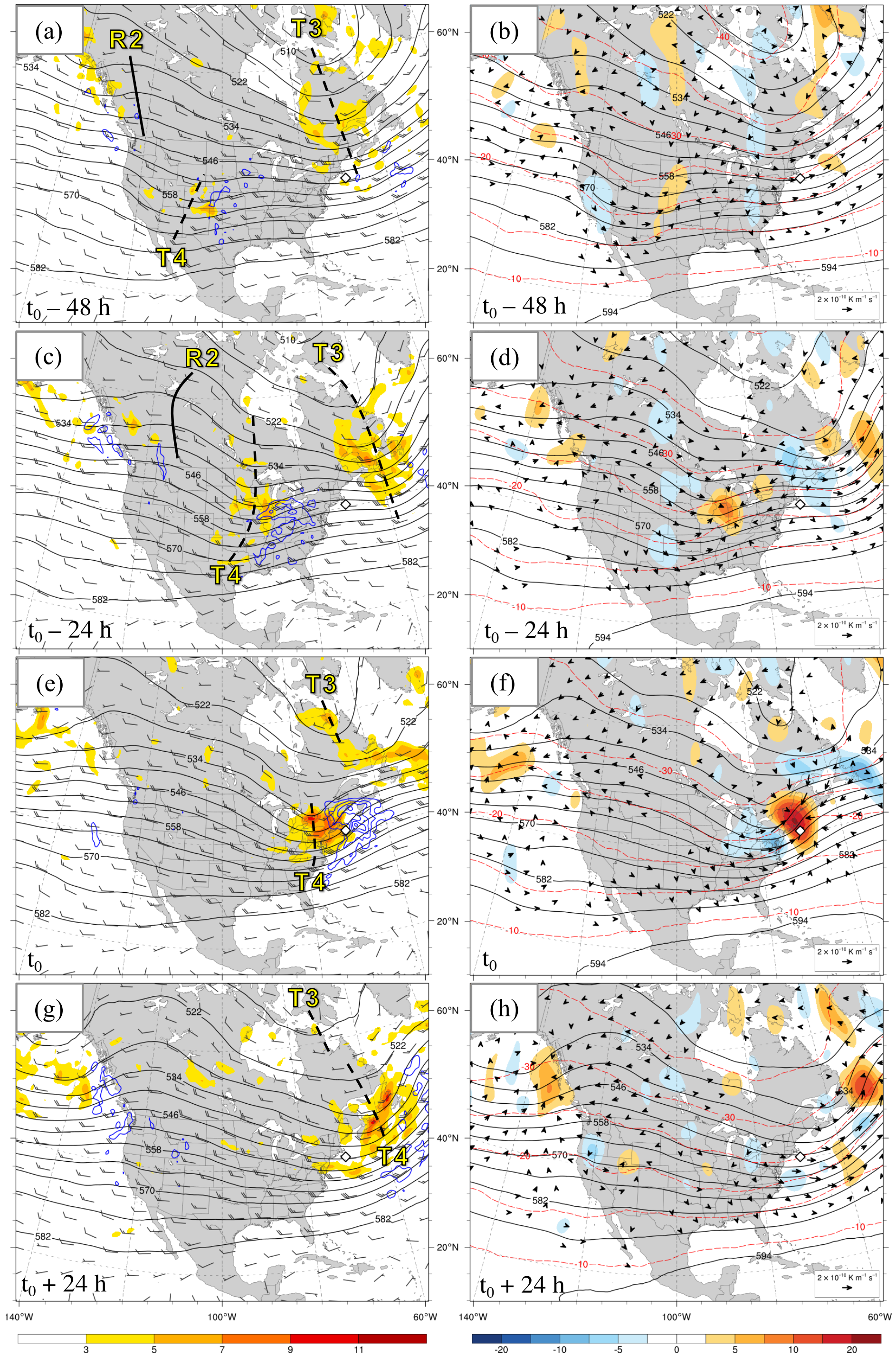

Fig. 4.7 As in Fig. 4.1 except for the Baroclinic Zone: Westerly Thermal Wind subset. The dashed and solid lines denote the locations of several troughs and ridges of interest, respectively, as do the labels "T3," "T4," and "R2."

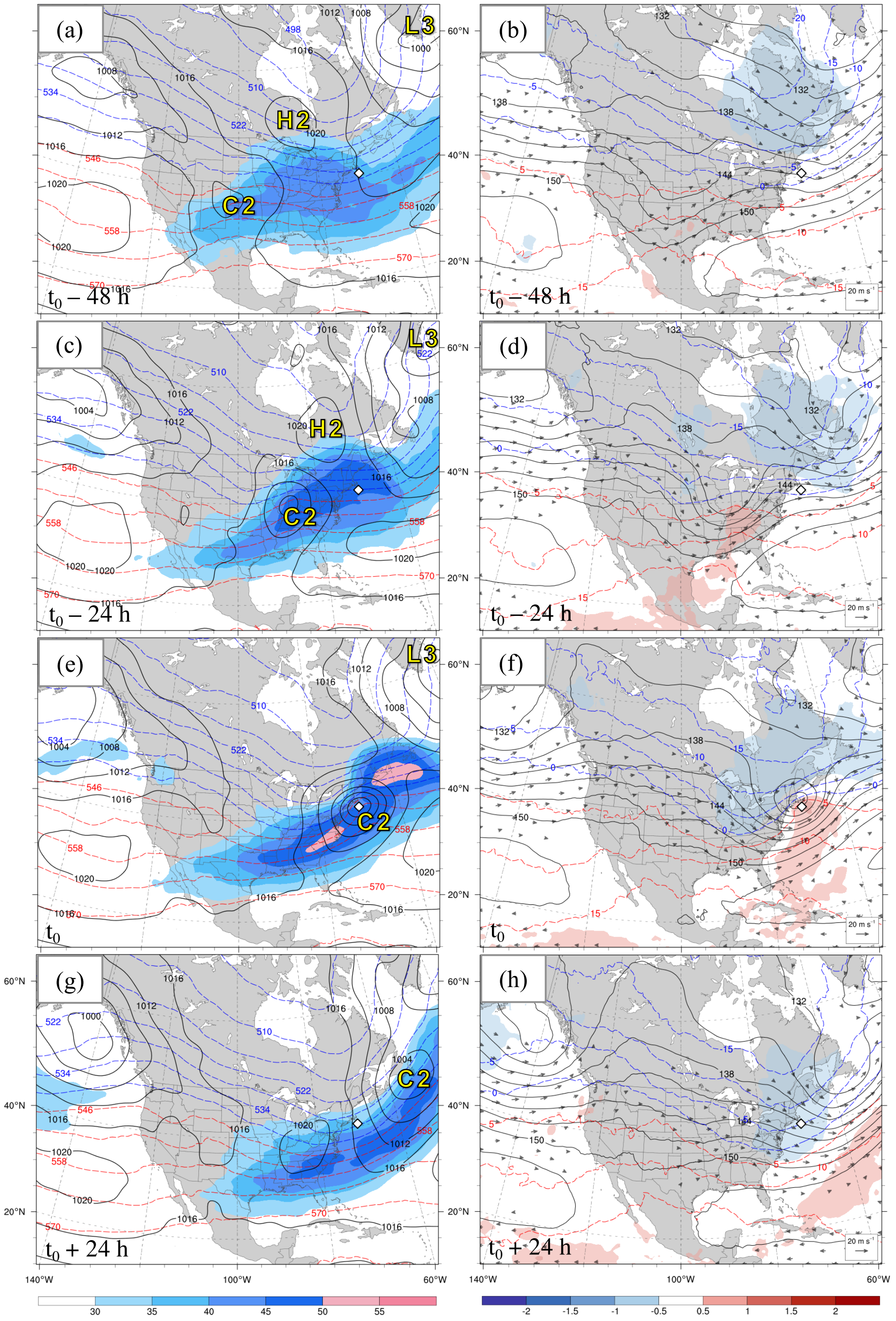

Fig. 4.8 As in Fig. 4.2 except for the Baroclinic Zone: Westerly Thermal Wind subset.

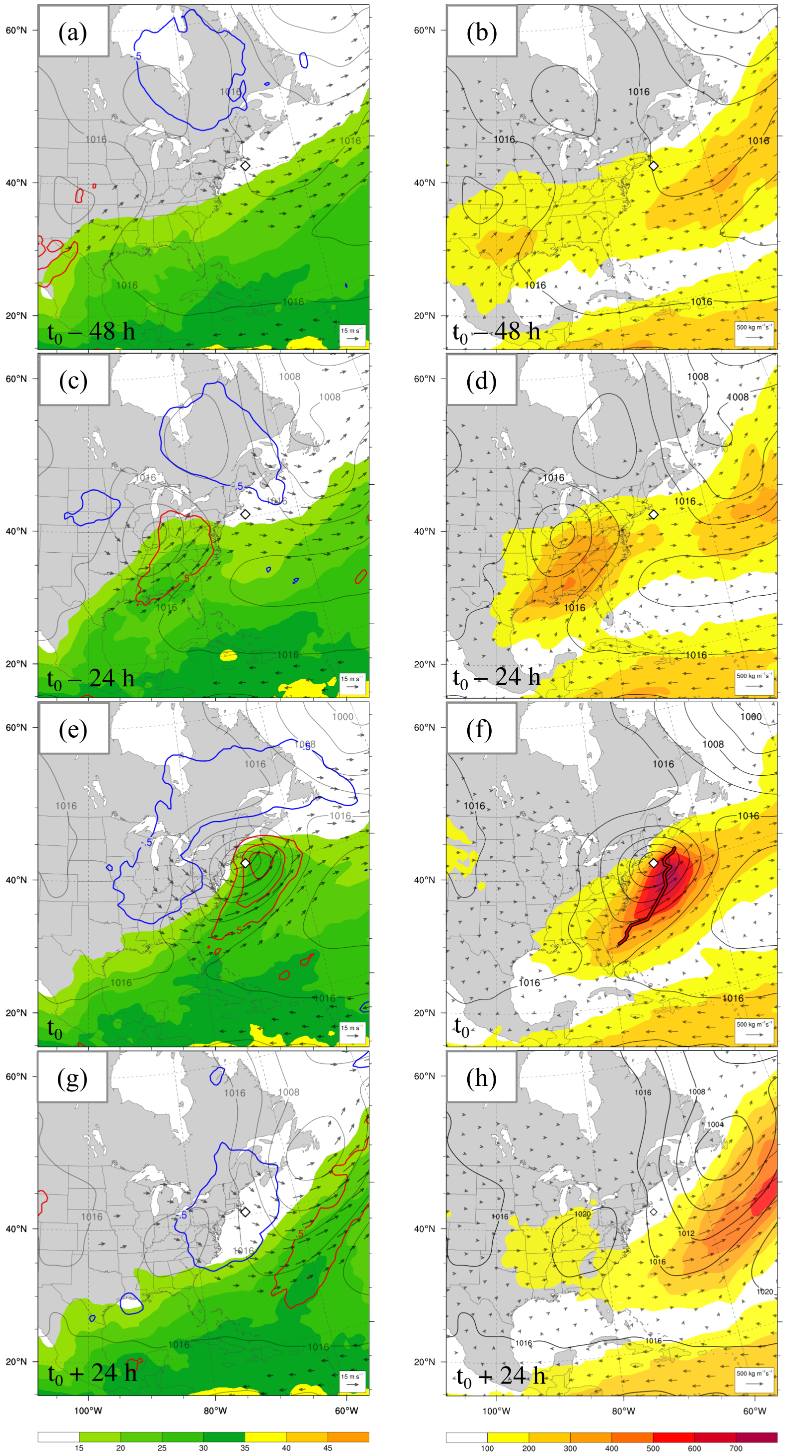

Fig. 4.9 As in Fig. 4.3 except for the Baroclinic Zone: Westerly Thermal Wind subset.

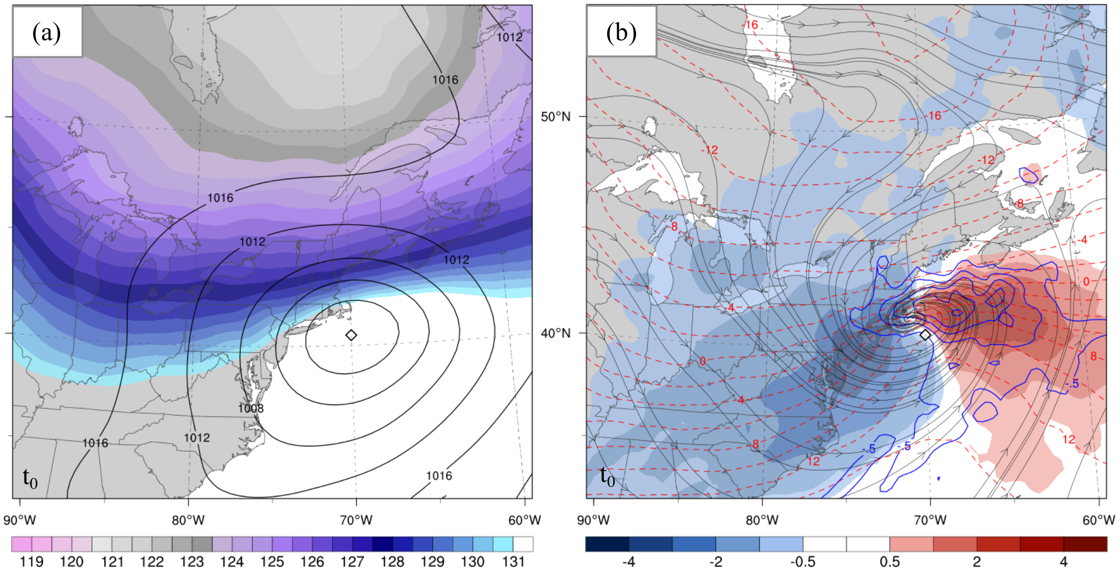

Fig. 4.10 As in Fig. 4.4 except for the Baroclinic Zone: Westerly Thermal Wind subset.

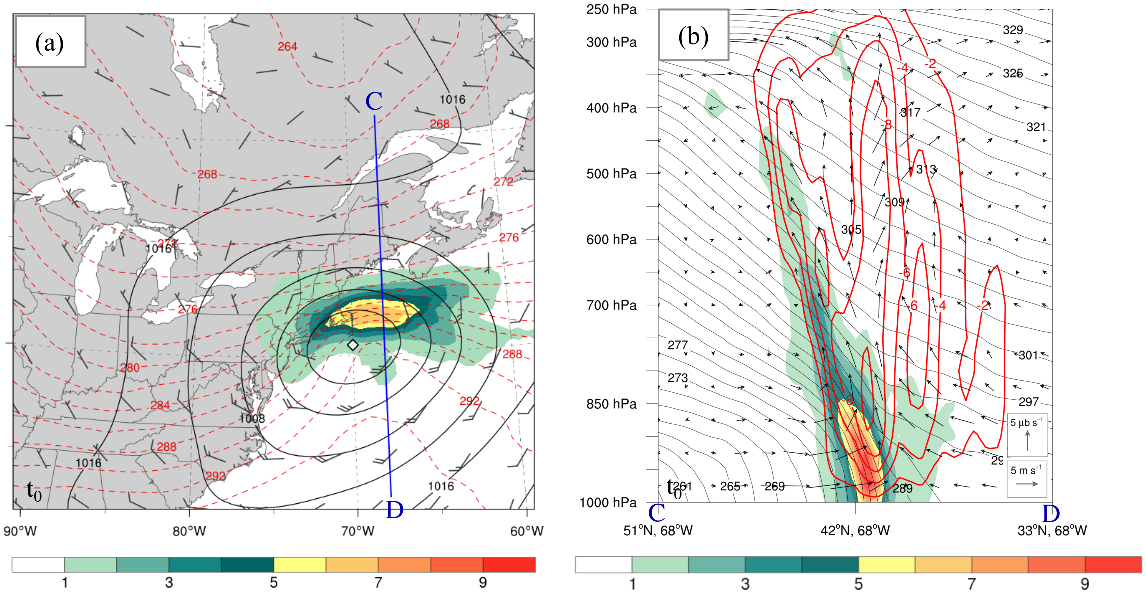

Fig. 4.11 As in Fig. 4.5 except for the Baroclinic Zone: Westerly Thermal Wind subset. The cross section shown in the right panel corresponds to the blue line in the left panel.

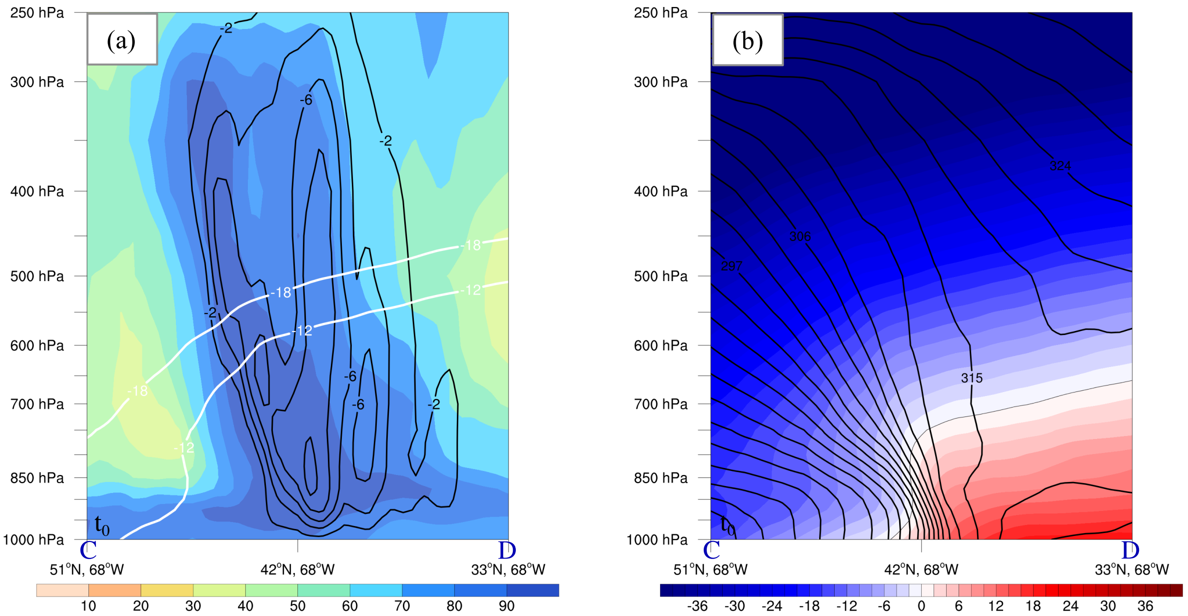

Fig. 4.12 As in Fig. 4.6 except for the Baroclinic Zone: Westerly Thermal Wind subset. The cross sections correspond to the blue line in Fig. 4.11a.

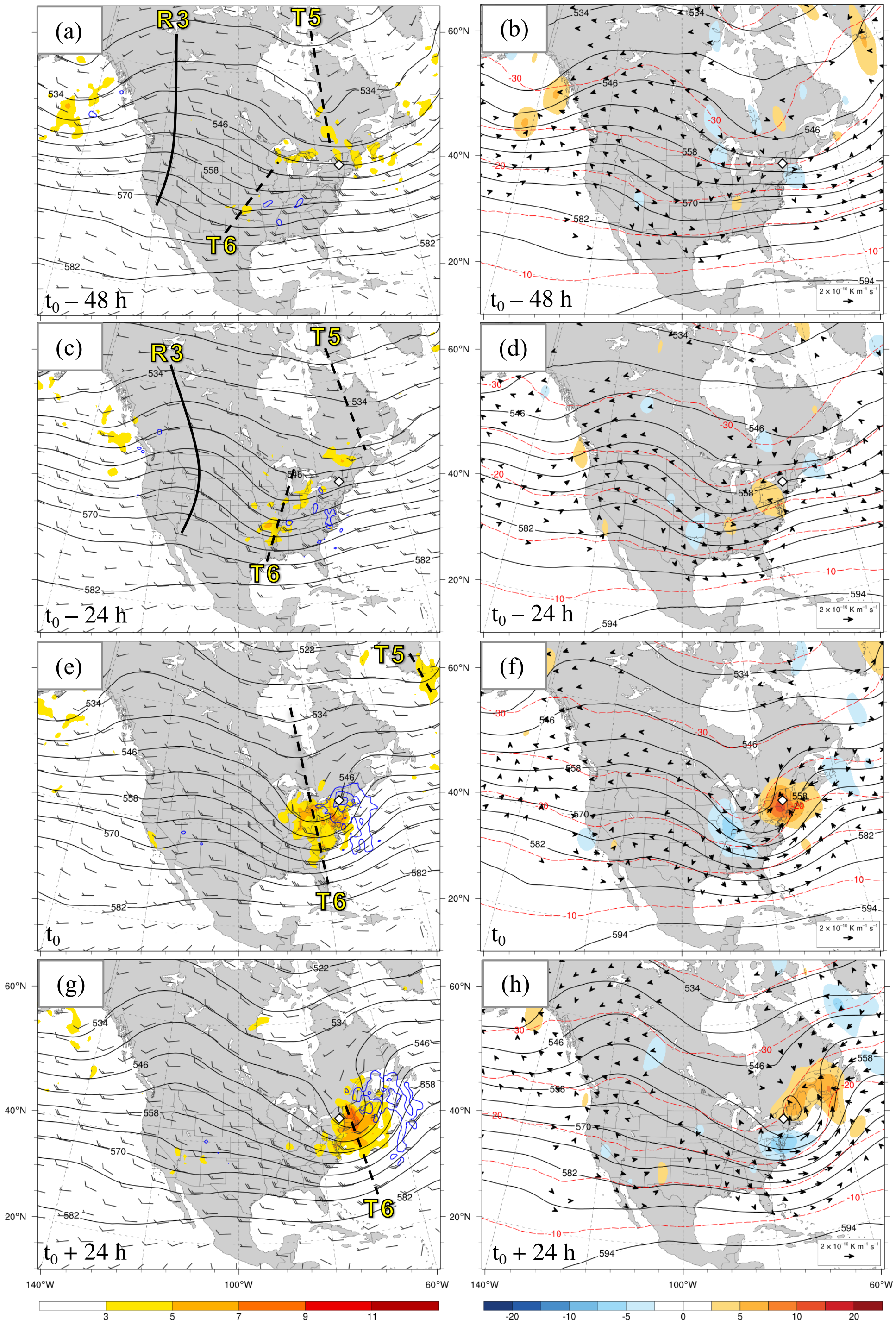

Fig. 4.13 As in Fig. 4.1 except for the Cold Pool category. The dashed and solid lines denote the locations of several troughs and ridges of interest, respectively, as do the labels "T5," "T6," and "R3."

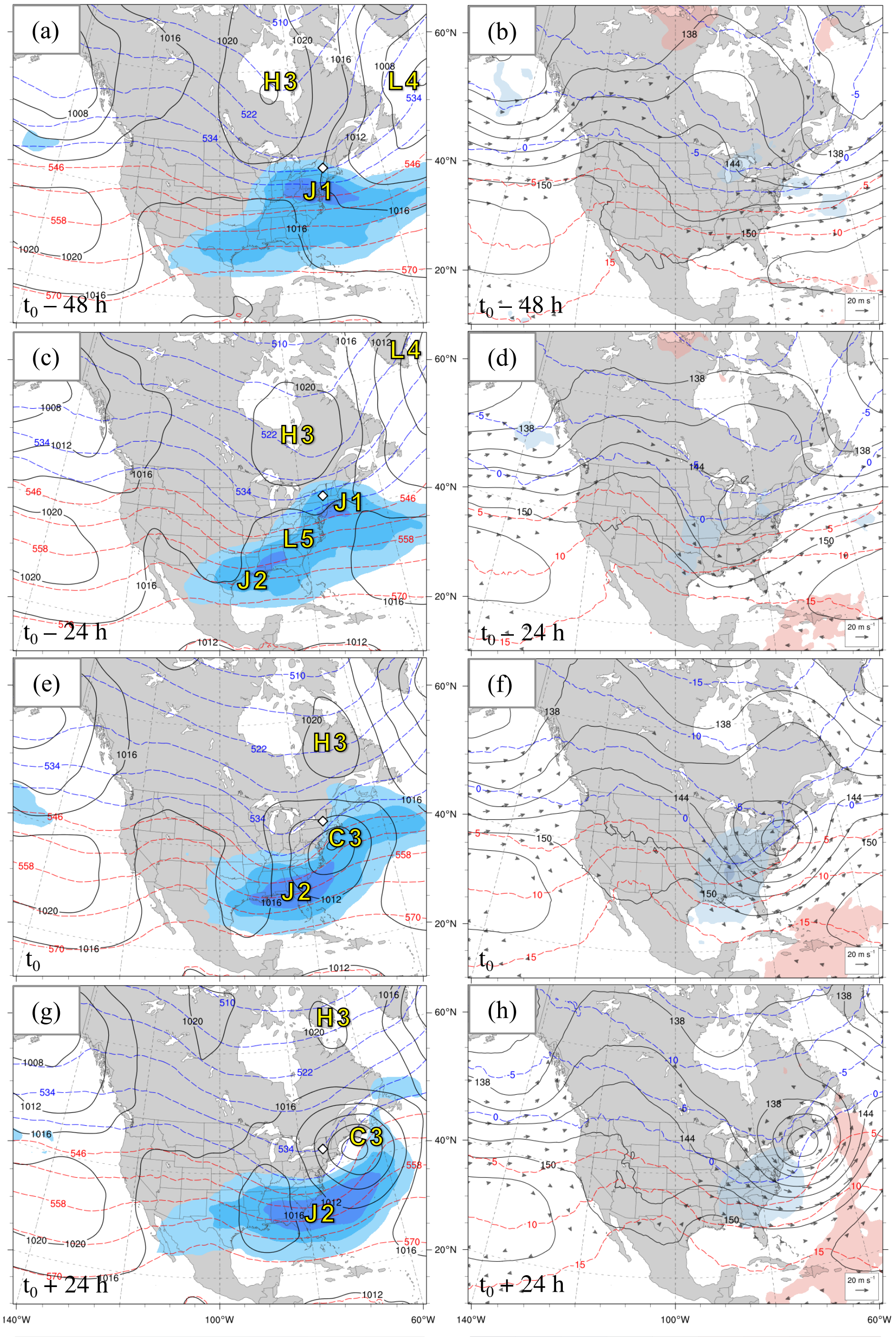

Fig. 4.14 As in Fig. 4.2 except for the Cold Pool category. The yellow labels "J1" and "J2" correspond to jet streaks of interest, and the remaining yellow labels denote the locations of surface high and low pressure systems of interest. The composite center (i.e., the white diamond with a black outline as denoted in Fig. 4.2) is not shown in the right panel but corresponds to the location of the composite center in the left panel.

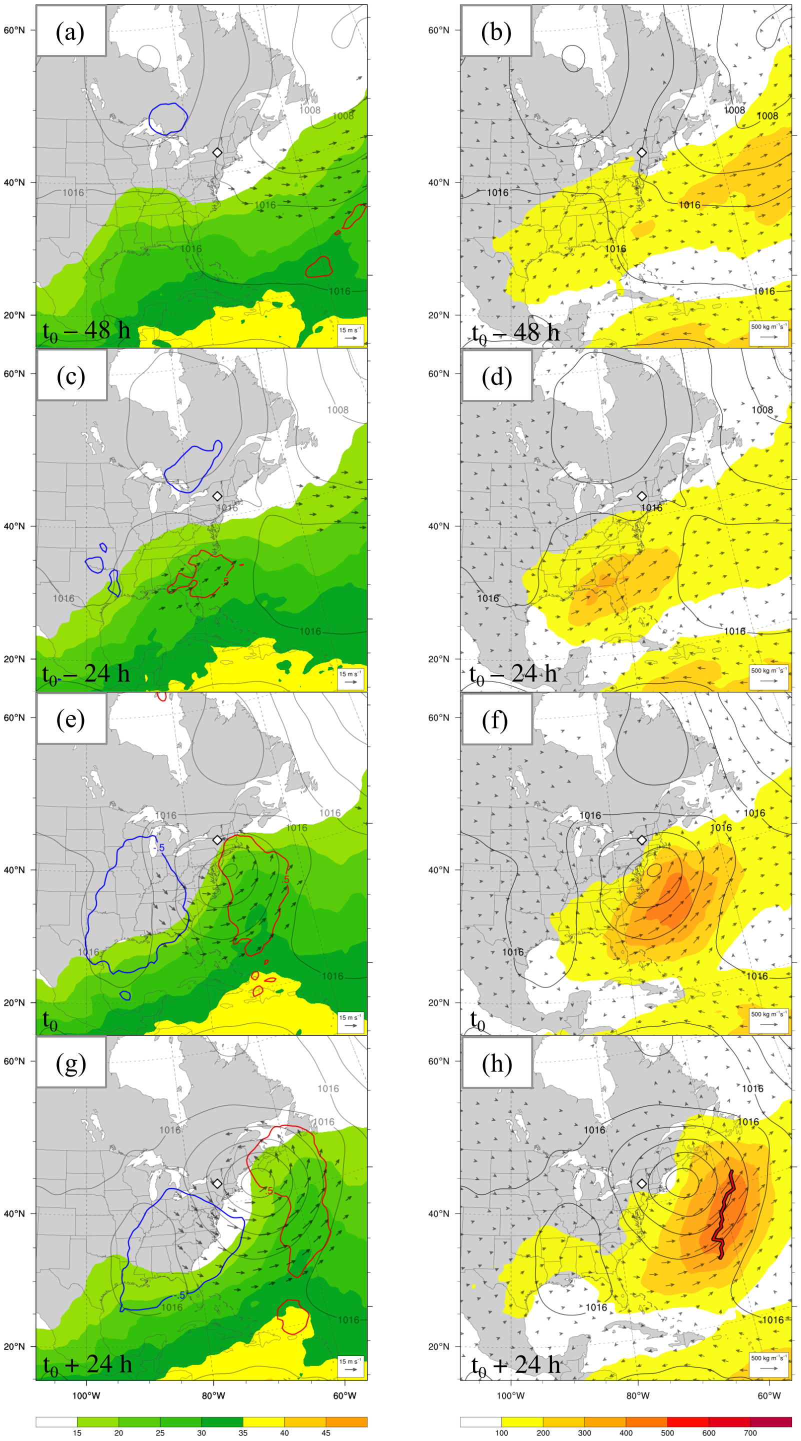

Fig. 4.15 As in Fig. 4.3 except for the Cold Pool category.

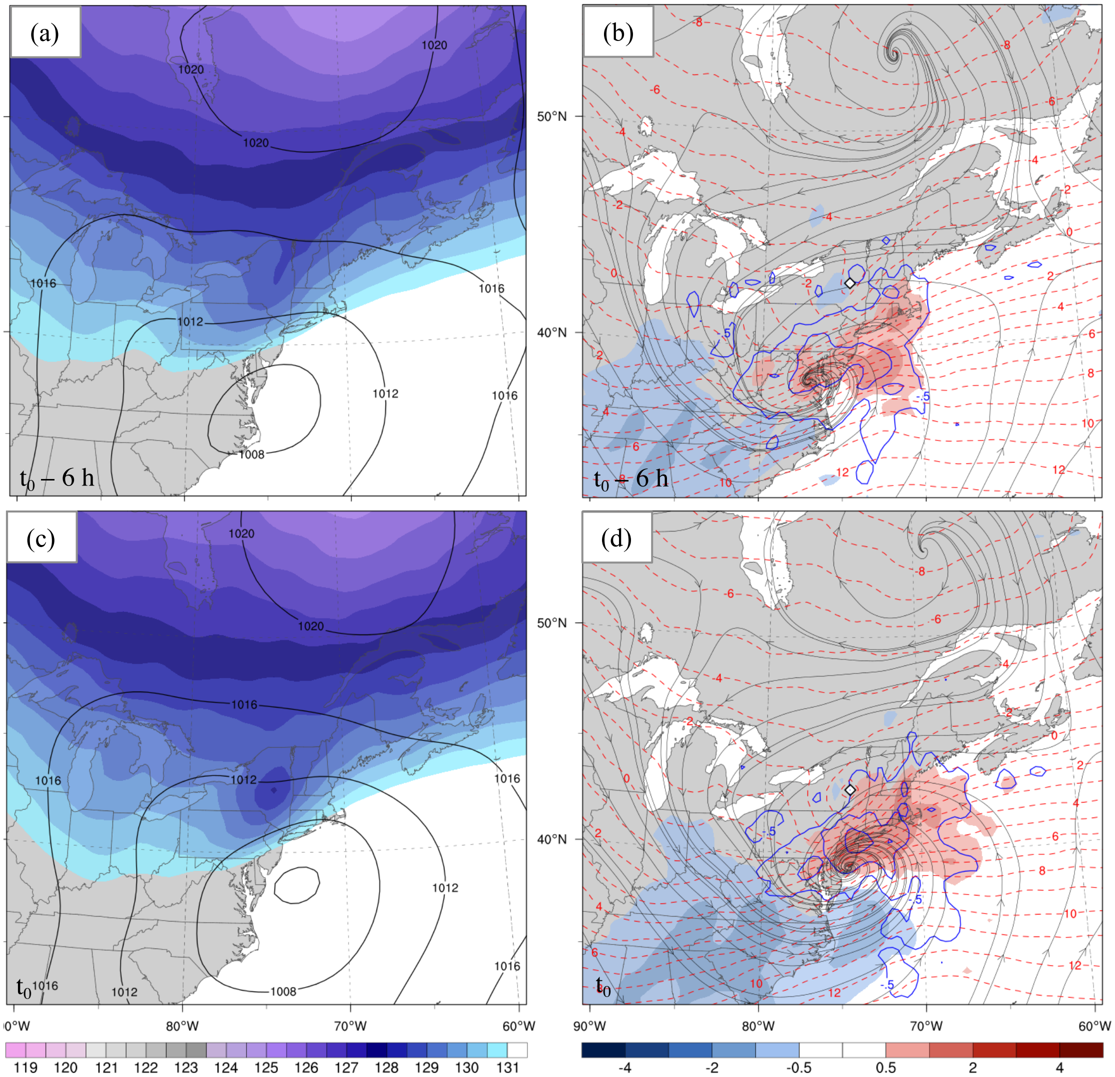

Fig. 4.16 As in Fig. 4.4 except for the Cold Pool category at (a),(b) t_0 – 6 h and (c),(d) t_0. The 1000–850-hPa layer-mean temperature is contoured in dashed red lines every 1ºC.

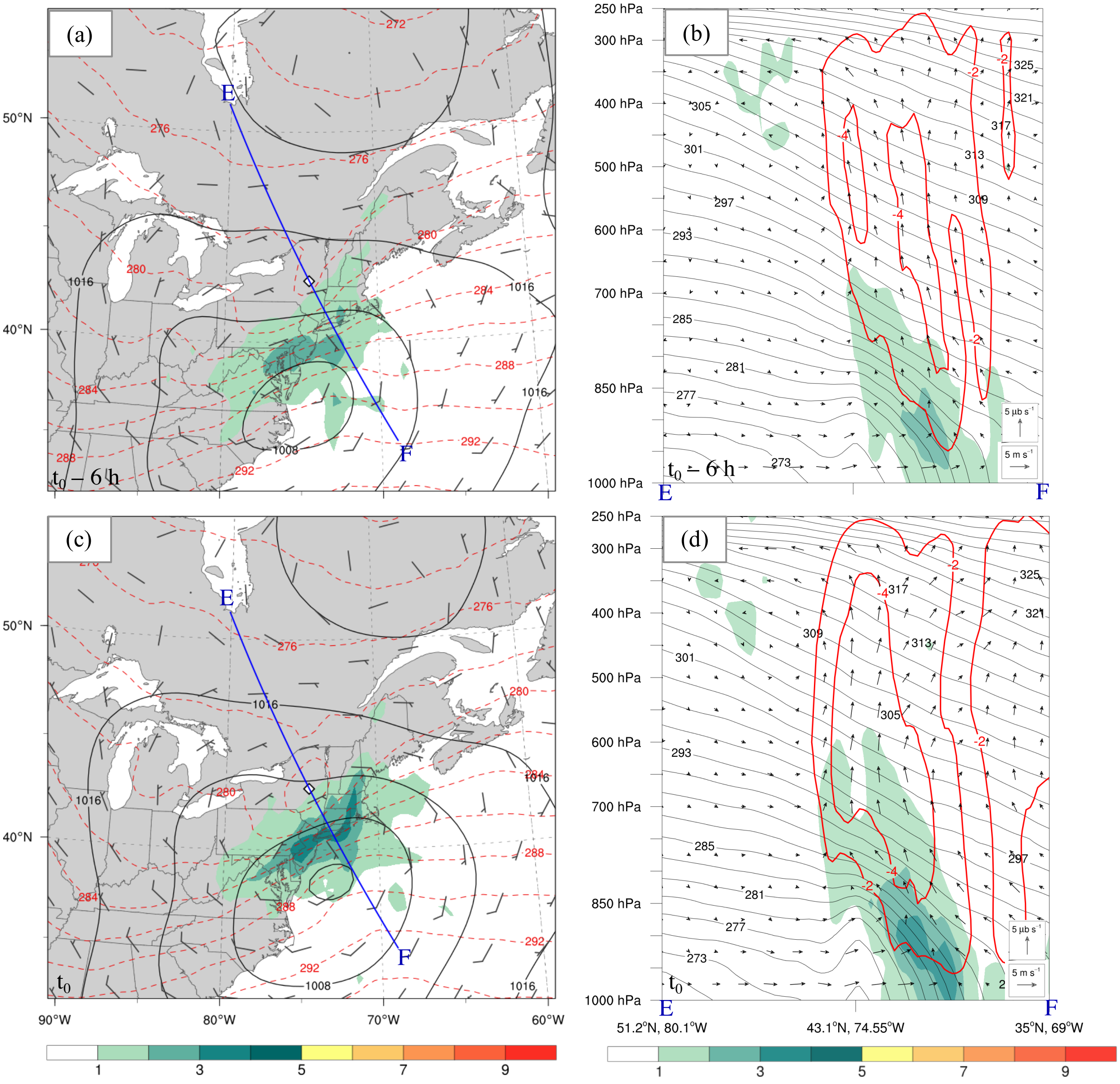

Fig. 4.17 As in Fig. 4.5 except for the Cold Pool category at (a),(b) $t_0 – 6$ h and (c),(d) t_0.

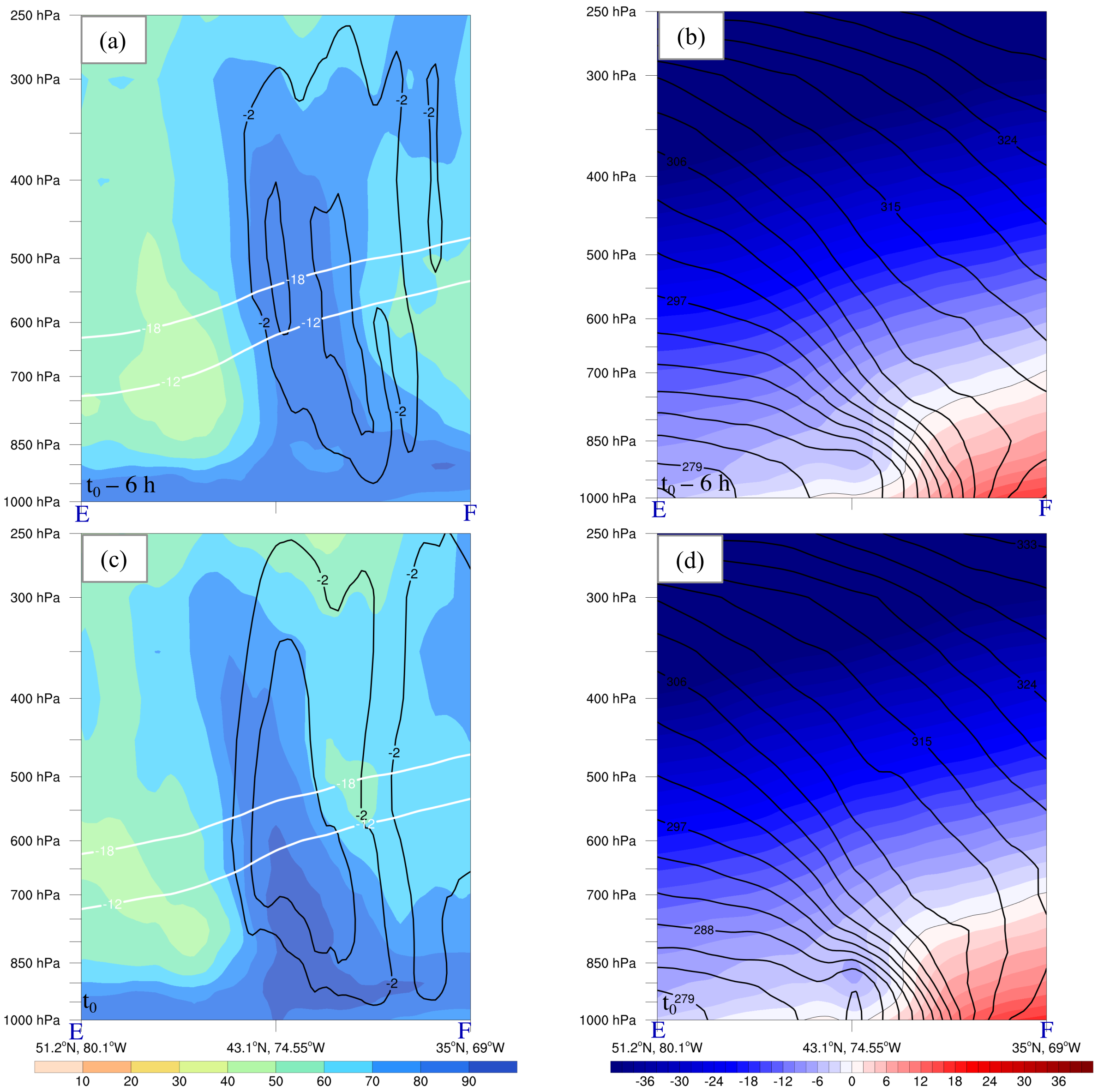

Fig. 4.18 As in Fig. 4.6 except for the Cold Pool category at (a),(b) t_0 – 6 h and (c),(d) t_0. The cross sections correspond to the blue lines in Figs. 4.17a,c.

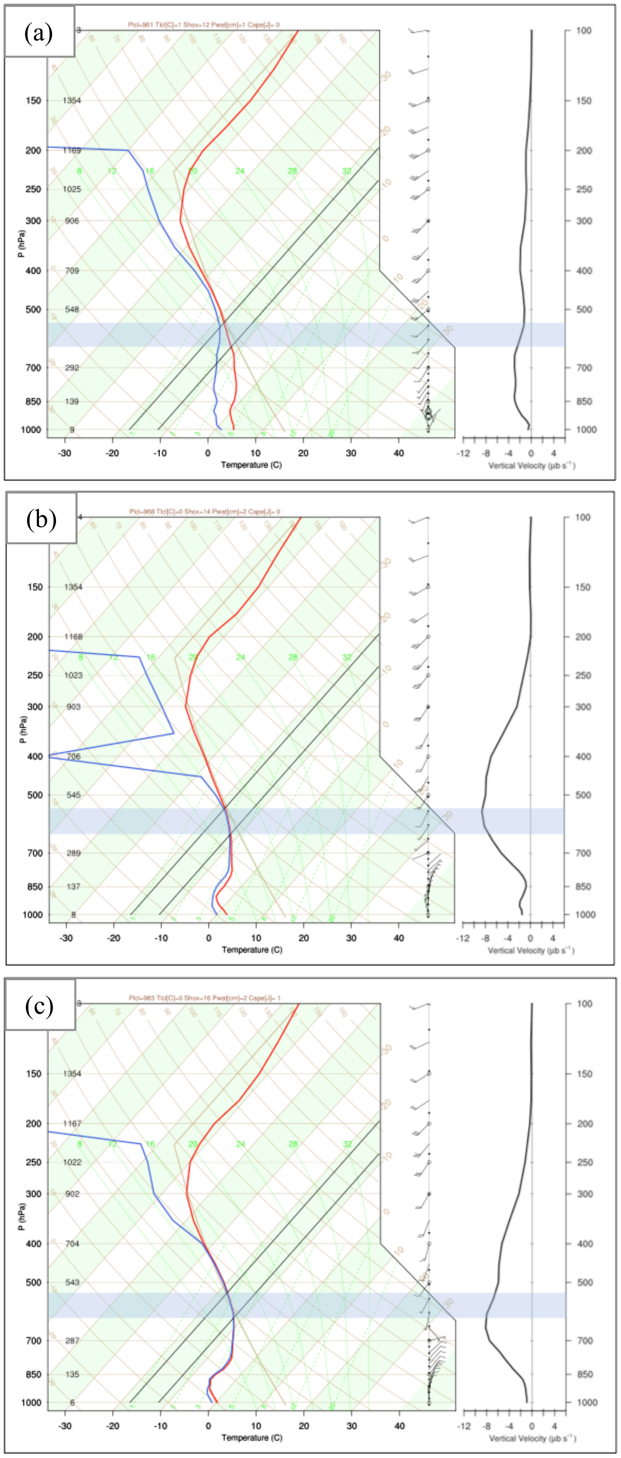

Fig. 4.19 Composite sounding with winds (m s^{-1}) and vertical velocity (μb s^{-1}) for the changeover subset of the Cold Pool category at (a) t_0 – 12 h, (b) t_0 – 6 h, and (c) t_0. The isotherms corresponding to the upper (−18ºC) and lower (−12ºC) bounds of the DGZ are in black, and the blue shading corresponds to the portion of the temperature profile within the DGZ. The composite soundings represent the average vertical profiles over the point of maximum snowfall accumulation within the cold pool and t_0 corresponds to the time when the cold pool first appeared over the point of maximum snowfall accumulation.

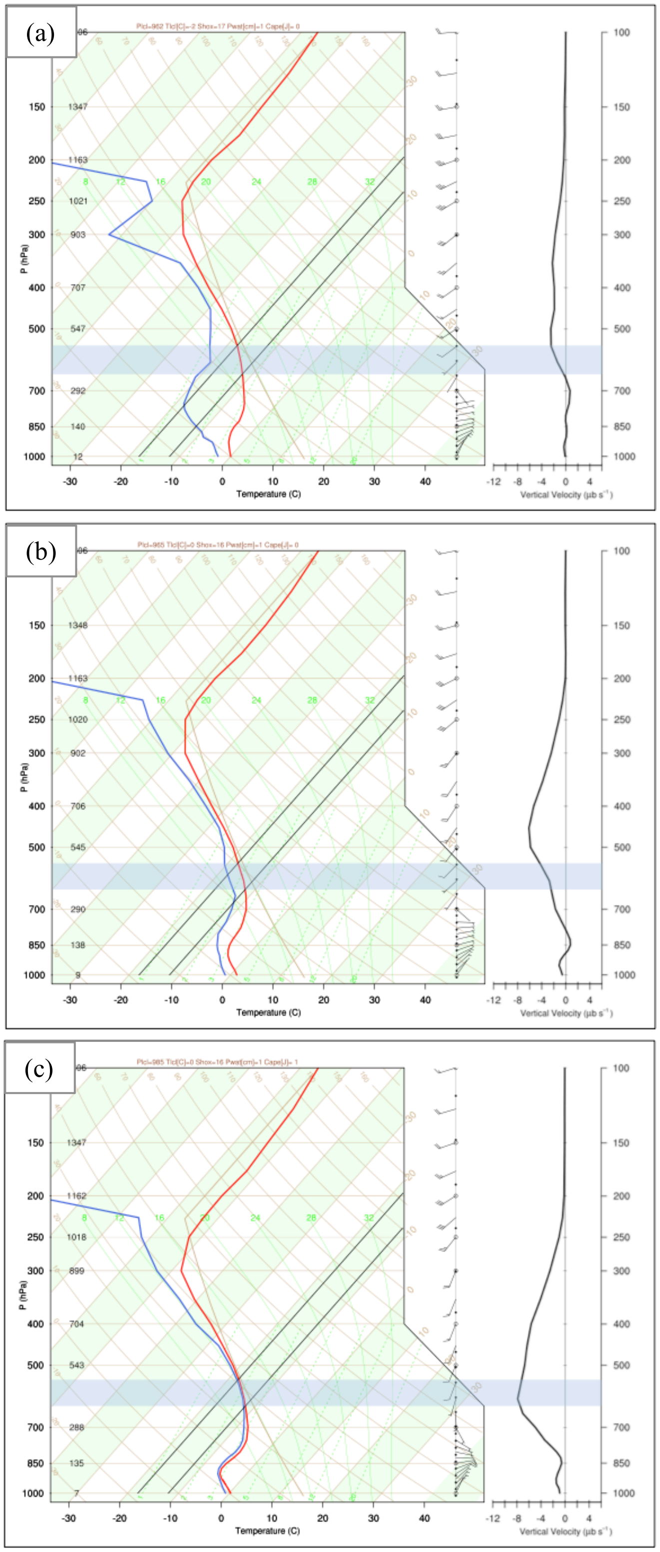

Fig. 4.20 As in Fig. 4.19 except for the wet snow subset of the Cold Pool category.

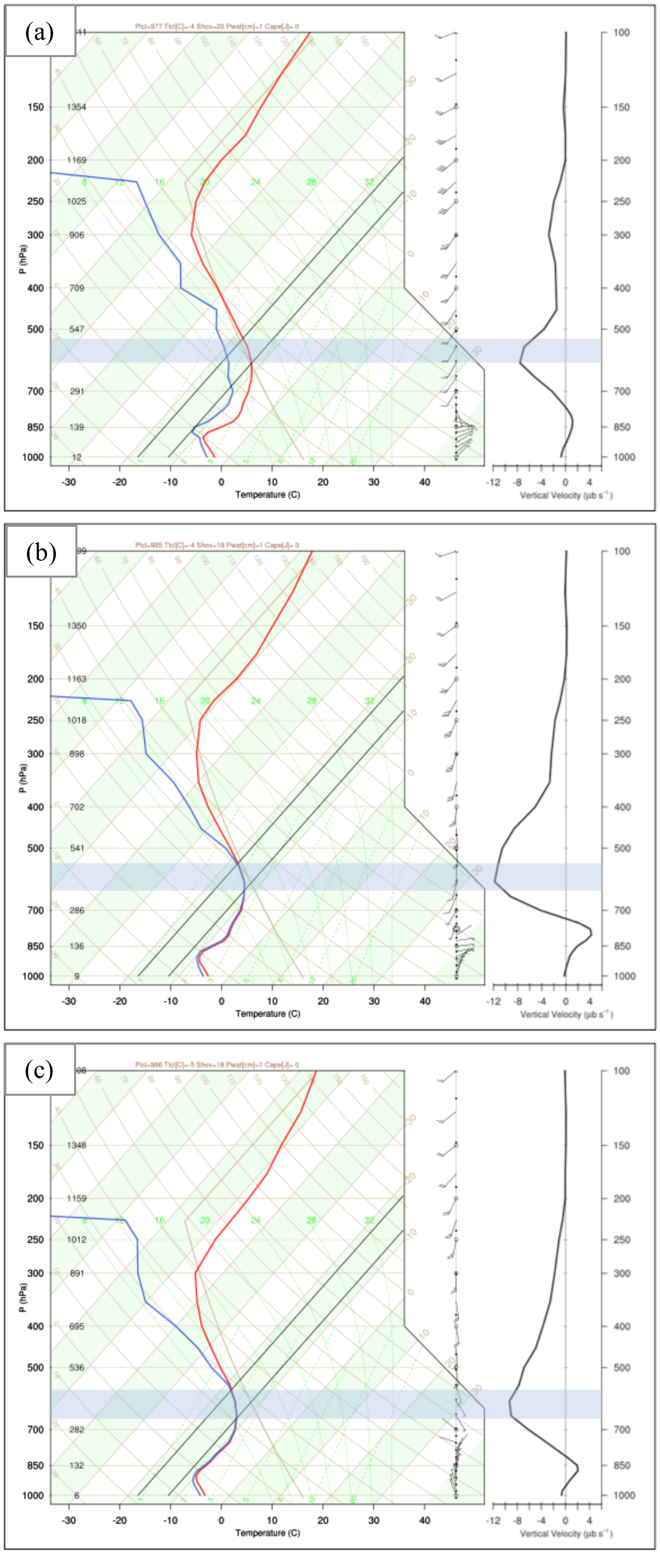

Fig. 4.21 As in Fig. 4.19 except for the normal snow subset of the Cold Pool category.

5. Summary, Discussion, and Suggestions for Future Work

5.1 Summary

Motivated by the opportunity to improve scientific understanding and forecaster situational awareness of major transition season Northeast snowstorms, this study examined this class of snowstorms by means of a multiscale analysis. The multiscale analysis included both a climatology and composite analysis and emphasized ARs and lower-tropospheric cold air. Major transition season Northeast snowstorms used in the climatology and composite analysis were identified from NCEI's monthly Storm Data publication during 1983–2013. From the identified snowstorms, this study found that major transition season Northeast snowstorms featured a variety of lower-tropospheric cold air patterns that provided a means to group similar snowstorms. The climatology focused on the snowstorms grouped by both temporal characteristics and lower-tropospheric cold air pattern, and the composite analysis focused on the snowstorms grouped by lower-tropospheric cold air pattern. In the composite analysis, the lower-tropospheric cold air pattern served as the basis for case-centered composites (see section 2.5 for details).

In the climatology, snowstorms grouped by temporal characteristics reveal the following key conclusions:

1) Spring snowstorms are the dominant type of major transition season Northeast snowstorms, with the majority occurring in March.

2) Spatial distributions of cases with heavy snowfall for the months of March, April, and November tend to exhibit latitudinal gradients where more cases with heavy snowfall

occur at high latitudes of the Northeast domain than at low latitudes of the Northeast domain.

3) March, April, October, and November feature maxima in number of cases with heavy snowfall per month in regions of elevated terrain.

4) ARs are frequently observed during the major transition season Northeast snowstorms in all months.

In the climatology, snowstorms grouped by lower-tropospheric cold air pattern reveal the following key conclusions:

1) The Cold Pool category features the widespread occurrence of cold pools across the Northeast domain at the initial and midpoint times of the cold pools.

2) Maxima in cold pool occurrence are typically located in regions of elevated terrain at the initial and midpoint times of the cold pools.

3) Each lower-tropospheric cold air pattern exhibits a distinct spatial distribution of cases with heavy snowfall.

4) All of the lower-tropospheric cold air patterns feature maxima in number of cases with heavy snowfall in regions of elevated terrain.

Results from the climatology indicate that ARs are characteristic ingredients in the Baroclinic Zone: Southwesterly Thermal Wind subset and the Cold Pool category. First, the Baroclinic Zone: Southwesterly Thermal Wind subset and the Cold Pool category have AR fractions over 50% during all case days, demonstrating that ARs are frequently identified during snowstorms for these two lower-tropospheric cold air patterns. Second, the Baroclinic Zone: Southwesterly Thermal Wind subset and the Cold Pool category feature high AR axis density values over the Northeast domain during all case days. Third, the majority of the cases in the

Baroclinic Zone: Southwesterly Thermal Wind subset (20 of 29 cases) and the Cold Pool category (25 of 36 cases) are AR-influenced.

ARs appear to be less of a characteristic ingredient for the Baroclinic Zone: Westerly Thermal Wind subset than for the other two lower-tropospheric cold air patterns. The Baroclinic Zone: Westerly Thermal Wind subset has an AR fraction of 47.5%, which indicates that ARs are often present during snowstorms in this subset. However, the ARs present during these snowstorms do not appear to play a large role in transporting moisture into the Northeast domain, since the ARs observed during all case days are concentrated over the western North Atlantic Ocean and are infrequent over the Northeast domain. Additionally, a low number of cases (5 of 20 cases) in the Baroclinic Zone: Westerly Thermal Wind subset are AR-influenced.

The composite analysis reveals various atmospheric flow patterns associated with the different lower-tropospheric cold air patterns of major transition season Northeast snowstorms. Conceptual models (Figs. 5.1a–c) highlight the variations in the atmospheric flow patterns for each of the lower-tropospheric cold air patterns at t_0, which represents a time of heavy precipitation (see section 2.5.1 for details). The Baroclinic Zone: Southwesterly Thermal Wind subset features a northeastward-moving surface cyclone and a southeastward-moving surface anticyclone located to the west of the surface cyclone at t_0. While the surface anticyclone moves southeastward, it exhibits a ridge of high pressure that extends toward the north of the surface cyclone (Fig. 5.1a). While the surface cyclone moves northeastward, it is located within the equatorward entrance region of a 250-hPa jet streak (Fig. 5.1a). Also while the surface cyclone moves northeastward, it features a northeastward advancing plume of PWAT collocated with IVT directed toward the northeast (Fig. 5.1a). Low-level flow, established by the juxtaposition of the surface cyclone and a surface anticyclone centered over the Atlantic Ocean, aids in advecting the plume of PWAT northeastward (Fig. 5.1a). At t_0, the surface cyclone is associated with a high-amplitude 500-hPa trough (Fig. 5.1a). In the northwest sector of the surface cyclone at t_0, Q-vector forcing for ascent is collocated with a band of frontogenesis, which stretches from the southwest to the northeast (Fig. 5.1a). Also in the northwest sector of the surface cyclone at t_0, lower-tropospheric cold air is established (Fig. 5.1a). Cooling due to ascent and horizontal cold air advection, by both the total wind and the ageostrophic wind, reinforces this cold air (shown in Figs. 4.4b and 4.5a,b).

The Baroclinic Zone: Westerly Thermal Wind subset features an eastward-moving surface cyclone and surface anticyclone. The surface anticyclone is located to the northeast of the surface cyclone before t_0 (shown in Figs. 4.8a,c). At t_0, high surface pressure is evident toward the north of the surface cyclone. As the surface cyclone moves eastward, low-level flow associated with the surface cyclone and enhanced by a surface anticyclone over the western North Atlantic Ocean advects a plume of PWAT poleward, which is collocated with IVT directed toward the east-northeast (Fig. 5.1b). At upper levels, the surface cyclone is associated with a low-amplitude 500-hPa trough at t_0 (Fig. 5.1b). Also at t_0, a signature of jet coupling at 250 hPa is evident over the surface cyclone (Fig. 5.1b). Toward the north and northwest of the surface cyclone at t_0, Q-vector forcing for ascent occurs and overlaps with a band of frontogenesis, which stretches from west to east (Fig. 5.1b). Cold air in the lower troposphere is established in the northern portion of the snowstorm as indicated by the southward extent of the 1290 m 1000–850-hPa thickness contour (Fig. 5.1b). The cold air is reinforced by cooling due to ascent and horizontal cold air advection by both the total wind and the ageostrophic wind (shown in Figs. 4.10b and 4.11a,b).

The Cold Pool category features a northeastward-moving surface cyclone and an eastward-moving surface anticyclone, which is located to the north of the surface cyclone. At upper levels, this surface cyclone is associated with a moderate-amplitude 500-hPa trough at t_0 (Fig. 5.1c). Also at upper levels, this surface cyclone is located toward the poleward exit region of a jet streak at 250 hPa (Fig. 5.1c). As the surface cyclone moves northeast, it features a broad area of northeastward advancing PWAT that overlaps with IVT that transitions from indicating northeastward moisture transport in the southern portion of the surface cyclone to northwestward moisture transport in the northern portion of the surface cyclone (Fig. 5.1c). Also in the northern portion of the surface cyclone, Q-vector forcing for ascent is apparent over a lower-tropospheric cold pool, and an area of frontogenesis located to the southeast of the lower-tropospheric cold pool coincides with the Q-vector forcing for ascent (Fig. 5.1c). Lower-tropospheric cold air is evident in the form of a narrow thermal trough with 1000–850-hPa thickness values ≤ 1290 m toward the north of the surface cyclone (Figs. 5.1c and 5.2a). Within this narrow thermal trough, a lower-tropospheric cold pool is apparent in regions that display cooling due to ascent, horizontal cold air advection by the total wind (Fig. 5.2a), and horizontal cold air advection by the ageostrophic wind (Fig. 5.2b). Signatures characteristic of diabatic cooling (i.e., moistening and cooling) are apparent within the lower-tropospheric cold pool, in both composite maps and composite soundings in section 4.3. These signatures indicate that diabatic cooling is likely important to the development of the lower-tropospheric cold pool. The lower-tropospheric cold pool occurs beneath the cross-hair signature, a signature of heavy snowfall (Cobb and Waldstreicher 2005), and frontogenesis overspreads the lower-tropospheric cold pool (Fig. 5.2b).

5.2 Discussion

5.2.1 Climatology

The climatology of major transition season Northeast snowstorms grouped by temporal characteristics is consistent with a climatology produced by Kocin and Uccellini (2004b, pp. 10–39) (as discussed in section 3.1) and a climatology produced by Changnon et al. (2006). Specifically, a latitudinal gradient pertaining to snowfall is evident in all three climatologies. In this study, the number of cases with heavy snowfall generally increases with increasing latitude in the Northeast domain for the months of March, April, and November. Kocin and Uccellini (2004b, pp. 10–39) generally analyzed increasing snowfall values as latitude increased when they spatially analyzed mean seasonal snowfall in the Northeast during 1961–1990, and Changnon et al. (2006) generally analyzed an increase in the annual average number of snowstorms as latitude increases east of the Rocky Mountains during 1901–2001 (refer to section 1.2.1 for further details regarding their analysis). The latitudinal gradient analyzed in this study, as well as in the studies of Kocin and Uccellini (2004b, pp. 10–39) and Changnon et al. (2006), indicates that the ingredients of snowstorms (i.e., cold air, moisture, and lift) (Kocin and Uccellini 2004b, pp. 4–6) overlap at higher latitudes more frequently than at lower latitudes in the Northeast. The frequent overlap of the snowstorm ingredients at higher latitudes in the Northeast is likely attributable to greater availability of cold air at higher latitudes relative to lower latitudes, since higher latitudes are climatologically colder than lower latitudes.

Two of the three ingredients of snowstorms (Kocin and Uccellini 2004b, pp. 4–6) served as the basis for two foci in this study: moisture transport occurring within ARs and lower-tropospheric cold air. Focusing on ARs, to the author's knowledge, this study is the first to document ARs during major transition season Northeast snowstorms from a climatological standpoint. Results from the documentation of the ARs support the following proposal made by Lavers and Villarini (2015). Lavers and Villarini (2015) calculated ratios of AR-contributed precipitation to total precipitation for each month in the central and eastern U.S. during 1979–2012, and they proposed that ARs during snowstorms led to high values of the AR-contributed precipitation to total precipitation ratio in the Northeast. Although this study focuses on major transition season Northeast snowstorms, it is shown that ARs are frequent during snowstorms that impact the Northeast as indicated by monthly AR fractions over 50%.

Focusing on lower-tropospheric cold air, months that are climatologically colder than other months in the transition seasons feature more snowstorms. The climatologically colder months are March and November, and these months feature two thirds of their monthly totals classified in the Baroclinic Zone category. Composites of the two subsets in this category indicate that cold air is abundant to the north of the surface cyclone centers, where mean temperatures of the 1000–850-hPa layer decrease rapidly to temperatures well-below freezing. Lower-tropospheric cold air is found to be more of a limiting ingredient in April than in March and November. Approximately two thirds of the snowstorms in April are in the Cold Pool category, and composites of the Cold Pool category indicate warmer mean temperatures of the 1000–850-hPa layer to the north of the surface cyclone center relative to either subset in the Baroclinic Zone category. Composites of the Cold Pool category also indicate a less rapid decrease in the mean temperature of the 1000–850-hPa layer to the north of the surface cyclone center relative to either subset in the Baroclinic Zone category.

Focusing on ARs and lower-tropospheric cold pools in the Cold Pool category, this study documents spatial overlap between these two features over eastern New York and New England at t_0. In this area, high values of AR axis density overlap high values of lower-tropospheric cold pool occurrence. Moreover, the core of high AR axis density is directed inland toward the area where lower-tropospheric cold pools occur most frequently, suggesting that moisture transport from ARs is directed into the area. Additionally, eastern New York and New England feature a concentration of high numbers of cases with heavy snowfall, confirming that all three ingredients of snowstorms (Kocin and Uccellini 2004b, pp. 4–6) frequently overlap in the area.

5.2.2 Composite Analysis

Synoptic-scale features in the composite analysis of the three lower-tropospheric cold air patterns associated with major transition season Northeast snowstorms reveal similarities to synoptic-scale features common among 30 snowstorms that impact the Northeast that were analyzed by Kocin and Uccellini (2004b, pp. 79–124). These common synoptic-scale features include: 1) antecedent large-scale features at 500 hPa (a ridge over western North America and a trough over eastern Canada), 2) an amplifying trough associated with the snowstorm, 3) a jet streak at the base of the trough over eastern Canada, 4) dynamic coupling of jet streaks over the snowstorm, and 5) surface anticyclone position and evolution. The composites of the subsets in the Baroclinic Zone category reveal several additional similarities to the 30 snowstorms analyzed by Kocin and Uccellini (2004b, pp. 79–124), which include: 1) areas of confluence at 500 hPa above surface anticyclones, and 2) thermally direct ageostrophic circulations that advect cold air toward the snowstorm and that are associated with jet streaks toward the northeast of the snowstorms.

Although many similar synoptic-scale features are identified within the composites of the three lower-tropospheric cold air patterns, the synoptic-scale features vary among the composites of the lower-tropospheric cold air patterns. The conceptual models display the varying features and show that major transition season Northeast snowstorms exhibit different atmospheric flow patterns (Figs. 5.1a–c). The varying features in the conceptual models relate to: 1) amplitudes of the 500-hPa troughs associated with the surface cyclones, 2) positions of prominent 250-hPa jet streaks relative to the surface cyclones, 3) direction of IVT in the vicinity of the surface cyclones, 4) positions of the surface anticyclones relative to the surface cyclones, 5) southward extensions of lower-tropospheric cold air (represented by 1290 m 1000–850-hPa thickness contours), and 6) configurations of frontogenesis regions. Differences in the composites not illustrated in the conceptual models relate to: 1) surface cyclone track, 2) surface anticyclone position and evolution, 3) ARs and their associated moisture transport, and 4) lower-tropospheric cold air.

ARs are identified in composite IVT fields for the three lower-tropospheric cold air patterns. These ARs, specifically the ARs shown in Figs. 4.3f, 4.9f, and 4.15h, feature a common signature pertaining to moisture transport: IVT vectors along the ARs axes are directed into areas of ascent associated with the snowstorms, which suggests that the ARs transport moisture into the snowstorms. In considering ARs in the composites, it is important to note that AR axes objectively identified in the composites do not represent the mean position of the ARs axes at their times of identification; rather identified AR axes indicate that the composite IVT field meets the objective thresholds of the algorithm that identifies ARs. Identification of ARs in the composite IVT field highlights the prominence of ARs in the composites members; maximum IVT values are used in the algorithm that identifies ARs, and composite IVT fields tend to exhibit lower maximum values than the composite members used to calculate the composite IVT fields.

Focusing on t_0, ARs are identified in the two subsets of the Baroclinic Zone category but not in the Cold Pool category. This difference in identification may be attributable to the difference in compositing methods between the two categories (see section 2.5.1 for additional details). In constructing composites for the Baroclinic Zone category, surface cyclone centers serve as a composite center, allowing for the spatial alignment of the eastern portions of the surface cyclones, which is the general location of ARs. In constructing composites for the Cold Pool category, lower-tropospheric cold pools serve as a composite center, so the eastern portions of the surface cyclones are not as likely to be spatially aligned. Although ARs are not identified in the composites of the three lower-tropospheric cold air patterns at t_0, AR fractions at t_0 indicate that ARs are frequent for the three lower-tropospheric cold air patterns at t_0. For each lower-tropospheric cold air pattern, the composite IVT field reveals a different moisture transport direction in the eastern portion of the surface cyclone (Figs. 5.1a–c), and this direction of moisture transport closely aligns with the core of high AR axis density at t_0. The different moisture transport directions and the different configurations of the cores of high AR axis density for the lower-tropospheric cold air patterns may be related to different configurations of jet streaks at 250-hPa, which is suggested based on the results of Payne and Magnusdottir (2016). Payne and Magnusdottir (2016) investigated ARs that made landfall over the western North American coast and noted that these ARs were associated with 200-hPa potential vorticity and 200-hPa jets. For example, they noted associations between strengths of ARs and strengths of 200-hPa jets, and also between positions of ARs and positions of 200-hPa jets when they created composites with various groups of ARs.

Lower-tropospheric cold air is more prevalent in both subsets of the Baroclinic Zone category than in the Cold Pool category. For example, temperatures at 850 hPa are colder and more anomalously cold over eastern North America in both subsets of the Baroclinic Zone category than in the Cold Pool category from t_0 – 48 h to t_0. 1000–850-hPa thickness fields reveal lower thickness values in southeastern Canada, indicative of colder air throughout the 1000–850-hPa layer, in both subsets of the Baroclinic Zone category compared to the Cold pool category at t_0. Additionally, stronger signatures of cooling due to ascent, and horizontal cold air advection by both the total wind and the ageostrophic wind, are evident in areas of heavy snowfall at t_0 in both subsets of the Baroclinic Zone category compared to the Cold Pool category. Although cold air is less prevalent in the Cold Pool category than in the subsets of the Baroclinic Zone category, it is suggested that the snowstorms in the Cold Pool category produce lower-tropospheric cold air through diabatic cooling in areas of heavy snowfall.

5.2.3 Applications of Research to Operational Forecasting

In this study, operationally relevant fields (e.g., 1000–850-hPa thickness, Q-vectors) are utilized in the analysis of major transition season Northeast snowstorms in order to facilitate the transition of research to operational forecasting. The 1000–850-hPa thickness field was used to classify major transition season Northeast snowstorms. The classification of snowstorms using this field can generally be performed visually, which can allow forecasters to quickly classify a major transition season Northeast snowstorm into one of the three lower-tropospheric cold air patterns. Composite analyses (chapter 4) and case studies (not shown) confirm the effectiveness of the 1000–850-hPa field in classifying major transition season Northeast snowstorms, since the composite analyses and case studies illustrate that the lower-tropospheric cold air patterns reveal different planetary-to-synoptic-scale and synoptic-to-mesoscale atmospheric flow patterns. The planetary-to-synoptic-scale and synoptic-to-mesoscale atmospheric flow patterns for each lower-tropospheric cold air pattern are illustrated in the conceptual models shown in Fig. 5.1. Additional conceptual models are shown in Fig. 5.2 for the Cold Pool category in order to illustrate synoptic-to-mesoscale flow patterns surrounding a lower-tropospheric cold pool. The case studies (not shown), which are illustrative examples of the composite analyses, have also been prepared to accompany the conceptual models for use in operational forecasting. At the time of this writing, the conceptual models and the case studies are being integrated into the NWS Virtual Laboratory tool.

5.3 Suggestions for Future Work

Future work could expand upon the AR climatology during major transition season Northeast snowstorms in this study to include either: 1) ARs during major winter season snowstorms in the Northeast, or 2) all ARs that occur during 1983–present over the eastern U.S. and the western North Atlantic Ocean. An expanded AR climatology could be used to investigate climatological characteristics of ARs, such as in Mundhenk et al. (2016), who did so for ARs occurring over the North Pacific Ocean. The expanded AR climatology could also be used to investigate whether more precipitation (liquid or solid) or flooding occurs when an AR is present than when an AR is absent. Methodologies of other studies with a similar focus (e.g., Ralph et al. 2006; Lavers and Villarini 2013; Mahoney et al. 2016) could be utilized for this investigation. This investigation could also examine whether different AR axis configurations tend to yield different amounts of precipitation.

The expanded AR climatology could also be utilized to examine the dynamics associated with landfalling ARs, as was done by Payne and Magnusdottir (2016) for western North America. Payne and Magnusdottir (2016) noted that landfalling ARs were associated with 200-hPa potential vorticity and 200-hPa jets. For example, they noted associations between strengths of ARs and strengths of 200-hPa jets, and also between positions of ARs and positions of 200-hPa jets when they created composites with various groups of ARs. Results from this thesis motivate the examination of the dynamics of landfalling ARs along the Northeast. Also, results from this thesis suggest considering different configurations of landfalling ARs (e.g., linear or cyclonically curved) when examining the dynamics associated with landfalling ARs. Results from chapter 3 of this study reveal different configurations of AR axes in the climatology when snowstorms were grouped by lower-tropospheric cold air pattern, and results from chapter 4 of this study show different configurations of 250-hPa jet streaks in the composites of the lower-tropospheric cold air patterns.

Using this study as a starting point, future research on major transition season Northeast snowstorms could investigate whether relationships exist between various teleconnection indices (e.g., North Atlantic Oscillation and El Niño–Southern Oscillation) and ARs or lower-tropospheric cold air patterns. For example, future research could investigate whether or not certain phases of a teleconnection index tend to favor the occurrence of snowstorms for one lower-tropospheric cold air pattern relative to the others. Also using this study as a starting point, future research could focus on a time period when radar imagery is available in order to investigate whether there are relationships between lower-tropospheric cold pools and snowbands identified from the radar imagery, such as the snowband types identified by Kenyon (2013).

Model simulations could be conducted to further explore the development of lower-tropospheric cold pools motivated by results in chapter 3 of this study, where it was shown that many lower-tropospheric cold pools initially occur along and in the lee of the Appalachian Mountains. A model simulation that includes terrain and a parallel model simulation that excludes terrain could be performed for a snowstorm that features a lower-tropospheric cold pool along or in the lee of the Appalachian Mountains. The two simulations could be compared to evaluate the influence of terrain on lower-tropospheric cold pool development. Model simulations could also be conducted to investigate if lower-tropospheric cold pools enhance snowfall by determining if the lower-tropospheric cold pools occurring during snowstorms act similar to the ones present during severe convective weather, which can induce lift on their boundaries (Engerer et al. 2008).

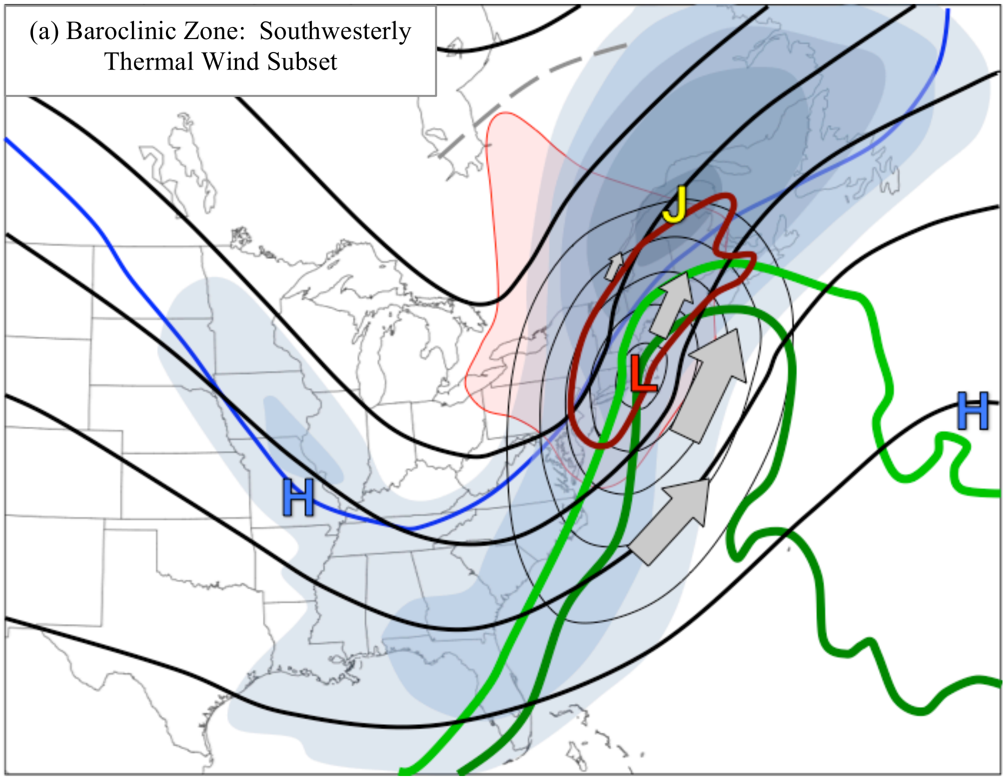

(a) Baroclinic Zone: Southwesterly Thermal Wind Subset

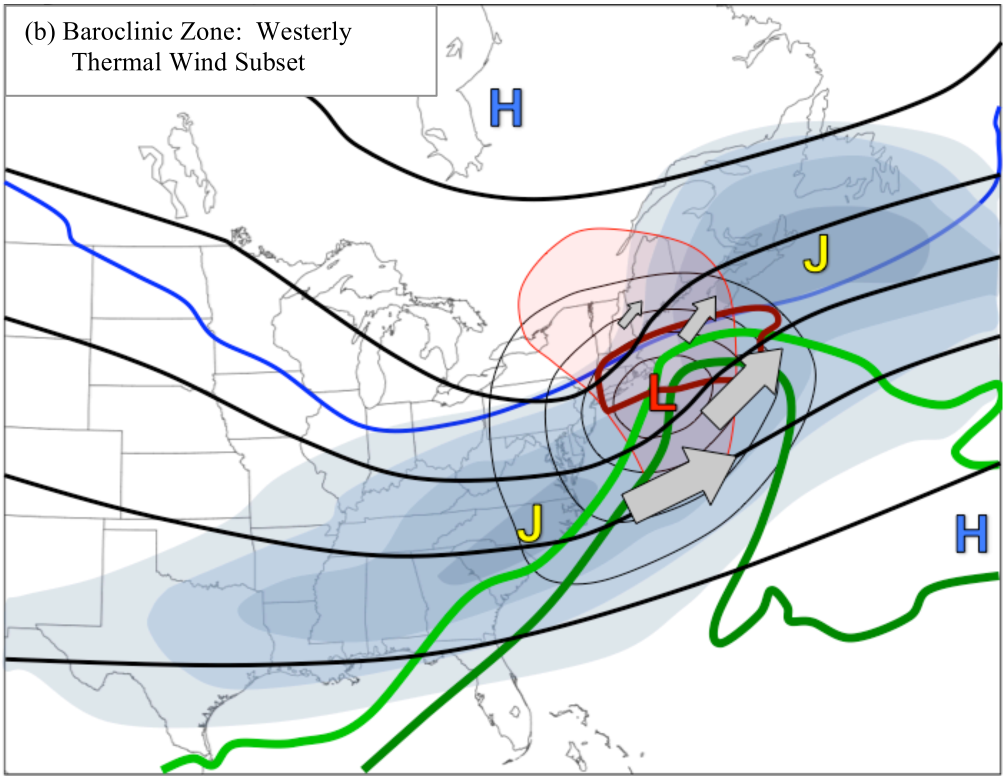

(b) Baroclinic Zone: Westerly Thermal Wind Subset

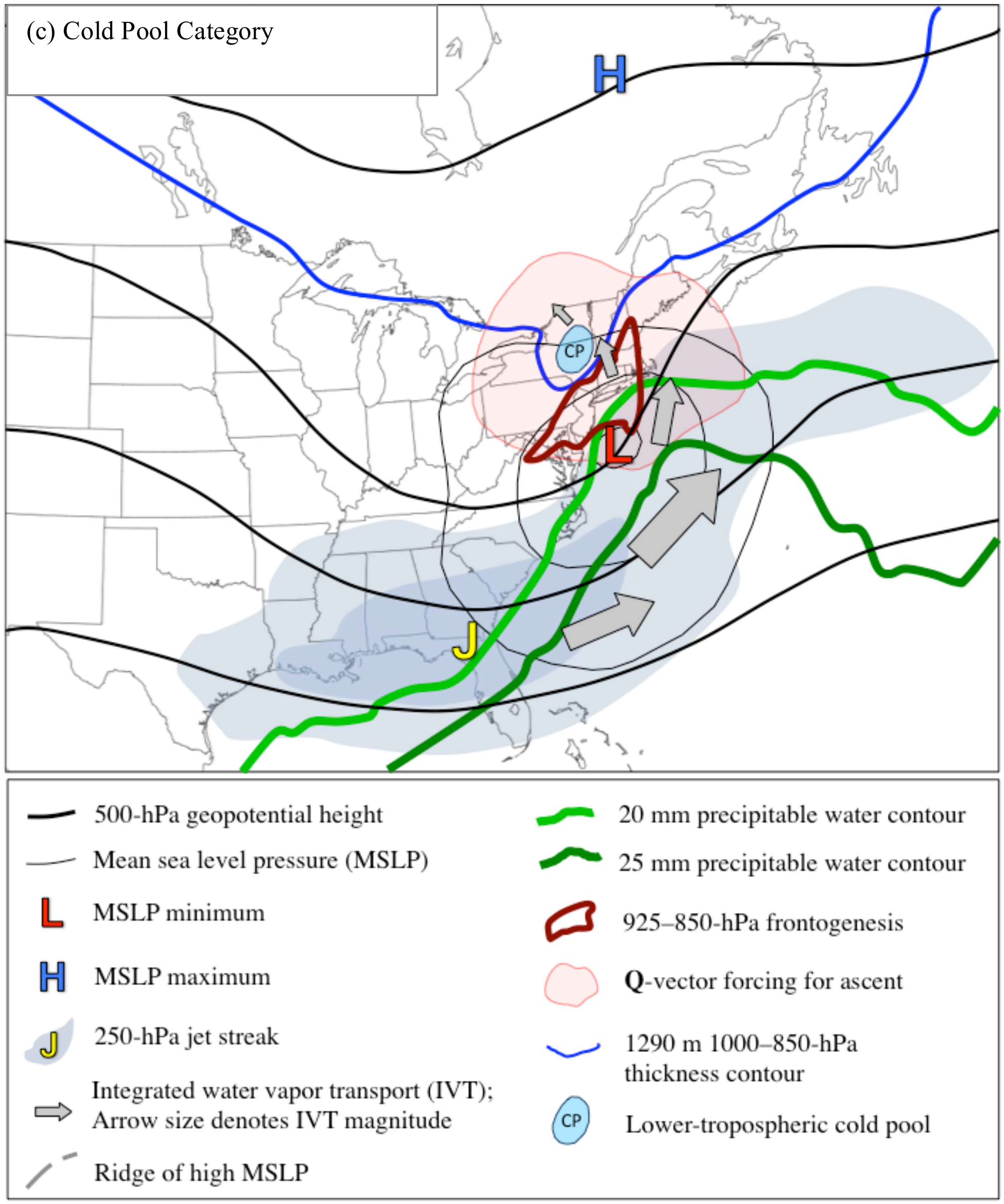

Fig. 5.1 Conceptual models summarizing planetary-to-synoptic-scale and synoptic-to-mesoscale atmospheric flow patterns at t_0 for (a) the Baroclinic Zone: Southwesterly Thermal Wind subset, (b) the Baroclinic Zone: Westerly Thermal Wind subset, and (c) the Cold Pool category. The background maps in the conceptual models are for reference only.

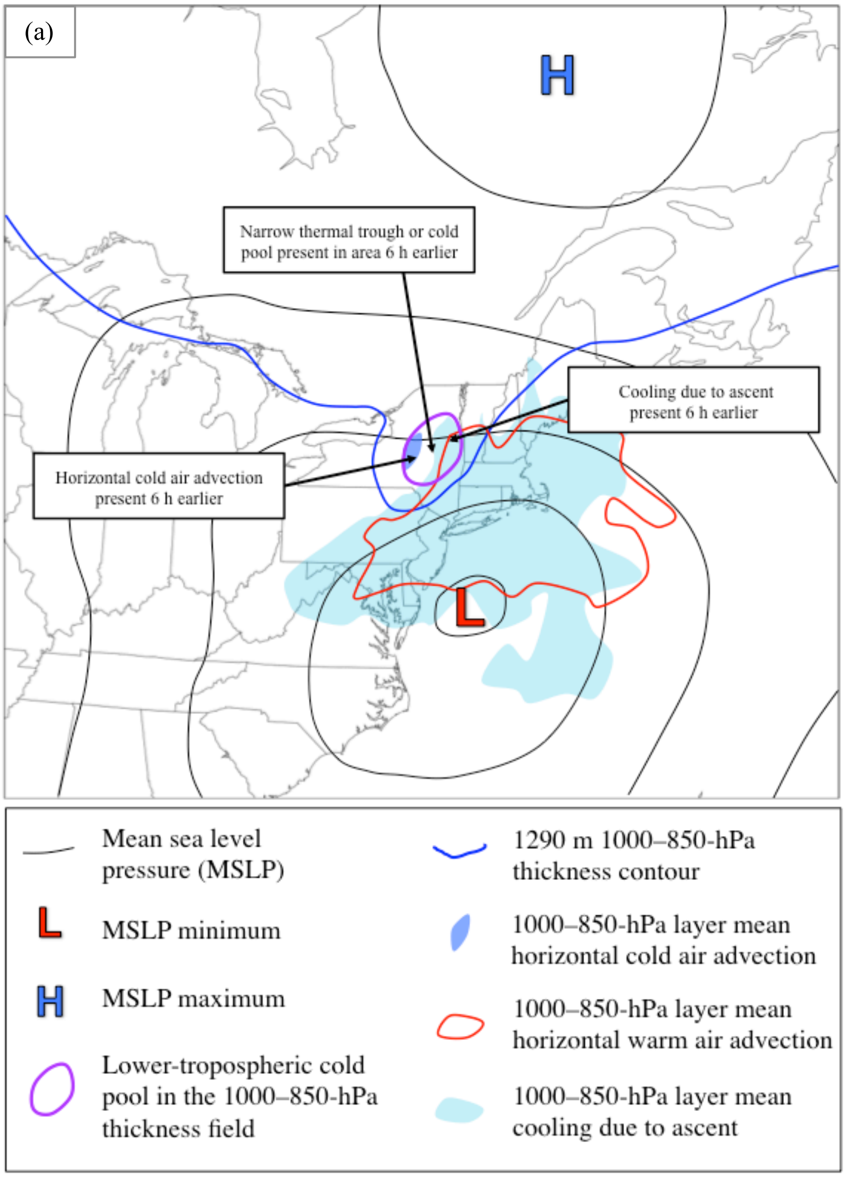

Narrow thermal trough or cold pool present in area 6 h earlier

Cooling due to ascent present 6 h earlier

Horizontal cold air advection present 6 h earlier

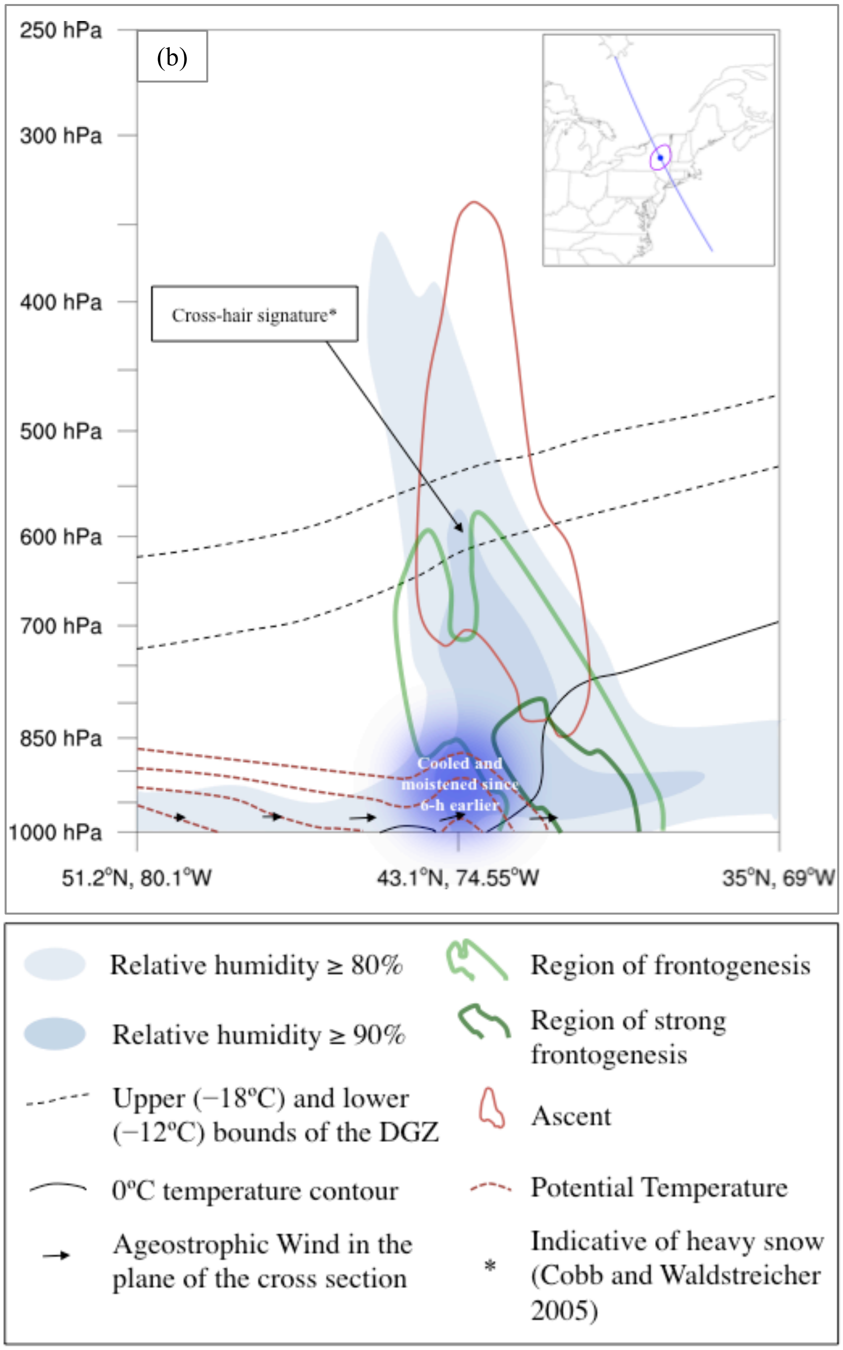

Fig. 5.2 Conceptual models for the Cold Pool category summarizing synoptic-to-mesoscale atmospheric flow patterns surrounding a lower-tropospheric tropospheric cold pool at t_0 for (a) the 1000–850-hPa layer and (b) a cross section through the cold pool. The cross section corresponds to the blue line in the inset map, and the center tick mark of the cross section corresponds to the solid blue circle in the inset map. The inset map includes the lower-tropospheric cold pool (purple line) from Fig. 5.2a. The background maps in the conceptual models are for reference only.

REFERENCES

Bao, J-W., S. A. Michelson, P. J. Neiman, F. M. Ralph, and J. M. Wilczak, 2006: Interpretation of enhanced integrated water vapor bands associated with extratropical cyclones: Their formation and connection to tropical moisture. *Mon. Wea. Rev.,* **134,** 1063–1080.

Baxter, M. A., C. E. Graves, and J. T. Moore, 2005: A climatology of snow-to-liquid ratio for the contiguous United States. *Wea. Forecasting,* **20,** 729–744.

Bell, G. D., and L. F. Bosart, 1989: The large-scale atmospheric structures accompanying New England coastal frontogenesis and associated North American east coast cyclogenesis. *Quart. J. Roy. Meteor. Soc.,* **115,** 1133–1146.

Bosart, L. F., and F. Sanders, 1991: An early-season coastal storm: Conceptual success and model failure. *Mon. Wea. Rev.,* **119,** 2831–2851.

—, C. J. Vaudo, and J. H. Helsdon Jr., 1972: Coastal frontogenesis. *J. Appl. Meteor.,* **11,** 1236–1258.

Brandes, E. A., and J. Spar, 1971: A search for necessary conditions for heavy snow on the East Coast. *J. Appl. Meteor.,* **10,** 397–409.

Branick, M. L., 1997: A climatology of significant winter-type weather events in the contiguous United States, 1982–94. *Wea. Forecasting,* **12,** 193–207.

Castellano, C. M., 2012: Synoptic and mesoscale aspects of ice storms in the northeastern U.S. M.S. thesis, Dept. of Atmospheric and Environmental Sciences, University at Albany, State University of New York, 134 pp.

Carlson, T. N., 1980: Airflow through midlatitude cyclones and the comma cloud pattern. *Mon. Wea. Rev.,* **108,** 1498–1509.

Changnon, S. A., D. Changnon, and T. R. Karl, 2006: Temporal and spatial characteristics of snowstorms in the contiguous United States. *J. Appl. Meteor. Climatol.,* **45,** 1141–1155.

Cobb, D. K., Jr., and J. S. Waldstreicher, 2005: A simple physically based snowfall algorithm. Preprints, 21st Conf. on Weather Analysis and Forecasting/17th Conf. on Numerical Weather Prediction, Washington, DC, Amer. Meteor. Soc., 2A.2. [Available online at https://ams.confex.com/ams/WAFNWP34BC/techprogram/paper_94815.htm].

Colucci, S. J., 1976: Winter cyclone frequencies over the eastern United States and adjacent western Atlantic, 1963–1973. *Bull. Amer. Meteor. Soc.,* **57,** 548–553.

Dacre, H. F., P. A. Clark, O. Martinez-Alvarado, M. A. Stringer, and D. A. Lavers, 2015: How do atmospheric rivers form? *Bull. Amer. Meteor. Soc.,* **96,** 1243–1255.

Danielson, J. J., and D. B. Gesch, 2011: Global multi-resolution terrain elevation data 2010 (GMTED2010). U.S. Geological Survey Open-File Report 2011–1073, 26 p.

DeVoir, G., 2002: A quick review of snow microphysics and its relation to heavy snow forecasting. Preprints, *NWS CTP Winter Weather Workshop,* National Weather Service, 1–27. [Available online at www.weather.gov/media/ctp/HISA/SnowMicroPhysics.ppt.]

Draxler, R. R., and G. D. Hess, 1998: An overview of the HYSPLIT4 modeling system for trajectories, dispersion, and deposition. *Aust. Meteor. Mag.,* **47,** 295–308.

Engerer, N. A., D. J. Stensrud, and M. C. Coniglio, 2008: Surface characteristics of observed cold pools. *Mon. Wea. Rev.,* **136,** 4839–4849.

Evans, M., 2006: An analysis of a frontogenetically forced early-spring snowstorm. *Bull. Amer. Meteor. Soc.,* **87,** 27–32.

Ganetis, S. A., and B. A. Colle, 2015: The thermodynamic and microphysical evolution of an intense snowband during the northeast U.S. blizzard of 8–9 February 2013. *Mon. Wea. Rev.,* **143,** 4104–4125.

Gedzelman, S. D., and E. Lewis, 1990: Warm snowstorms: A forecasters dilemma. *Weatherwise,* **43,** 265–270.

Gimeno, L., R. Nieto, M. Vázquez, and D. A. Lavers, 2014: Atmospheric rivers: A mini-review. *Frontiers in Earth Science,* **2,** 1–6, 10.3389/feart.2014.00002.

Halverson, J. B., and T. D. Rabenhorst, 2010: Mega-snow in the megalopolis: The mid-Atlantic's blockbuster winter of 2009–2010. *Weatherwise,* **63,** 16–23.

Harrington, J. A., Jr., R. S. Cerveny, and K. F. Dewey, 1987: A climatology of mean monthly snowfall for the conterminous United States: Temporal and spatial patterns. *J. Climate Appl. Meteor.,* **26,** 897–912.

Homan, J., and L. W. Uccellini, 1987: Winter forecast problems associated with light to moderate snow events in the mid-Atlantic states on 14 and 22 February 1986. *Wea. Forecasting,* **2,** 206–228.

Kain, J. S., S. M. Goss, and M. E. Baldwin, 2000: The melting effect as a factor in precipitation-type forecasting. *Wea. Forecasting,* **15,** 700–714.

Kenyon, J. S., 2013: The motion of mesoscale snowbands in northeast U.S. winter storms. M.S. thesis, Dept. of Atmospheric and Environmental Sciences, University at Albany, State University of New York, 122 pp.

Kocin, P. J., and L. W. Uccellini, 2004a: A snowfall impact scale derived from Northeast storm snowfall distributions. *Bull. Amer. Meteor. Soc.,* **85,** 177–194.

——, and ——, 2004b: *Northeast Snowstorms. (Volume I: Overview, Volume II: The Cases). Meteor. Monogr.*, No. 54, Amer. Meteor. Soc., 818 pp.

——, P. N. Schumacher, R. F. Morales Jr., and L. W. Uccellini, 1995: Overview of the 12–14 March 1993 superstorm. *Bull. Amer. Meteor. Soc.,* **76,** 165–182.

Lackmann, G. M., L. F. Bosart, and D. Keyser, 1996: Planetary- and synoptic-scale characteristics of explosive wintertime cyclogenesis over the western North Atlantic Ocean. *Mon. Wea. Rev.,* **124,** 2672–2702.

——, K. Keeter, L. G. Lee, and M. B. Ek, 2002: Model representation of freezing and melting precipitation: Implications for winter weather forecasting. *Wea. Forecasting,* **17,** 1016–1033.

Lavers, D. A., and G. Villarini, 2013. Atmospheric rivers and flooding over the central United States. *J. Clim.,* **26,** 7829–7836.

——, and G. Villarini, 2015: The contribution of atmospheric rivers to precipitation in Europe and the United States. *J. Hydro*., **522,** 382–390.

Maglaras, G. J., J. S. Waldstreicher, P. J. Kocin, A. F. Gigi, and R. A. Marine, 1995: Winter weather forecasting throughout the eastern United States. Part I: An overview. *Wea. Forecasting,* **10,** 5–20.

Mahoney, K., D. L. Jackson, P. Neiman, M. Hughes, L. Darby, G. Wick, A. White, E. Sukovich, and R. Cifelli, 2016: Understanding the role of atmospheric rivers in heavy precipitation in the southeast United States. *Mon. Wea. Rev.,* **144,** 1617–1632.

Market, P. S., R. W. Przybylinski, and S. M. Rochette, 2006: The role of sublimational cooling in a late-season Midwestern snow event. *Wea. Forecasting,* **21,** 364–382.

Martin, J. E., 1999: Quasigeostrophic forcing of ascent in the occluded sector of cyclones and the trowal airstream. *Mon. Wea. Rev.,* **127,** 70–88.

McNulty, R. P., 1988: Winter precipitation type. CR Technical Attachment 88–4. DOC/NOAA/NWS central Region, Kansas City, MO, 9 pp.

Menne, M., I. Durre, R. Vose, B. Gleason, and T. Houston, 2012: An Overview of the Global Historical Climatology Network-Daily Database. *J. Atmos. Oceanic Technol.,* **29,** 897–910.

Moore, B. J., P. J. Neiman, F. M. Ralph, and F. E. Barthold, 2012: Physical processes associated with heavy flooding rainfall in Nashville, Tennessee, and vicinity during 1–2 May 2010: The role of an atmospheric river and mesoscale convective systems. *Mon. Wea. Rev.,* **140,** 358–378.

Mote, T. L., D. W. Gamble, S. J. Underwood, and M. L. Bentley, 1997: Synoptic-scale features common to heavy snowstorms in the southeast United States. *Wea. Forecasting,* **12,** 5–23.

Mullens, E. D., L. M. Leslie, and P. J. Lamb, 2016: Synoptic pattern analysis and climatology of ice and snowstorms in the southern Great Plains, 1993–2011. *Wea. Forecasting,* **31,** 1109–1136.

Mundhenk, B. D., E. A. Barnes, and E. D. Maloney, 2016: All-season climatology and variability of atmospheric river frequencies over the North Pacific. *J. Climate,* **29,** 4885–4903.

NCEI, 1997a: Storm Data. Vol. 39, No. 3, 249 pp.

—–, 1997b: Storm Data. Vol. 30, No. 4, 211 pp.

—–, 2011: Storm Data. Vol. 53, No. 4, 146 pp.

Neiman, P. J., F. M. Ralph, G. A. Wick, J. D. Lundquist, and M. D. Dettinger, 2008a: Meteorological characteristics and overland precipitation impacts of atmospheric rivers affecting the west coast of North America based on eight years of SSM/I satellite Observations. *J. Hydrometeor.,* **9,** 22–47.

—–, —–, —–, Y.-H. Kuo, T.-K. Wee, Z. Ma, G. H. Taylor, and M. D. Dettinger, 2008b: Diagnosis of an intense atmospheric river impacting the Pacific Northwest: Storm summary and offshore vertical structure observed with COSMIC satellite retrievals. *Mon. Wea. Rev.,* **136,** 4398–4420.

Nicosia, D. J., and R. H. Grumm, 1999: Mesoscale band formation in three major northeastern United States snowstorms. *Wea. Forecasting,* **14,** 346–368.

Novak, D. R., L. F. Bosart, D. Keyser, and J. S. Waldstreicher, 2004: An observational study of cold season–banded precipitation in northeast U.S. cyclones. *Wea. Forecasting,* **19,** 993–1010.

Pasch, R. J., E. S. Blake, H. D. Cobb III, and D. P. Roberts, 2006: Tropical Cyclone Report: Hurricane Wilma, 15–25 October 2005. National Hurricane Center Rep., 27 pp. [Available online at http://www.nhc.noaa.gov/data/tcr/AL252005_Wilma.pdf.]

Payne, A. E., and G. Magnusdottir, 2014: Dynamics of landfalling atmospheric rivers over the North Pacific in 30 years of MERRA reanalysis. *J. Climate,* **27,** 7133–7150.

Penn, S., 1957: The prediction of snow vs. rain. Forecasting Guide #2, U.S. Weather Bureau, 29 pp.

QGIS Development Team, 2015: QGIS Geographic Information System. Open Source Geospatial Foundation Project. [Available online at http://www.qgis.org/.]

Ralph, F. M., P. J. Neiman, and G. A. Wick, 2004: Satellite and CALJET aircraft observations of atmospheric rivers over the eastern North Pacific Ocean during the winter of 1997/98. *Mon. Wea. Rev.,* **132,** 1721–1745.

—, —, G. A. Wick, S. I. Gutman, M. D. Dettinger, D. R. Cayan, and A. B. White, 2006: Flooding on California's Russian River: The role of atmospheric rivers. *Geophys. Res. Lett.,* **33,** L13801.

Ramos, A. M., R. Nieto, R. Tomé, L. Gimeno, R. M. Trigo, M. L. R. Liberato, and D. A. Lavers, 2016: Atmospheric rivers moisture sources from a Lagrangian perspective. *Earth Syst. Dynam.,* **7,** 2, 371–384.

Reitan, C. H., 1974: Frequencies of cyclones and cyclogenesis for North America, 1951–1970. *Mon. Wea. Rev.,* **102,** 861–868.

Richwein, B. A., 1980: The damming effect of the southern Appalachians. *Natl. Wea. Dig.,* **5,** 2–12.

Roebber, P. J., 1984: Statistical analysis and updated climatology of explosive cyclones. *Mon. Wea. Rev.,* **112,** 1577–1589.

—, S. L. Bruening, D. M. Schultz, and J. V. Cortinas Jr., 2003: Improving snowfall forecasting by diagnosing snow density. *Wea. Forecasting,* **18,** 264–287.

Rutz, J. J., W. J. Steenburgh, and F. M. Ralph, 2014: Climatological characteristics of atmospheric rivers and their inland penetration over the western United States. *Mon. Wea. Rev.,* **142,** 905–921.

Saha, S., and Coauthors, 2010: The NCEP Climate Forecast System Reanalysis. *Bull. Amer. Meteor. Soc.,* **91,** 1015–1057.

Sanders, F., and J. R. Gaykum, 1980: Synoptic-dynamic climatology of the "bomb." *Mon. Wea. Rev.,* **108,** 1589–1606.

Schmocker, G. K., 2008: Forecasting winter precipitation type. Preprints, *Winter Weather Workshop 2008;* St. Louis, MO, National Weather Service, 1–70. [Available online at https://www.weather.gov/lsx/winterwxworkshop08.]

Schultz, D. M., 2001: Reexamining the cold conveyor belt. *Mon. Wea. Rev.,* **129,** 2205–2225.

Sodemann, H., and A. Stohl, 2013: Moisture Origin and Meridional Transport in Atmospheric Rivers and Their Association with Multiple Cyclones. *Mon. Wea. Rev.,* **141,** 2850–2868.

Squires, M. F., J. H. Lawrimore, R. R. Heim Jr., D. A. Robinson, M. R. Gerbush, and T. W. Estilow, 2014: The regional snowfall index. *Bull. Amer. Meteor. Soc.,* **95,** 1835–1848.

Sutcliffe, R. C., and A. G. Forsdyke, 1950: The theory and use of upper air thickness patterns in forecasting. *Quart. J. Roy. Meteor. Soc.,* **76,** 189–217.

Szeto, K. K., and R. E. Stewart, 1997: Effects of melting on frontogenesis. *J. Atmos. Sci.,* **54,** 689–702.

The NCAR (National Center for Atmospheric Research), 2016: The NCAR Command Language Version 6.3.0. UCAR/NCAR/CISL/TDD.

Thomas, B. C., and J. E. Martin, 2007: A synoptic climatology and composite analysis of the Alberta Clipper. *Wea. Forecasting,* **22,** 315–333.

Uccellini, L. W., and P. J. Kocin, 1987: The interaction of jet streak circulations during heavy snow events along the east coast of the United States. *Wea. Forecasting,* **2,** 289–308.

—–, R. A. Petersen, P. J. Kocin, K. F. Brill, and J. J. Tuccillo, 1987: Synergistic interactions between an upper-level jet streak and diabatic processes that influence the development of a low-level jet and a secondary coastal cyclone. *Mon. Wea. Rev.,* **115,** 2227–2261.

Waldstreicher, J. S., 2001: The importance of snow microphysics for large snowfalls. [Available online at http://www.erh.noaa.gov/er/hq/ssd/snowmicro/].

Ware, E. C., D. M. Schultz, H. E. Brooks, P. J. Roebber, and S. L. Bruening, 2006: Improving snowfall forecasting by accounting for the climatological variability of snow density. *Wea. Forecasting,* **21,** 94–103.

Wick, G. A., 2014: Implementation and initial application of an atmospheric river detection tool based on integrated vapor transport. 2014 Fall Meeting, San Francisco, CA, Amer. Geophys. Union, Abstract A34E-06.

Zhu, Y., and R. E. Newell, 1998: A proposed algorithm for moisture fluxes from atmospheric rivers. *Mon. Wea. Rev.,* **126,** 725–735.